Fall 12-14-2011

Calculated Vibrational Properties of Quinones in Photosynthetic Reaction Centers

Hari Prasad Lamichhane

CALCULATED VIBRATIONAL PROPERTIES OF QUINONES IN PHOTOSYNTHETIC REACTION CENTERS

by

HARI PRASAD LAMICHHANE

Under the Direction of Dr. Gary Hastings

ABSTRACT

This thesis presents a detailed computational investigation into the vibrational properties of quinones involved in solar energy conversion processes in photosynthetic reaction centers. In particular, we focus on the vibrational properties of the ubiquinone molecule that occupies the Q_A binding site in purple bacterial photosynthetic reaction centers.

To provide a foundation upon which to base computational studies of pigments in protein binding sites density functional theory based calculations of the vibrational properties of neutral ubiquinone in the gas phase and in solvent were undertaken. From single point energy calculations it was shown that at least eight ubiquinone conformers, each with slightly different FTIR spectra, could be present in solvent at room temperature.

The calculated and experimental spectra for neutral ubiquinone in solution are very different from the spectra associated with ubiquinone in the Q_A binding in purple bacterial reaction centers. For this reason an ONIOM method was undertaken in which the pigment was treated using density functional theory based methods while the protein was treated using molecular mechanics. The ONIOM calculations not only modeled the experimental Q_A FTIR difference spectra but also resolved the long standing issue of whether a very strong hydrogen bond exists

between the bound ubiquinone and the imidazole nitrogen of a histidine residue (HisM219). To further validate the usefulness of the ONIOM approach experimental isotope edited FTIR spectra obtained using purple bacterial reaction centers with a range of chainless symmetrical quinones incorporated were modeled. Again, the agreement between the calculated and experimental spectra is outstanding.

We also modeled the vibrational properties of the ubisemiquinone anion radical both in solvent and in the Q_A binding site. Vibrational modes of ubisemiquinone display a greater degree of mixing of the various molecular groups of the molecule. Nonetheless the calculated FTIR spectra for ubisemiquinone in solution and in the Q_A site agree very well with that found experimentally. Vibrational frequencies of ubisemiquinone obtained from ONIOM calculated Raman spectra also agree very well with that found in experimental resonance Raman spectra associated with the ubisemiquinone anion radical in the Q_A binding site.

INDEX WORDS: Photosynthesis, Purple bacteria, Purple bacteria reaction centers, Rhodobactor sphaeroides reaction centers, Ubiquinone (UQ), Ubiquinone conformers, Duraquinone (DQ), Dimethyl napthquinone (DMNQ), Vitamin K1, 2-,3-dimethoxy 5-,6- dimethyl 1-,4-benzoquinone (MQ0), Neutral quinines, Semiquinones, Q_A binding site, Fourier transform infrared (FTIR) spectra, Gaussian calculations, Density functional theory (DFT), Gas phase model, Polarizable continuum model (PCM), Our own N-layered quantum mechanics + molecular mechanics (ONIOM), Quantum mechanics/molecular mechanics (QM/MM), Difference spectrum, Double difference spectrum, Potential energy distribution, Gar2ped

CALCULATED VIBRATIONAL PROPERTIES OF QUINONES IN PHOTOSYNTHETIC REACTION CENTERS

by

HARI PRASAD LAMICHHANE

A Dissertation Submitted in Partial Fulfillment of the Requirements for the Degree of

Doctor of Philosophy

in the College of Arts and Sciences

Georgia State University

2011

CALCULATED VIBRATIONAL PROPERTIES OF QUINONES IN PHOTOSYNTHETIC REACTION CENTERS

by

HARI PRASAD LAMICHHANE

Committee Chair: Dr. Gary Hastings

Committee: Dr. Richard H. Miller
Dr. A. G. Unil Perera
Dr. Brian D. Thoms
Dr. Gennady Cymbalyuk

Electronic Version Approved:

Office of Graduate Studies
College of Arts and Sciences
Georgia State University
December 2011

ACKNOWLEDGEMENTS

My time at the Department of Physics and Astronomy at Georgia State University as a graduate student has been a great learning experience both as a researcher and as a person, for which I have many to thank.

First of all, my sincere gratitude goes to Dr. Gary Hastings for his invaluable guidance and support in completing this dissertation, for his patience during times when my progress was slow. Many in Dr. Hastings research group have contributed to this research. Dr. Ruili Wang, Priyangika B. Jayaweera, Dr. Sreeja Parameswaran, Nan Zhao, Dr. Jing Guo and Hiroki Masaki deserve mention for their support. I must also thank my committee members, Dr. Richard H. Miller, Dr. A. G. Unil Perera, Dr. Brian D. Thoms and Dr. Gennady Cymbalyuk for their guidance and support.

This work would not have been possible without the high performance computing facilities at the University Academic Technology Services (UATS) research computing at Georgia State University. I am grateful to Mr. Art Vandenberg, the director of UATS, Mr. Victor Bolet, Mr. Kls Jaroslav and other staff at the UATS for their immense support for the duration of my PhD program. Mostly I must thank Dr. Krzysztof Zborowski (Jagiellonian University, Krakow, Poland) for help in using theGAR2PED program.

I would also like to thank the remarkable teachers at Georgia State University, including, but not limited to, Dr. Nikolaus Dietz, Dr. Gary Hastings, Dr. Steven Manson, Dr. Unil Perera, Dr. Vadym Apalkov, Dr. Mark Stockman, Dr. Stuart A. Allison and Dr. Markus Germann. I would like to thank late Dr. Thomas Netzel for his inspirational teachings in aspects of quantum chemistry.

Also thanks to numerous others in Georgia State University: Charles Hopper and Peter Walker at the Physics Shop, Duke Widsor, Carola Butler, Julie Stoverink, Yvette Hilaire and Felicia Watts and all the staff at the Physics and Astronomy office who have helped with administrative dealings. I would like to thank Dr. Donald Hamelberg, Dr. Don Harden, Dr. Gamini Ariyawansa, Dr. P. V.V. Jayaweera, Mr. Ranga Jayasinghe, and Mr. Abhisek Sen for their help.

I would like to thank Tribhuvan University (T. U.) and Central Department of Physics, T. U., Nepal for providing paid study leave. I would like to thank my teachers, staff, and students at the Central Department of Physics, T. U. for their inspiration and love.

Financial support for this research came through research grants from United State Department of Agriculture (USDA grant number 2004-35318-14889), and National Science Foundation (NSF grant number DBI: 0352324). The support is gratefully acknowledged.

Most importantly, I'd like to thank my daughter, Anuja, my son, Achyut, and my wife, Premkala for their unconditional love and support especially my wife who did her best to help me through the process to finish my Ph. D. I would also like to thank my mother back home who raised me to become the person I am now. Finally, I want to thank all of my family members, friends, and strangers who have knowingly or unknowingly helped me on the way.

TITLE: CALCULATED VIBRATIONAL PROPERTIES OF QUINONES IN PHOTOSYNTHETIC REACTION CENTERS

TABLE OF CONTENTS

LIST OF TABLES

LIST OF FIGURES

9. LIST OFABBREVIATIONS

ALAM260- Alanine M260
ATP- Adenosine triphosphate
B3LYP- Becke, three-parameter, Lee-Yang-Parr exchange-correlation functional
Bchl a- Bacteriochlorophyll a
CD- Circular dichroism
Chl a- Chlorophyll a
D*- Excited bacteriochlorophyll a dimer
DFT- Density functional theory
DMNQ- Dimethyl naphthoquinone
DDS- Double difference spectrum
DQ- Dura quinone
DS- Difference spectrum
ENDOR- Electron nuclear double resonance
ESEEM- ***Electron spin echo envelope modulation***
FTIR- Fourier transform infrared
HisM219- Histidine M219
HYSCORE- Hyperfine sub-level correlation
IEF- Integral equation formalism
IR- Infrared
IUPAC- International union of pure and applied chemistry
MQ_0- 2-,3-dimethoxy 5-,6-dimethyl 1-, 4-benzoquinone
$NADP^+$ - Nicotinamide adenine dinucleotide phosphate
NMR- Nuclear magnetic resonance
OFac- Overlap factor
ONIOM- Our own N-layered Integrated molecular Orbital and molecular Mechanics
PBRC- Purple bacteria reaction center
PCM- Polarizable continuum model
PDB- Protein data bank
PS I Photosystem I
PS II- Photosystem II
Q- Quinone
Q_A- A side quinone
Q_B- B side quinone
QH_2- Hydroquinone
QM:MM-Quamtum mechanics: molecular mechanics
Rb. sphaeroides-Rhodobactor sphaeroides
RC- Reaction center
RMin- Minimum radius

TRP M252- Tryptophane M252
UQ_0- Ubiquinone without isoprene unit
UQ_1- Ubiquinone with single isoprene unit (Ubiquinone one)
$UQ_1^{\cdot}$ -Ubiquinone one radical anion
UQ_3- Ubiquinone with three isoprene units
UQ_6- Ubiquinone with six isoprene units
UQ_8- Ubiquinone with eight isoprene units
UQ_{10}- Ubiquinone with ten isoprene units
UQ_n- Ubiquinone with n isoprene units
VdW- Van der Waal
VK1- Vitamin K1

CHAPTER 1

INTRODUCTION

1.1 Photosynthesis:

The word photosynthesis is made from two words: photon and synthesis. Photon is the smallest unit (quantum) of light energy. Synthesis means production of something by combining separate things. Thus, photosynthesis is a natural process by which green plants, algae and bacteria convert carbon dioxide into organic food using solar energy [1, 2]. Another raw material, water is reduced and oxygen is evolved in oxygenic photosynthesis. However, oxygen is not evolved in bacterial photosynthesis [3]. In either case, photosynthesis is a coordinated process which occurs in four steps: 1) solar energy harvesting, 2) charge separation, 3) electron transport and 4) ATP synthesis [4].

Solar energy trapping takes place in the light-harvesting pigment-protein complexes. Without loss, the trapped energy reaches to the reaction center (RC) which consists of special pair of chlorophylls or bacteriochlorophylls and triggers charge separation reaction [5]. Charge separation initiates a series of electron transfer reactions that are coupled to the translocation of protons across the membrane, generating an electrochemical proton gradient that powers chemical reaction needed for ATP synthesis. Schematic representation of protein complexes involved in oxygenic photosynthesis is shown in Figure 1.1.

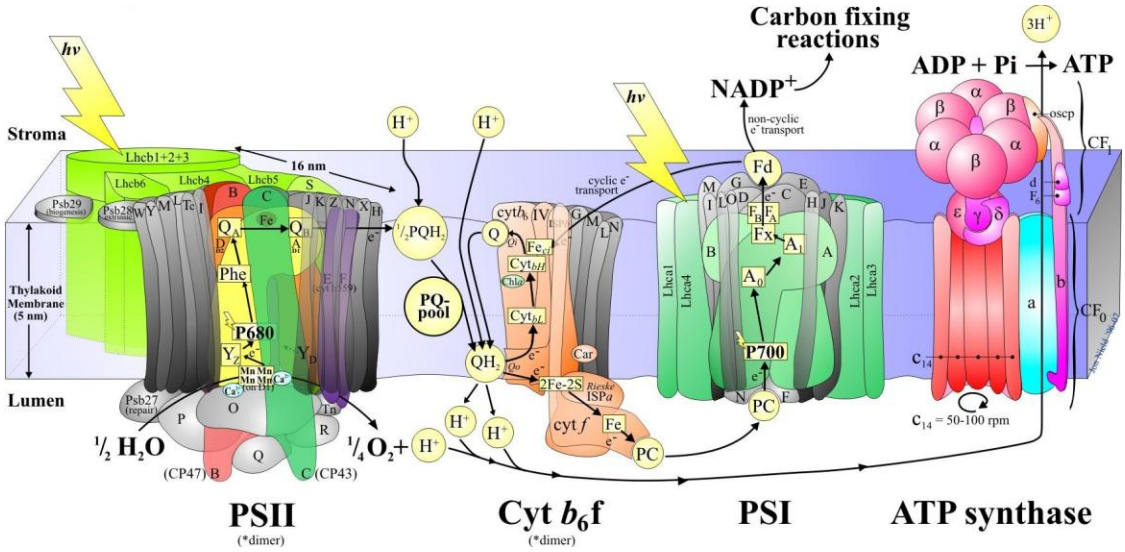

Figure 1.1: Schematic representation of four protein complexes within the thylakoid membrane. (http://queenmaryphotosynthesis.org/nield/psIIimages/oxygenicphotosynthmodel.html)

In oxygenic photosynthesis, solar photons are captured by chlorophyll antenna pigments bound to the periphery of PS II and PS I. The captured energy is rapidly transferred to a special pigment (or group of pigments) in the reaction center (RC) called the primary electron donor. The primary electron donor in PS I/PS II is called P_{700}/P_{680} (Figure 1.1), respectively. Upon excitation of the primary electron donor an electron is transferred via a series of acceptors across the membrane to a terminal acceptor species that is either an iron-sulfur cluster in PS I or a quinone in PS II. The quinone (Q) becomes quinole (QH_2) after receiving two electrons from PS II. Cytochrome b_6f complex coordinates cycle of Q/QH_2 exchange with PS II. Cytochrome b_6f complex gives one of the electrons to Rieske iron-sulfur protein and to plastocyanin. Finally, P_{700}^{+} gets electron from plastocianin. On the other hand the reduced iron-sulfur cluster reduces $NADP^{+}$ to NADPH. The NADPH and potential gradient across the thylakoid membrane convert ADP to ATP. In the dark reaction ATP converts CO_2 into carbohydrate.

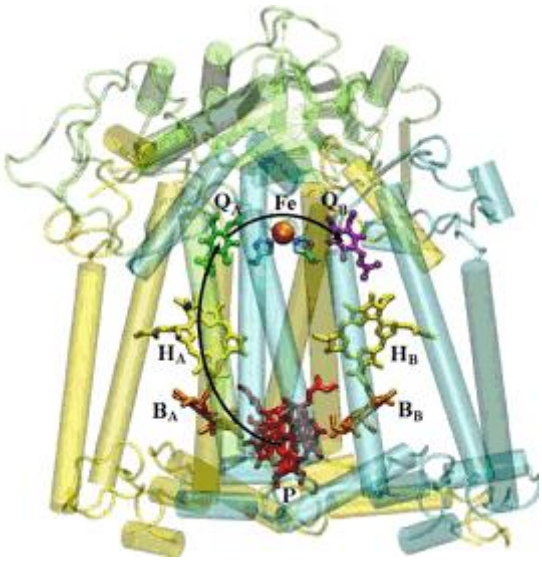

Figure 1.2 Structure of Q_A binding site and arrangement of pigment molecules of Rb. sphaeroides RC: Yellow, blue and green color groups represent L, M and H sub-units of protein. The pigment molecules and electron transport path way are also shown in the figure. The figure was made from crystal structure 1AIJ [3, 6].

1.2 Purple Bacteria

Purple bacteria are prokaryotic anoxygenic photosynthetic organisms. They can grow in the aquatic, harsh habitat where very deem light can reach. They do not reduce H_2O and hence cannot evolve oxygen in the photochemical process. However, they use H_2S or other organic materials in photosynthesis. On the basis of raw material used in the photochemical process, the purple bacteria can be classified into two categories: the non-sulfur purple bacteria (e.g., Rhodobacter sphaeroides and Rhodospeudomonas viridis) and the sulfur purple bacteria (e.g., Chromatium vinosum) [7]. Non-sulfur purple bacteria typically use an organic electron donor, such as succinate or malate. They can also use hydrogen gas. The sulfur bacteria use an inorganic sulfur compound, such as hydrogen sulfide as the electron donor. The only pathway for carbon fixation by purple bacteria is the Calvin cycle. Sulfur purple bacteria must fix CO_2 to live,

whereas non-sulfur purple bacteria can grow aerobically in the dark by respiration on an organic carbon source.

Many bacteria species can only survive in environments that have a low concentration of oxygen. The beauty of purple bacteria is that they can consume a toxic substance H_2S and contribute organic matter to anoxic environment by their autotrophic capacities or they can consume non-fermentable organic compounds in their roles as photoheterotrophs. In either case purple bacteria reduces the pollution in the aquatic medium, where they grow.

1.3 Rb. Sphaeroides Reaction Center

Determination of the three-dimensional structures of the reaction center of the non- sulfur purple bacteria, Rhodobacter sphaeroides, has provided an unprecedented opportunity to understand the structure and function of photosynthetic reaction centers [6, 8]. The positions of the electron transfer components in the reaction center of Rhodobacter sphaeroides are shown in Fig 1.2. Rb. sphaeroides RC consists of three groups of protein sub-units L, M and H. Originally L, M and H named for light, medium and heavy sub-units [4]. Later on H was found the must lightest protein sub-unit among three. The L and M sub-units binds the pigment molecules which involve in the electron transfer process. The pigment molecules present in the reaction center are: four bacteriochlorophyll-A (BChlA) and two bacteriopheophytin (BPh) molecules, two ubiquinones Q_A and Q_B and a non-heme iron. Two of the bacteriochlorophyll-a molecules form the primary donor (D). Function of other two chlorophylls is not clear. After getting solar energy, the primary donor D becomes excited. The excited D* gives electron to the L-side bacteriopheophytin (BPh_L). The reaction takes place in ~ 3 ps. The reduced BPhL then reduces

Q_A in ~ 200 ps [9, 10]. The electron transfer from Q_A^- to Q_B takes place in 3-200 μs [11]. The process involved in the electron transfer from Q_A^- to Q_B takes is the current field of research.

1.4 Q_A Binding Site

10Å sphere of Q_A binding site of Rb. sphaeroides RC (PDB code 1AIJ) contains one ubiquinone molecule, 49 amino acids, seven water molecules and a non-heme iron atom. Q_A and some amino acids surrounding it are shown in Figure 1.3. As shown in Fig. 1.3, Ala M260 and His M219 are supposed to provide hydrogen bonds to two carbonyl groups of Q_A at position C_1 and C_4. Ala M260 it at 2.84 Å away from the C_1=O carbonyl and His M219 is 2.84 Å away from the C_4=O carbonyl. Another possible candidate which can give H-bond to C_4=O carbonyl group is Thr M222. The doubly oxidized iron atom is at 2.19 Å from the N_ϵ of His M219. The Tryptophan Trp M252 is almost parallel to the Q_A head group. Other amino acids which are in vicinity of methoxy groups are Ile M265 and Met M262.

Although, the crystal structure digs up the relative positions of heavy atoms within the experimental resolution, the actual position of hydrogen cannot be seen in the crystal structure. Even if the actual position of atoms is known that is still an interesting field of research, nobody knows the interaction between the quinone and its protein environment. This problem should be solved by other means. Spectroscopic and magnetic tools can help better explore the physical properties of Q_A in the binding site. Some of the spectroscopic measurements are UV-visible absorption, pump-probe method; circular dichroism (CD), Raman spectroscopy, resonance Raman spectroscopy and Fourier transform infrared (FTIR) spectroscopy. On the other hand, electron paramagnetic resonance (EPR), nuclear magnetic resonance (NMR), electron nuclear double resonance (ENDOR), Electron Spin Echo Envelop Modulation (ESEEM) [12], Hyperfine

Sub-level Correlation (HYSCORE), Mossbauer effect, and Zeeman effect measurements deal with interaction between nuclear or electronic spin and the applied magnetic field. Spectroscopic measurement can be applied to neutral as well charged molecules. But, magnetic techniques are used only for charged molecule which has unpaired spin [13]. Most of the experimental and theoretical works were concentrated on exploring possible reasons why two ubiquinones behave differently in purple bacteria and whether two carbonyls of Q_A are asymmetrically bind to the nearest amino acids of the binding site. In this research we use computational method to study vibrational properties of ubiquinone molecule in the gas phase, in CCl_4 and in the Q_A binding site. We observed that Q_A binding site do impact on the ubiquinone molecule both in the neutral and anion phase.

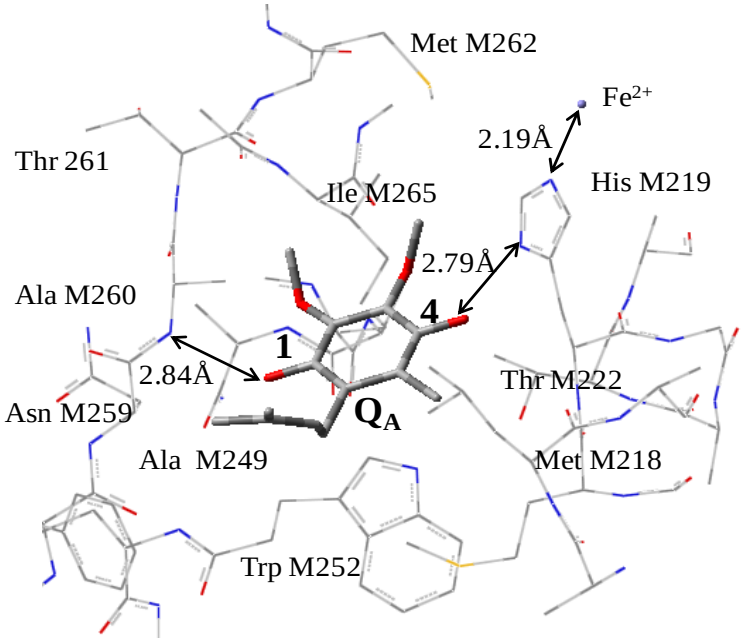

Figure 1.3 Structure of Q_A molecule and surrounding amino acids. This structure is taken from the Rb. sphaeroides RC crystal structure file 1AIJ and prepared using GaussView.

1.5 Fourier Transform Infra-Red (FTIR) Difference Spectroscopy (DS)

1.5.1 Infrared (IR) Absorbance Spectra

Every poly-atomic molecule has various types of energy levels such as electronic, vibrational, rotational and translational energy levels. The molecular vibrational energy difference lies in the infrared region. That is why the infrared (IR) spectroscopy is useful to monitor vibrational energy levels in molecules. Specific group of atoms in the molecule absorbs at different but definite frequency region. An IR absorption spectrum of a sample is a semi-logarithmic plot of the intensity ratio of the emerging IR beam to the incident IR beam versus wavenumber (or wavelength). Thus specific absorption bands in an IR spectrum relate to specific vibrational modes of specific molecular bonds.

An absorption band can be described quantitatively by the Beer-Lambert law:

$$A = \log(\frac{I_0}{I}) = \varepsilon cl \qquad (1.4)$$

Where A is absorbance; I_0 is the intensity of incident radiation; I is the intensity after passing through the sample; ε is the molar extinction coefficient or absorptivity; c is the concentration; and l is the path length.

The molar extinction coefficient ε depends on the square of the change in dipole moment, of the chemical bond and also on the wavelength. For a given concentration and path length, the absolute intensity of the absorption is determined by the change in dipole moment. In other words, vibrations from different chemical functional groups in the molecule give rise to infrared bands of different intensities due to difference in the change in dipole moment upon light excitation or absorptivity ε.

The set of vibrational modes of a molecule completely depends on type of molecule, charge on the molecule and the interaction with surrounding molecules. One molecule can

interact with the other through the hydrogen-bonding effect, electronic and molecular embedding and Van der Waals interaction. Hydrogen bonding effect is the most studied interaction among them. When a carbonyl group of a molecule makes hydrogen bond with the lone pair donating atom, the vibrational frequency of that carbonyl group decreases. Therefore, IR spectroscopy can be a tool that can be used to find the interaction of a molecule with other molecules in the sample. However, IR spectroscopy cannot dig out the information of all vibrational energy levels of molecules. For example, if a vibrational mode does not undergo a change in dipole moment, it cannot be detected through IR spectroscopic measurement. On the contrary, such a mode undergoes a change in polarizibility and hence can be detected at Raman spectra.

1.5.2 Normal Modes

A normal mode of a molecule is defined as a vibration during which all of the atoms in the molecule move with the same frequency and phase. The frequency of this periodic motion is known as vibrational frequency. A molecular vibration is excited when the molecule absorbs a quantum of energy, E, corresponding to the vibration's frequency, ν (in wavenumber), according to the relation

$$E = h\nu \qquad (1.1)$$

Where *h* is Planck's constant. The set of normal modes of a pure chemical compound in a given environment is unique. For this reason the IR spectrum, which is representative of the normal mode structure of a molecule, is a unique identifier of a specific molecule in a specific environment and provides a “fingerprint” of the molecule(s).

To a first approximation, the motion in a normal vibration can be described as a kind of simple harmonic motion and the frequency of the vibration can be calculated using the equation

$$\nu = \frac{1}{2\pi c}\sqrt{\frac{k}{\mu}} \qquad (1.2)$$

Where, k is the force constant (spring constant) and μ is the reduced mass. The reduced mass is given by

$$\mu = \frac{m_1 m_2}{m_1 + m_2} \qquad (1.3)$$

Where m_1 and m_2 are the component masses of the two atoms forming the chemical bond.

Equation 1.2 gives the simple link relating the frequency of light that a molecule will absorb to the reduced mass of the interacting atoms and the strength of the covalent bond between the two atoms.

1.5.3 Mass and Electronic Effects

Equation 1.2 indicates that when the force constant (*k*) increases, vibrational mode frequency increases or up-shift, and vice versa. The force constant is related to the distribution of electron density within the chemical bond between the atoms. Hence the vibrational frequency of a functional group also depends on the electronic structure of a molecule. The decrease or increase in bond strength on change in the electronic charge of the molecule depends on types of bonding. For example, carbonyl stretching vibrational frequency of ubiquinone molecule decreases upon anion formation.

The frequency of the vibrational mode also depends on the reduced mass of the vibrating pair of atoms (equation 1.2). Increasing the reduced mass (using isotope labeled atoms) will cause the vibrational frequency to decrease or down-shift, and vice versa. This type of isotope induced frequency alteration is called a mass effect.

1.5.4 Difference and Double Difference FTIR Spectra

Pigment molecules in a photosynthetic unit bind by groups of protein sub-units. Thus, the FTIR absorption spectrum contains information not only from the pigment molecules but also from the rest of the molecules present in the sample. In general it is almost impossible to observe

absorption bands only due to pigment molecules in the photosynthetic sample. However, only the pigment molecules undergo change in the electronic state during electron transport, so that the IR bands related only to the pigment molecules should change during electron transfer reaction. The change in the spectral band is still very small and hard to observe in the absorption band. However, on subtracting one absorption spectrum from the other, we can separate the bands due to the pigment molecules. The difference spectrum will contain negative bands due to the neutral molecule and positive bands due to the charged molecule.

Spectral band analysis will be difficult if the difference spectrum contain information not only from the pigment molecules but also from other molecules which are interacting with the pigment molecules [14-17]. In such case, isotope labeling on the pigment molecule will help finding bands related only to pigment molecule. Contribution on the difference spectrum from other molecules can be removed by subtracting difference spectrum with unlabeled molecule from the difference spectrum of the isotope labeled molecule. The final FTIR spectrum is called double difference spectrum. Positive bands in the double difference spectrum can be due to neutral unlabeled molecule or isotope labeled charged molecule. With the prior knowledge of bands of molecules in solvents, it is not difficult to identify bands in the double difference spectrum.

1.6 Calculated FTIR Spectra

1.6.1 Level of theory

For vibrational frequency calculation of charged molecule in the Gaussian program, density functional theory (DFT) with B3LYP functional and 6-31+G(d) basis set is useful [18].

1.6.2 Steps of vibration frequency calculation of a molecule

The molecule under study can be constructed using GaussView or can be imported into the GaussView. The molecule should be geometry optimized before settings for frequency calculation using Gaussian key word opt. The level of calculation and memory limits can be set using GaussView. IR frequency and intensity can be calculated using keyword freq. For calculation in solvent, the type of solvent can be selected from the option given in GaussView. After frequency calculation, IR spectra can be constructed from the sick spectra using 4 cm^{-1} spectral width.

1.6.3 ONIOM (Our own N-layered Integrated molecular Orbital + molecular Mechanics) for optimizing pigment molecule in the protein binding site

Quantum level frequency calculation of the pigment molecule and the protein binding site together is not feasible. However, effect of binding site can be incorporated during optimization of pigment molecule in the binding site using ONIOM method [19]. ONIOM method is basically important for treating pigment molecule and the protein at different level by partitioning them in different layers. The pigment molecule can be optimized at quantum level (high level) and the rest of molecules at molecular level (low level). The high level calculation is performed using DFT with B3LYP functional and 6-31+G(d) basis set. Electronic embedding of the protein binding site on the quinone molecule can be obtained using AMBER level of calculation at the low level and Gaussian key word ONIOM = embed. ONIOM layer and Q_A site model prepared for ONIOM calculation is shown in Figure 1.4.

The optimized energy of the pigment molecule in the ONIOM method can be calculated as:

$$E^{ONIOM} = E^{real,MM} + E^{model,QM} - E^{model,MM}. \quad 1.4 \quad [19]$$

Vibrational frequency and IR intensity calculation of the optimized molecule is calculated at the quantum level using DFT with B3LYP functional and 6-31+G(d) basis set.

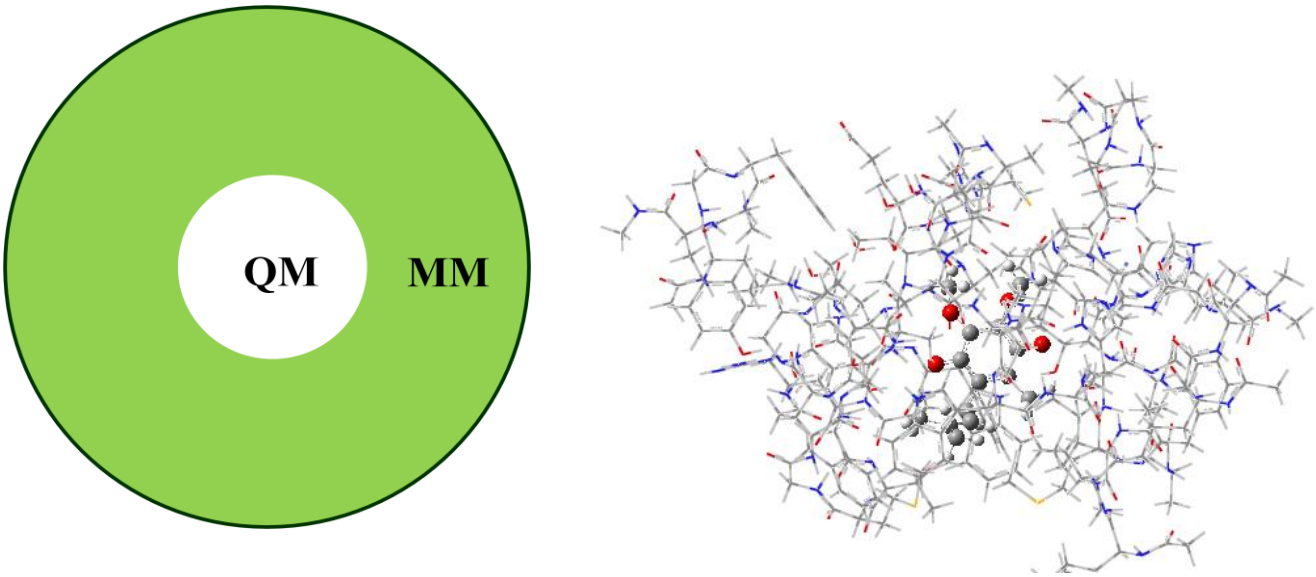

A B

Figure 1.4 A) ONIOM layer, B) 10Å sphere of Q_A binding site prepared for ONIOM calculation. The Q_A molecule is treated at high level and the rest of the molecules are treated at molecular level. This binding site consists of one ubiquinone molecule, 49 amino acids, 7 water molecules and one non-heme iron atom.

1.7 Brief Introduction of Chapters

Chapter 2 contains material already published in the Vibrational Spectroscopy journal. Here we discuss on the calculated neutral ubiquinone structures and FTIR spectra in the gas phase and in CCl_4. We have observed at least eight low energy neutral ubiquinone conformers in the gas phase and in solvent. Not a single conformer can fully explain isotope edited experimental spectra in various solvents. However, Boltzmann averaged spectra of all eight neutral ubiquinone conformers could explain the experimental FTIR spectra. The IR frequency of neutral ubiquinone carbonyl vibration depends on the orientation of methoxy groups. The IR

frequency of the carbonyl group which is proximal to the methoxy group lying nearly parallel to the ubiquinone ring is higher than the IR frequency of distant carbonyl group. This observation clearly objects possibility of symmetrical band shifting in single molecule on specific ^{13}C labeling at C_1 or C_4 position. However, there is equal chance of either methoxy group but not both at a time lying on the ubiquinone plane. Hence on the average both carbonyl groups equally contribute to either carbonyl band.

Chapter 3 discusses on the calculated anion ubiquinone structures and FTIR spectra in the gas phase and in CCl_4. We have observed at least four low energy anion ubiquinone conformers in the gas phase and in solvent. Not a single methoxy group lies on the ubiquinone plane in the anion state. All four anion ubiquinones have similar carbonyl IR frequencies. We also observe an intense FTIR band as found in the experimental FTIR spectra. The C=C stretching frequency lies in the higher frequency than the C=O stretching frequency. Upon ^{13}C isotope labeling C=C out-of-phase mode, C=O mode and methyl bending modes couple and the FTIR spectrum becomes complex. On ^{18}O labeling, only the carbonyl band mixes with methyl bending modes.

Chapter 4 contains materials already published in PNAS journal. To test whether the C_4=O carbonyl of Q_A in Rb. sphaeroides reaction center is unusually strong hydrogen bonded or not, we have optimized the neutral ubiquinone molecule in the 10Å sphere of protein binding site from either carbonyl oxygen of the ubiquinone molecule using ONIOM method. We could simulate experimental double difference spectra. However, we do not observe unusually strong hydrogen bond at C_4=O carbonyl. Instead we observe C=C out-of-phase band up shifting upon $^{13}C_4$ labeling. This effect is not anticipated in the experimental FTIR spectra.

Chapter 5 discusses on the calculated anion ubiquinone structures and FTIR spectra in the Q_A binding site of Rb. sphaeroides RC. Here also we prepared 10Å sphere of protein binding site

from either carbonyl oxygen of the ubiquinone molecule for ONIOM calculation. We observe that with increase in size of ubiquinone head group, H-bonding distance from both carbonyl decreases. We also observe splitting of unique intense FTIR band into three equivalent bands as observe in the experimental FTIR double difference spectra of ubiquinone in the Q_A binding site. However, Calculated FTIR band separations do not match with experimental FTIR band separations as was observed in the neutral molecule FTIR spectra. Because of the interaction with protein binding site, both carbonyl bands downshifted from the solvent phase bands. The mode downshifting is more for C_4=O carbonyl. We observe that the origin of three equivalent bands is not only the asymmetric interaction of protein binding site on the anion ubiquinone molecule but also the coupling of the carbonyl vibration with the methyl bending vibration.

Effect Q_A binding site on various quinines is discussed in chapter 6. We have replaced ubiquinone with Vitamin K1, DMNQ, DQ or MQ_0 molecule. We have successfully simulated experimental isotope edited double difference spectra for all molecules except MQ_0. MQ_0 can have various conformations in the Q_A binding site. Study of various conformations MQ_0 in Q_A binding site will be another research work so that it is not discussed in this dissertation. Here also concept of strong hydrogen bonding to C_4=O is not required to explain experimental isotope edited double difference spectra.

Finally, method of resp charge and amber parameter calculation using antechamber program, systematic way of exploring ubiquinone conformers and definitions of internal coordinates as well as potential energy calculation using gar2ped program are discussed in the appendix.

CHAPTER 2
COMPARISON OF CALCULATED AND EXPERIMENTAL FTIR SPECTRA OF SPECIFICALLY LABELED UBIQUINONES

2.1 Abstract

Density functional theory has been used to calculate harmonic vibrational frequencies and intensities of unlabeled and labeled ubiquinone-1 in both the gas phase and in solution (CCl_4). Calculations were undertaken using the B3LYP functional and the 6-31G+(d) basis set. Calculations using larger basis sets did not significantly alter the calculated spectra. Calculations for ubiquinone-2, 3, 6 or 8 gave very similar results. Ubiquinone-1 is therefore an appropriate model for the calculation of the properties of ubiquinones with longer isoprene side chains.

From single point energy calculations of ubiquinone-1 with all possible methoxy group orientations it is found that eight ubiquinone-1 structures/conformations, which differ only in the orientation of their methoxy groups, will exist in solution at room temperature. The calculated infrared spectra for these eight conformations vary considerably. However, by averaging the Boltzmann weighted spectra for the eight conformers, composite spectra are calculated that accurately model both the frequency and intensity information inherent in the experimental FTIR spectra obtained for both unlabeled and labeled ubiquinones in solution.

The calculated spectra presented here provide a robust foundation from which to consider and assess future modeling of the vibrational properties of ubiquinones embedded in protein complexes.

Keywords: Ubiquinone; FTIR; Density functional theory; Vibration; Group frequency; Normal mode.

2.2. Introduction

Ubiquinones (UQ_n: 2,3-dimethoxy-5-methyl-6-polyprenyl-1,4-benzoquinone, see Fig. 2.1 for structure and numbering) play an important role in biological electron and proton transfer processes that occur in both respiration and photosynthesis[20]. In photosynthetic reaction centers from purple bacteria, two UQ molecules, called Q_A and Q_B, act as terminal electron acceptors [21]. In purple bacterial reaction centers (PBRCs)[1] from *Rhodobacter sphaeroides*, Q_A and Q_B are both ubiquinone-10 (UQ_{10}) molecules. Q_A and Q_B have very different functions, however. Q_A is an intermediary cofactor involved in transferring electrons from bacteriopheophytin to Q_B, while Q_B couples electron and proton transfer processes [22, 23]. The very different redox functions of Q_A and Q_B is testimony to the flexibility of UQs in biological processes. Since Q_A and Q_B are both UQ_{10} molecules, it is clearly the nature of pigment-protein interactions that modulate UQ_{10} functional properties in PBRCs. It is elucidation of these structure function properties of UQs that is at the heart of much current research in photosynthesis.

Fourier transform infrared (FTIR) difference spectroscopy (DS) is a sensitive molecular-level probe of pigment-protein interactions, and it is widely used to study both the neutral and reduced quinone states in PBRCs[24]. Q_A^-/Q_A and Q_B^-/Q_B FTIR DS are difficult to interpret because many bands not associated with the quinone also contribute to the spectra. Reconstitution of PBRCs with isotopically labeled quinones, however, has allowed some separation of the contributions of the quinones from those of the protein to the spectra[24]. Nonetheless the

[1]Abbreviations: Density functional theory, DFT; difference spectra/spectrum/spectroscopy, DS; Fourier transform infrared, FTIR; infrared, IR; integral equation formalism; IEF; purple bacterial reaction centers, PBRCs; polarizable continuum model, PCM; ubiquinone, UQ;

hypothesized experimental FTIR DS band assignments have not been accurately modeled computationally.

Infrared (IR) absorption spectra for unlabeled and specifically isotope labeled UQs in solution have also been obtained. However, from a computational standpoint, even these simpler solution IR spectra are poorly understood. No work has been undertaken that can fully explain all the isotope-induced changes in band frequencies and intensities that are observed in experimental spectra. The work outlined in this manuscript is aimed at addressing this problem.

Fig. 1 shows the structure and numbering scheme for UQ_n. The subscript, *n*, refers to the number of isoprene units in the chain at position 6. Virtually all protein bound UQs contain a poly-isoprene chain. Importantly, experimental FTIR spectra of UQs have been shown to be independent of the number of isoprene units in the chain at position 6, *so long as there is at least one isoprene unit* [25].

Prior to ~2000, several groups had undertaken computational work aimed at modeling the physical and chemical properties of UQs [26-31]. Here we extend upon these works by including several points of detail necessary for accurate modeling of the vibrational spectra of UQs.

Firstly, in many of the previous studies, tail-less UQ models were considered in order to decrease computational expense. Since experimental FTIR spectra for tail-less UQs differ from tail-containing UQs, the tail-less models will inaccurately simulate the vibrational properties of tail-containing UQs.

Secondly, most previous computational studies of UQs were undertaken in the gas phase. In fact, Nonella and Brandli [26] suggested that their calculations poorly modeled aspects of

experimental spectra probably because solvent effects were not considered. Below we will describe tail-containing UQ models in both the gas phase and in CCl_4.

Thirdly, in some previous computational studies of UQs, only the vibrational properties of a UQ with a specific methoxy group conformation were considered [30, 31]. Below we will show that there are four approximately-isoenergetic UQ models that differ only in the conformation of the methoxy groups. We will also show that it is necessary to consider the spectra of all of these conformers in order to accurately describe experimental FTIR spectra.

Fourth, many previous calculations of UQ were undertaken using semi-empirical methods (PM3), or density functional based methods using relatively low-level functional and/or basis sets. We have found that the calculation of the vibrational properties of UQ models is most efficiently undertaken using the B3LYP functional and the 6-31+G(d) basis set. Calculation using a larger basis does not alter the calculated vibrational properties but calculation using a smaller basis set does.

As mentioned above, experimental FTIR difference spectra are available for various types of quinones (both labeled and unlabeled) occupying the Q_A and/or Q_B binding site in PBRCs [32]. On a quantitative level these spectra are poorly understood. One of the goals of modern molecular biophysics is to be able to understand the vibrational properties of quinones in large protein complexes. Such calculations are becoming feasible. However, a rational foundation on which to base such calculations has first to be constructed. It is to this problem that the calculations reported here are addressed, and in this manuscript we describe the simulation of vibrational spectra associated with labeled and unlabeled tail-containing UQ models in both the gas phase and in solvent.

2.3 Materials and methods

2.3.1. Calculations

Molecular geometry optimizations and harmonic vibrational frequency calculations were performed using hybrid DFT methods, employing the B3LYP functional and the 6-31+G(d) method within Gaussian 03 [33]. For calculations including solvent, the integral equation formalism (IEF)[34-36] of the polarizable continuum model (PCM) [37, 38]was used. The PCM uses the united atom cavity approach. Cavity parameters used in all calculations were OFac=0.89 (overlap index between two interlocking spheres) and RMin=0.2 (minimum radius in Angstroms for overlapping spheres). Very similar spectra were calculated when a smaller number of added spheres were considered (OFac=0.8 and RMin=0.5).

Quantitative assignment of calculated vibrational frequencies to molecular groups is based on a consideration of the calculated atomic displacements (in Cartesian coordinates) associated with the normal modes. The extent that a molecular group contributes to a normal mode is also quantified by considering the calculated projection of the normal mode onto the appropriate internal coordinate (see supplementary information section). In addition, the molecular groups that most prominently contribute to the normal modes are assessed visually using software (GaussView03) in which the atomic displacements during the vibration are animated.

Calculated normal mode vibrational frequencies presented here are unscaled. We choose to do this because we are primarily interested in vibrational frequency changes that occur upon isotope labeling. We have shown in the past [39], and we show here that such frequency differences are accurately calculated without scaling, presumably because the same errors are inherent in calculation for both the labeled and unlabeled species. Another reason why we

unscaled the frequency is the difference between scaled and unscaled isotopic frequency shifts would be much smaller than the spectral resolution 4 cm^{-1}. Normal mode intensities are also presented here. With both the frequency and intensity information IR absorption spectra (stick spectra) can be constructed. In previous vibrational frequency calculations of UQs, the relative intensity information was not considered in detail [26]. This is unfortunate since relative intensity information is the key to assessing the validity and accuracy of the computational approach. We note that if intensity information were fully considered in previous UQ vibrational frequency calculations it would have been apparent that the calculated spectra were not in line with experiment.

2.4 Results

2.4.1 UQ structure and numbering

Fig. 2.1 shows the structure and IUPAC numbering scheme for UQ_n. The subscript, *n*, refers to the number of isoprene units in the chain at position 6.

2.4.2 Experimental FTIR absorption spectra of UQ

Experimental FTIR absorption spectra for neutral UQ_{10}, UQ_3 and UQ_6, in the 1590-1690 cm^{-1} region, are shown in Fig. 2A, B and C, respectively. The FTIR spectra for the UQ_3, UQ_6 and UQ_{10} are very similar, demonstrating that the number of isoprene units in the chain at position 6 has no effect on the spectra in the 1590-1690 cm^{-1} region. FTIR spectra for all UQs containing one or more isoprene units are known to be very similar [25].

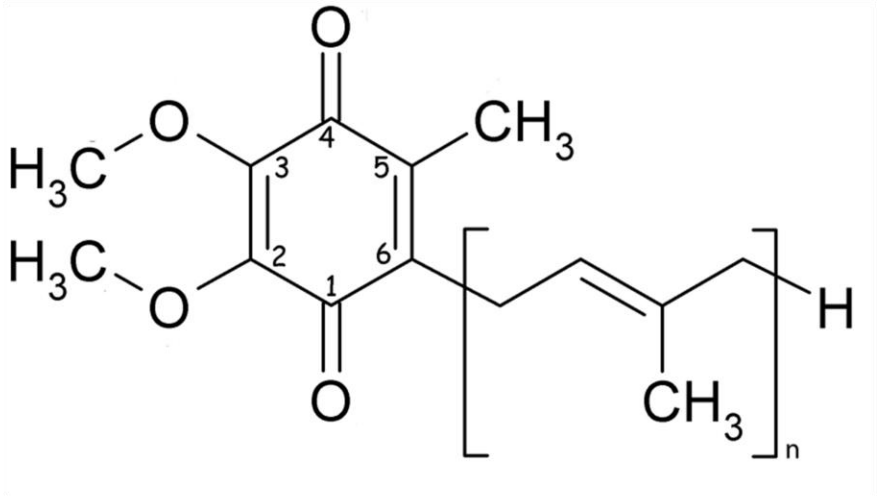

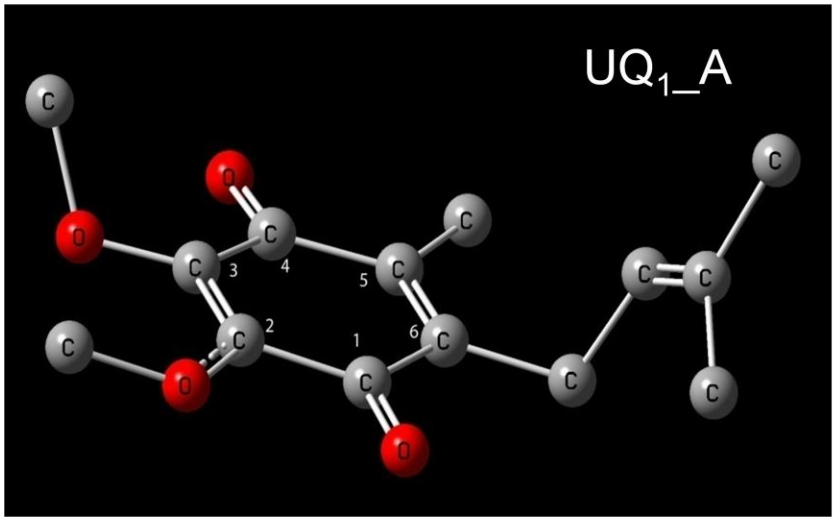

Fig. 2.1. (A) Structure and IUPAC numbering scheme for UQ_n. The subscript *n* refers to the number of isoprene units associated with the chain attached at position 6. (B) Energy minimized UQ_1 model used in calculations. The atom numbering scheme is also shown. The hydrogen atoms have been removed for clarity.

In the FTIR spectra of unlabeled UQ shown in Fig. 2.2, three bands are found at ~1664, 1650 and 1611 cm^{-1}. The 1650/1664 cm^{-1} band is the most/least intense, respectively, with the intensity of the 1611 cm^{-1} band being in between. No computational studies undertaken so far have been able to accurately model these observed relative intensities.

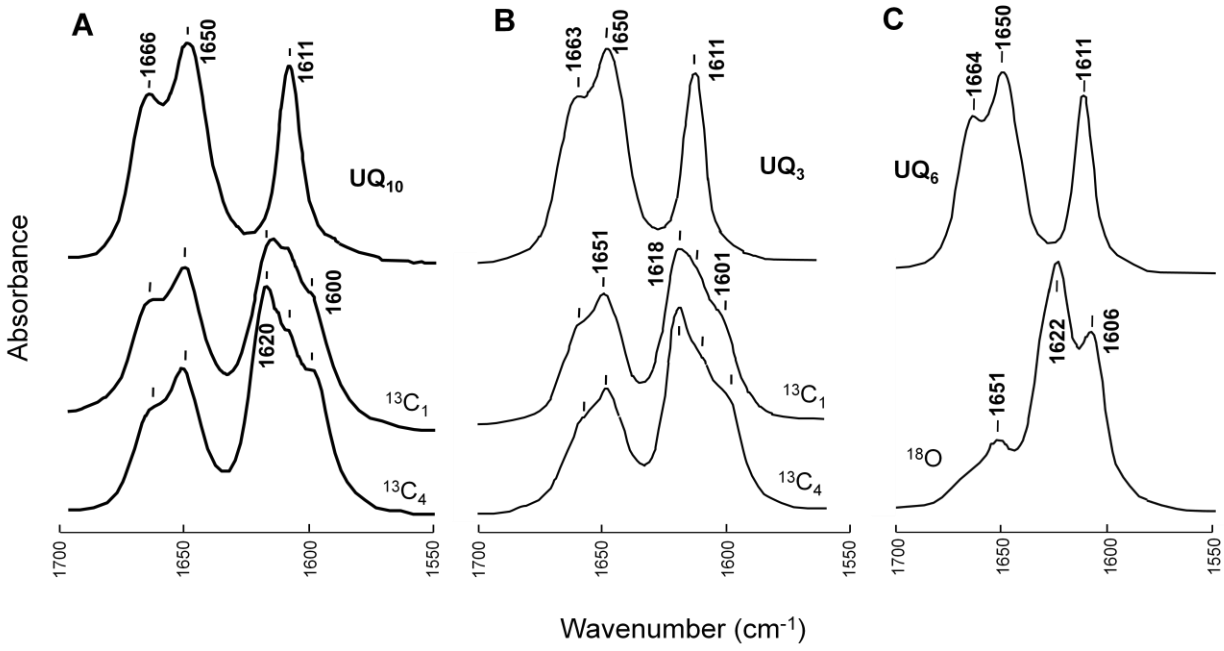

Fig. 2.2. Experimental IR absorption spectra for (A) UQ_{10}, (B) UQ_3 and (C) UQ_6. The spectra for specifically $^{13}C_1$, and $^{13}C_4$ labeled UQ_{10}/UQ_3 are shown in (A)/(B), respectively. The spectra for ^{18}O labeled UQ_6 is also shown in (C). In ^{18}O labeling experiments of UQ_8 (C) only ~75% of the carbonyl oxygen atoms are ^{18}O labeled. The spectra in (A) were obtained from UQ_{10} samples dissolved in n-pentane. The samples were placed on IR transparent windows and the solvent was allowed to evaporate prior to measurement. Spectra in (B) and (C) were for UQs in CCl_4. The spectra in (A) and (B) are similar, i.e, the different solvents do not lead to the changes in the spectra. The UQ_{10}, UQ_3 and UQ_6 spectra were taken from references 16, 17 and 18 (with permission).

Upon $^{13}C_1$ or $^{13}C_4$ labeling the bands at ~1664 and 1650 cm^{-1} decrease in intensity by about 50%, and a new band appears at ~1619 cm^{-1} (Fig. 2.2A, B) The band at 1611 cm^{-1} also decreases in intensity and shifts to 1601 cm^{-1}.

The spectra for $^{13}C_1$ and $^{13}C_4$ specifically labeled UQ indicate that both the 1664 and 1650 cm^{-1} bands are changed when a modification is made at either the 1 or 4 position. So both the C_1=O and C_4=O groups of UQ contribute to both the 1664 and 1650 cm^{-1} bands. In addition, C=C modes must also couple to both the C_1=O and C_4=O groups, as the 1611 cm^{-1} band down-shifts upon both $^{13}C_1$ and $^{13}C_4$ labeling.

Upon ^{18}O labeling of Q_6 (Fig. 2.2C) the 1664 and 1650 cm^{-l} bands down-shift, with a new band appearing at 1622 cm^{-l}, and a weak shoulder around 1630 cm^{-l}. The band at 1651 cm^{-1} in the ^{18}O labeled UQ_6 spectrum is due to the residual (~25%) unlabeled UQ_6. The band at 1611 cm^{-1} in the unlabeled UQ_6 spectrum down-shifts to 1606 cm^{-l} upon ^{l8}O labeling.

No vibrational frequency calculations undertaken so far have been able to simultaneously predict the isotope induced shifting behavior, and the isotope induced band intensity changes, for the above three spectral bands. These unlabeled and labeled experimental spectra then allow for stringent testing of our computational modeling.

2.4.3. Calculated structure of UQ_1

Since FTIR spectra of UQ's do not depend on the number of isoprene units in the chain at position 6, so long as there is at least one unit [25], we will consider only UQ_1 models.[2] The energy minimized structures of a UQ_1 model in the gas phase is shown in Fig. 2.1B, along with

[2] We have undertaken gas phase calculations for a UQ model containing 2, 3, 6 and 8 isoprene units, and have found that the calculated IR spectra are very similar to that calculated for a model containing 1 isoprene unit (not shown). For $UQ_{2,3,6,8}$ models the C=C_t mode is uncoupled from the C=O modes. The C=C_t mode contains negligible intensity, however.

the atom numbering scheme we will use throughout this manuscript. To establish the range of methoxy group dihedral angles of UQ_1 that are likely to be found in solution at room temperature, we have calculated the energy of UQ_1 models in which the methoxy group dihedral angles are systematically varied in 10^o increments. For calculations the methoxy group dihedral angles are constrained but the rest of the UQ_1 molecule is optimized (energy minimized). The energies of optimized UQ_1 structures in the gas phase, with constrained methoxy group dihedral angles, are plotted in Fig. 2.3A. The C_3/C_2 methoxy dihedral angle is defined as the C_2-C_3-O_{16}-C_8 / C_3-C_2-O_{17}-C_9 dihedral angle, respectively. Calculations using C_4-C_3-O_{16}-C_8 / C_1-C_2-O_{17}-C_9 dihedral angles give similar results.

The lowest energy UQ_1 conformations have a C_3 methoxy dihedral angle near $\pm120^o$ or $\pm10^o$ (Fig. 2.3B). For the C_3 methoxy dihedral angle near $\pm120^o$, the lowest energies occur for a C_2 methoxy dihedral angle near $\pm10^o$ (Fig. 2.2B). For the C_3 methoxy dihedral angle near +/- 10^o, the lowest energies occur for a C_2 methoxy dihedral angle near $\pm120^o$ (Fig. 2.3B). The high energy conformations in Fig. 2.3B corresponds to UQ_1 structures where methoxy methyl groups face each other, with both the C_2 and C_3 methoxy dihedral angles being near zero degrees ($\pm10^o$). Given the very high energy of these conformations, they will contribute negligibly to solution spectra at room temperature.

From the data in Fig. 2.3 the lowest energy UQ_1 conformations are likely to have C_2 and/or C_3 methoxy dihedral angles close to ±120 or ±10 degrees. Given this we have fully geometry optimized UQ_1 structures with starting geometries having the above C_2 or C_3 methoxy group dihedral angles. We have considered 12 different conformer starting geometries. The C_2 and C_3 methoxy dihedral angles of the starting geometries, the energies of the optimized structures (relative to the lowest energy structure), and the final calculated C_2/C_3 methoxy

dihedral angles are listed in tables 2.1 and 2.2 for calculations in the gas phase and CCl_4, respectively.

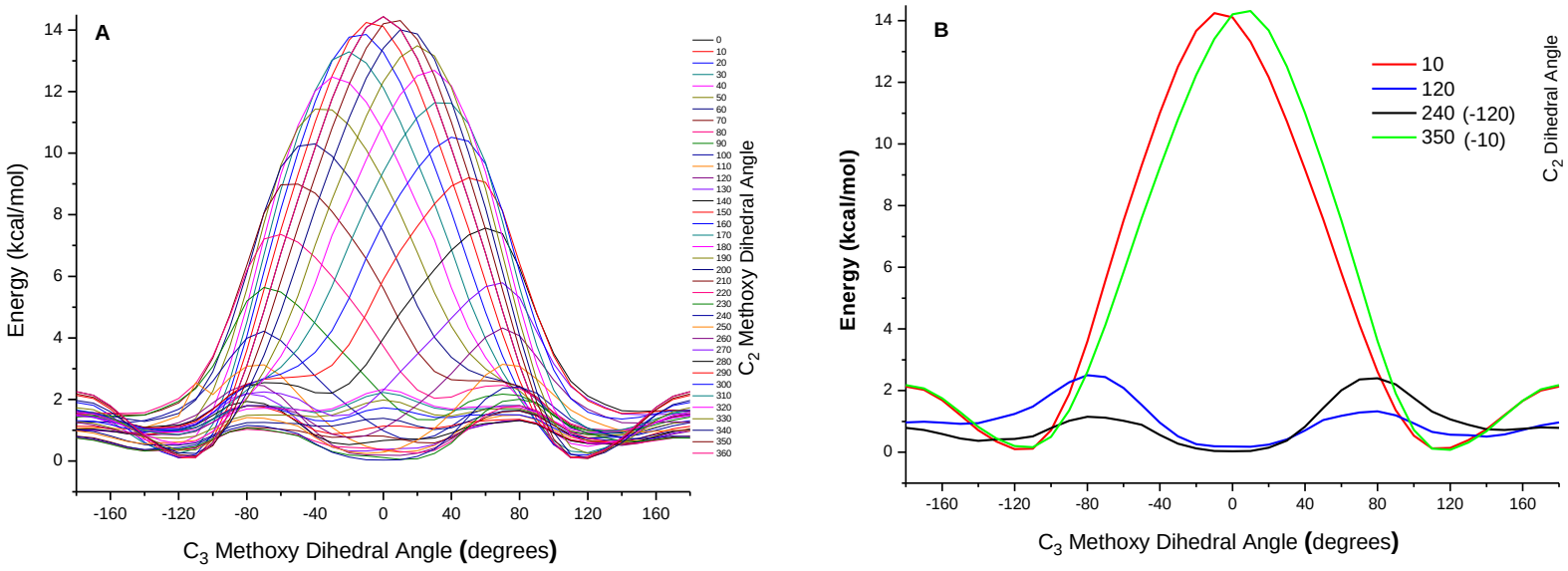

Fig. 2.3. (A) Calculated energies (in kcal/mol) of neutral UQ_1 conformers with constrained dihedral angles. The dihedral angles were systematically varied in 10° increments. The energy axis was shifted by 530361.942 kcal/mol so that the lowest energy conformation has zero energy. (B) Calculated energies (in kcal/mol) of neutral UQ_1 conformers for all C_3 methoxy group dihedral angles, with C_2 methoxy group dihedral angles constrained to ±10 (red and green curves) and ±120 (blue and black curves) degrees.

In the gas phase and CCl_4, the calculated spectra for conformers E and F are virtually identical to that for A and B (see below). This is not surprising since the C_2 and C_3 dihedral angles are similar. Similarly, the spectra for conformers G and H are also very similar to that of conformers D and C, respectively. Below we will consider conformers E, F, G and H to be the same as conformers A, B, D and C respectively. Given the above results we will consider only the eight different conformers (A,B,C,D,I,J,K,L).

Table 2.1: Calculated optimized energies for 12 different UQ_1 starting conformations in the gas phase. The starting and final calculated C_2 and C_3 methoxy dihedral angles are listed. The relative energies of the conformations above the lowest energy conformation are also listed. At 298 K, k_BT ~ 0.592 kcal/mol. Zero point energies are included. Conformer E and F are virtually the same as conformer A and B, respectively. Conformer G and H are also similar to conformer D and C, respectively, with the C_3 methoxy dihedral angle differing by less than 20^o.

Input Conformation	C_2-methoxy dihedral angle		C_3-methoxy dihedral angle		Energy (kcal/mol)	ΔE (kcal/mol)	Output Conformation
	Input	Output	Input	Output			
A	-10	-8.9	120	123.6	530361.90064	0.0414	A
B	10	10.8	-120	-123.0	530361.88885	0.0532	B
C	-120	-124.3	10	10.1	530361.94195	0	C
D	120	120.3	-10	-5.3	530361.75852	0.1835	D
E	10	-9.1	120	123.7	-530361.9006	0.0414	A
F	-10	10.6	-120	-122.9	530361.88885	0.0532	B
G	120	118.3	10	8.0	530361.74247	0.1995	D
H	-120	-122.4	-10	-10.2	530361.86217	0.0798	C
I	120	122.0	120	146.8	530361.43805	0.5040	I
J	-120	-146.5	120	147.3	530361.41343	0.5286	J
K	-120	-129.9	-120	-129.8	530361.55695	0.3851	K
L	120	144.2	-120	-147.0	530361.10274	0.8393	L

Table 2.2 : Calculated optimized energies for 12 different UQ_1 starting conformations in CCl_4. The starting and final methoxy dihedral angles are listed. The relative energies of the conformations above the lowest energy conformation are also listed. Zero point energies are included. For calculations in CCl_4, the energy quoted is the total free energy without inclusion of non-electrostatic terms. Differences in the non-electrostatic terms between conformers are calculated to be negligible. At 298 K, $k_BT \sim 0.592$ kcal/mol.

Input Conformation	2-methoxy dihedral angle		3-methoxy dihedral angle		Energy (kCal/Mole)	ΔE (kcal/mole)	Output Conform
	Input	Output	Input	Output			
A	-10	-9.3	120	120.9	-530364.8585	0.0788	A
B	10	10.7	-120	-121.7	-530364.8912	0.0461	B
C	-120	-122.5	10	10.4	-530364.9373	0	C
D	120	117.2	-10	-5.2	-530364.8081	0.1292	D
E	10	1.8	120	118.4	-530364.8627	0.0746	A
F	-10	-0.5	-120	-117.3	-530364.878	0.0592	B
G	120	115.5	10	5.7	-530364.8015	0.1358	D
H	-120	-119.6	-10	-5.8	-530364.9189	0.0184	C
I	120	118.4	120	123.3	-530363.887	1.0502	I
J	-120	-144.5	120	141.9	-530363.7736	1.1637	J
K	-120	-123.8	-120	-122.7	-530364.0127	0.9245	K
L	120	139.4	-120	-142.3	-530363.4424	1.4949	L

2.4.4 Calculated IR spectra of UQ_1.

The calculated IR spectra in the 1775-1600 cm^{-1} region, for the 8 UQ_1 conformers in the gas phase and CCl_4 are shown in Fig. 4a and c, respectively. The Boltzmann weighted sum of the spectra for these eight conformers in the gas phase and in CCl_4 are shown in Fig. 4b and d, respectively. For the Boltzmann weighted sum of the spectra there are three prominent bands at ~1732/1723, ~1703/1695 and 1652/1650 cm^{-1}, for UQ_1 in the gas phase/CCl_4, respectively. These calculated bands correspond to the bands at ~1663, 1650 and 1611 cm^{-1} in the experimental spectra of unlabeled UQ (Fig. 2.2).

The spectra for conformers A-D are very different to that of conformers I-L. Spectra for conformers I-L show no band near 1732-1722 cm^{-1} (Fig. 4a, c). The band near 1695-1703 cm^{-1} is considerably more intense for conformers I-L, however, and conformers I-L therefore make a large contribution to the band at 1703/1695 cm^{-1} in the Boltzmann weighted sum of the spectra (Fig. 2.4c, d). The band at 1652/1650 cm^{-1} in the Boltzmann weighted sum of the spectra (Fig. 2.4c, d) is due predominantly to contributions from conformers A-D.

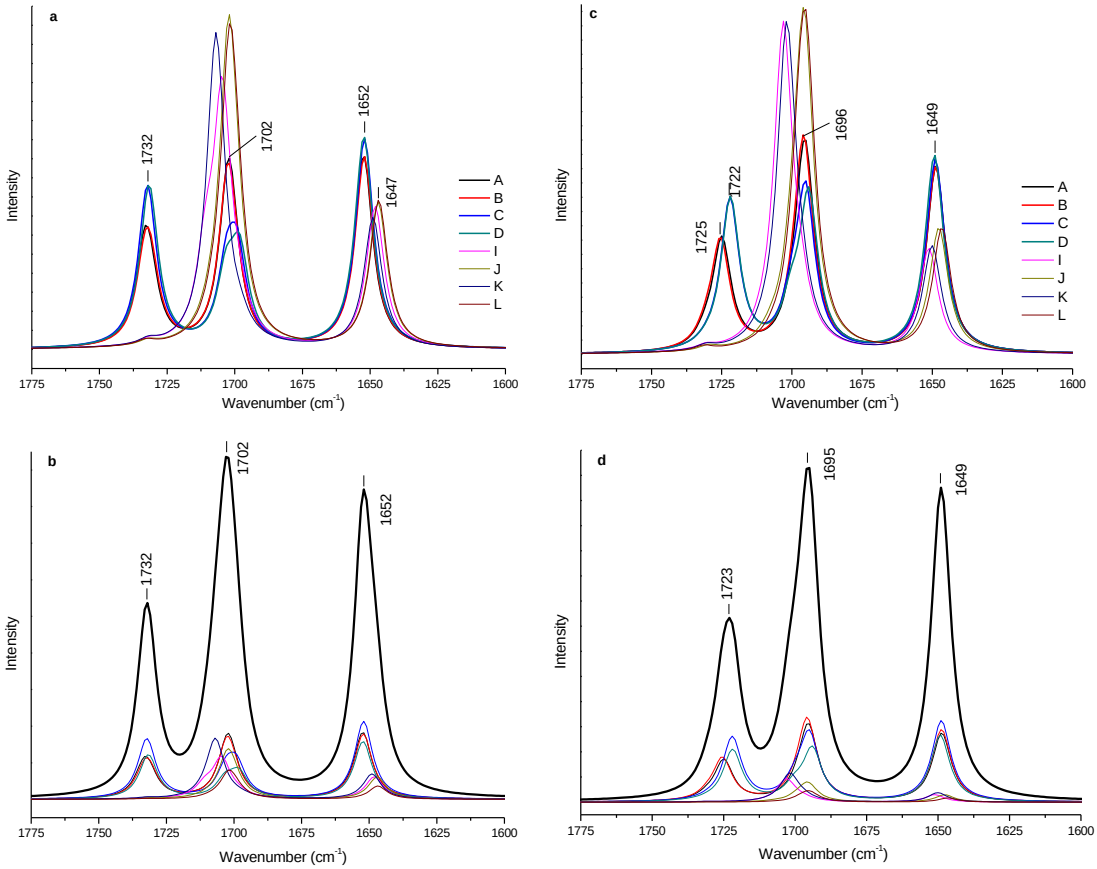

Fig. 2.4. Calculated IR spectra for UQ_1_A-L in (a) the gas phase and (c) CCl_4. The spectra for conformers A-D are shown with a bolder line style to emphasize that the spectra of conformers A-D are distinctly different from the spectra of conformers I-L. (b)/(d) Boltzmann weighted sum of the spectra from all of the conformers in the gas phase/CCl_4, respectively. The appropriately weighted spectra taken from (a)/(c) are also shown. For calculations at room temperature (298

K), the Boltzmann weighting factors for conformer A, B, C, D, I, J, K, L in the gas phase are 0.1800, 0.1765, 0.1930, 0.1416, 0.0824, 0.0790, 0.1007, 0.0468 and 0.2082, 0.2201, 0.2379, 0.1912, 0.0404, 0.0333, 0.0499, 0.0190 in CCl_4.

For gas phase calculations using the larger 6-311++G(d) basis set, the spectra are virtually the same as that shown in Fig. 2.4A, except for a 7-8 cm^{-1} downshift in frequency of all three bands (not shown). For spectra calculated using the smaller 6-31G(d) basis set, there are some significant differences in the spectra, however (not shown). Calculations at the 6-31+G(d) level therefore represent a good compromise for accurate spectral simulation with low computational cost.

Table 2.3 lists the frequencies and intensities of the normal modes that contribute to the bands in the spectra in Fig. 2.3, for each of the eight UQ_1 conformers in the gas phase (A) and CCl_4 (B). For conformers A-D the bands at ~1732/1723 and ~1703/1695 cm^{-1} in the spectra in Fig. 2.4a, c each contain contributions from two modes, while the 1652 cm^{-1} band is due to a single mode.

For conformers I-L the band at ~1703/1695 cm^{-1} in the spectra in Fig. 2.4a, c contains contributions from two modes, while the ~1647 cm^{-1} band is due to a single mode.
To aid in visualization of the mode assignments listed in table 2.3, Fig. 2.5 shows images of the atomic displacements for conformer A in the gas phase (*left*) and in CCl_4 (*right*) that occur for the five modes associated with the three bands. For convenience, $C{=}C_t$ refers to the C=C group of the tail and $C{=}C_r$ refers to a combined vibration of the $C_2{=}C_3$ and $C_5{=}C_6$ groups of the quinone ring. A quantitative description of three of the listed normal modes of UQ_1_B in CCl_4 is given in supplementary information section 1.

Table 2.3. Calculated harmonic normal mode vibrational frequencies (in cm^{-1}), intensities (given in the parenthesis in km/mol) and assignments for the eight unlabeled UQ_1 conformers

A) UQ_1 in the gas phase			
UQ_1_A	UQ_1_B	UQ_1_C	UQ_1_D
1733 (127) C_1=O, C=C_t (*as*)	1733 (111) C_1=O, C=C_t (*as*)	1732 (155) C_4=O, C=C_t (*as*)	1733 (15) C_4=O, C=C_t (*as*)
1731 (67) C_1=O, C=C_t (*s*)	1731 (81) C_1=O, C=C_t (*s*)	1732 (91) C_4=O, C=C_t (*s*)	1732 (232) C_4=O, C=C_t (*as*)
1703 (256) C_4=O, C_2=C_3 (*as*)	1703 (249) C_4=O, C=C_r (*as*)	1703 (110) C_1=O, C=C_r (*as*)	1703 (96) C_1=O, C=C_r (*as*)
1701 (36) C=C_r (*s*)	1700 (40) C=C_r (*s*)	1699 (122) C_1=O, C=C_r (*s*)	1698 (133) C_1=O, C=C_r (*as*)
1652 (292) C_4=O, C=C_r (*as*)	1652 (291) C_4=O, C=C_r (*as*)	1652 (317) C_1=O, C=C_r (*as*)	1652 (321) C_1=O, C=C_r (*as*)
UQ_1_I	UQ_1_J	UQ_1_K	UQ_1_L
1732 (7) C=C_t	1732 (7) C=C_t	1732 (8) C=C_t	1733 (8) C=C_t
1711 (112) C_4=O, C=C_r (*s*)	1709 (16) C=O (s), C=C_r (*s*)	1711 (11) C=O (*s*), C=C_r (*s*)	1708 (19) C=O (*s*), C=C_r (*s*)
1705 (373) C_1=O, C=O (as)	1702 (446) C=O (as)	1707 (472) C=O (as)	1702 (441) C=O (as)
1698 (33) C_4=O, C=C_r (*s*)	1700 (78) C_4=O, C=C_r (*s*)	1698 (17) C=C_r (*s*)	1699 (73) C_4=O, C=C_r (*s*)
1648 (215) C=C_r (*as*)	1647 (221) C=C_r (*as*)	1649 (198) C=C_r (*as*)	1647 (224) C=C_r (*as*)
B) UQ_1 in CCl_4			
UQ_1_A	UQ_1_B	UQ_1_C	UQ_1_D
1731 (20) C=C_t	1731 (24) C=C_t	1730 (6) C=C_t	1731 (6) C=C_t
1724 (224) C_1=O	1725 (220) C_1=O	1722 (308) C_4=O	1722 (309) C_4=O
1699 (31) C_4=O, C=C_r (*s*)	1699 (34) C_4=O, C=C_r (*s*)	1700 (68) C_1=O, C=C_r (*s*)	1700 (74) C_1=O, C=C_r (*s*)
1695 (415) C_4=O	1696 (417) C_4=O	1695 (316) C_1=O, C=C_r (*s*)	1694 (309) C_1=O, C=C_r (*s*)
1649 (379) C_4=O, C=C_r (*as*)	1649 (377) C_4=O, C=C_r (*as*)	1649 (392) C=C_r (*as*)	1649 (400) C=C_r (*as*)
UQ_1_I	UQ_1_J	UQ_1_K	UQ_1_L
1731 (9) C=C_t	1730 (9) C=C_t	1730 (10) C=C_t	1731 (9) C=C_t
1710 (7) C=O (s)	1708 (14) C=O (s), C=C_r(*s*)	1710 (7) C=O (s)	1706 (7) C=O (s), C=C_r(*s*)
1703 (653) C=O (as)	1699 (111) C_1=O, C=C_r (*s*)	1702 (654) C=O (as)	1698 (178) C_1=O, C=C_r (*s*)
1697 (65) C_4=O, C=C_r (*s*)	1696 (639) C=O (as), C=C_r (*s*)	1696 (51) C_4=O, C=C_r (*s*)	1695 (573) C=O (*as*), C=C_r (*s*)
1651 (211) C=C_r (*as*)	1648 (252) C=C_r (*as*)	1650 (216) C=C_r (*as*)	1647 (252) C=C_r (*as*)

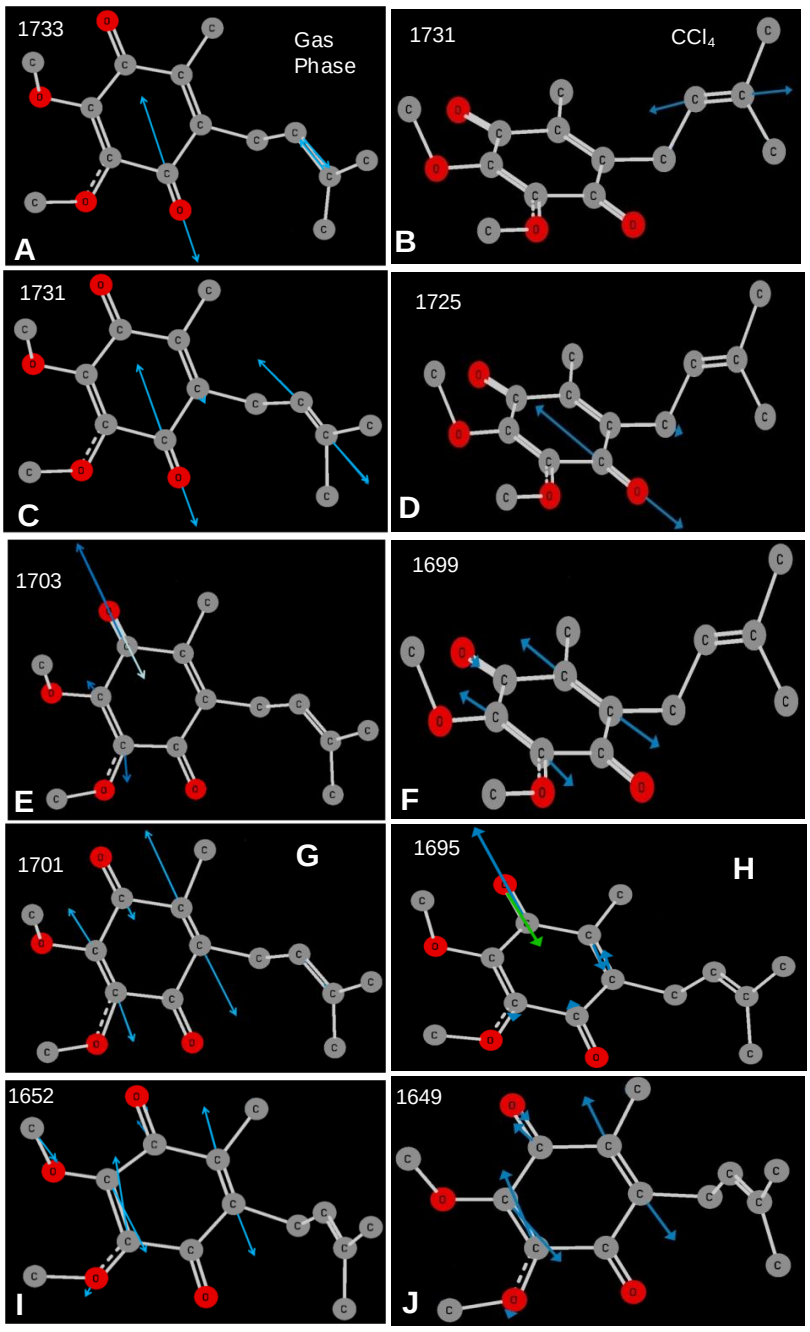

Fig. 2.5. Atomic displacements of selected vibrational modes of UQ_1_A in the gas phase (*left*) and in CCl_4 (*right*). The length of the arrows is representative of the magnitude of the movement of the atom upon vibration. The hydrogen atoms have been removed from the shown structures, so any C-H bending vibrations that are coupled to the modes shown will not be displayed.

In vibrational frequency calculations of 1,4-benzoquinone and 1,4-naphthoquinone models, both C=O groups are strongly coupled[40]. For UQ_1, however, the calculations predict that the two C=O modes are not coupled for conformers A-D in either gas phase or solvent calculations. In gas phase calculations the C=O modes are predicted to be coupled to $C=C_t$ modes. This appears not to be the case in solvent calculations, where the C=O modes are predominantly uncoupled from the $C=C_t$ modes. For example, in gas phase calculations, the 1733 and 1731 cm^{-1} modes of UQ_1 conformers A and B are due to anti-symmetric and symmetric coupled $C_1=O$ and $C=C_t$ vibrations, respectively. In CCl_4, however, the $C_1=O$ and $C=C_t$ vibrations are uncoupled, giving rise to individuals modes with frequencies of 1731 and 1725 cm^{-1}, respectively (Fig. 2.5). The same type of observations can be made for the uncoupling of the $C_4=O$ and $C=C_t$ vibrations of UQ_1 conformers C and D on going from the gas phase to solvent.

The mode-composition of the bands in the spectra in Fig. 2.4a and c depend on the conformer. For example, for UQ_1_A and UQ_1_B in the gas phase, the ~1703 cm^{-1} band is due in part to the $C_4=O$ vibration. For UQ_1_C and UQ_1_D, however, the ~1703 cm^{-1} band is due in part to the $C_1=O$ vibration (table 2.3). The same is found for the calculations in CCl_4.

2.4.5. Calculated infrared spectra for specifically labeled UQ_1

How the different vibrational modes contribute to a given spectral band is best visualized by comparing calculated spectra for unlabeled and specific isotope labeled UQ_1. Fig. 2.6 shows calculated IR spectra for unlabeled, $^{13}C_1$, $^{13}C_4$ and ^{18}O labeled UQ_1_A in CCl_4. The band at ~1724 cm^{-1} is downshifted 43 cm^{-1} upon $^{13}C_1$ labeling, but is unaffected by $^{13}C_4$ labeling. The ~1724 cm^{-1} band therefore contains a major contribution from the $C_1=O$ group, but not the $C_4=O$

group. The calculated isotope-labeled IR spectra for UQ_1_A (Fig. 2.6) do not resemble the results

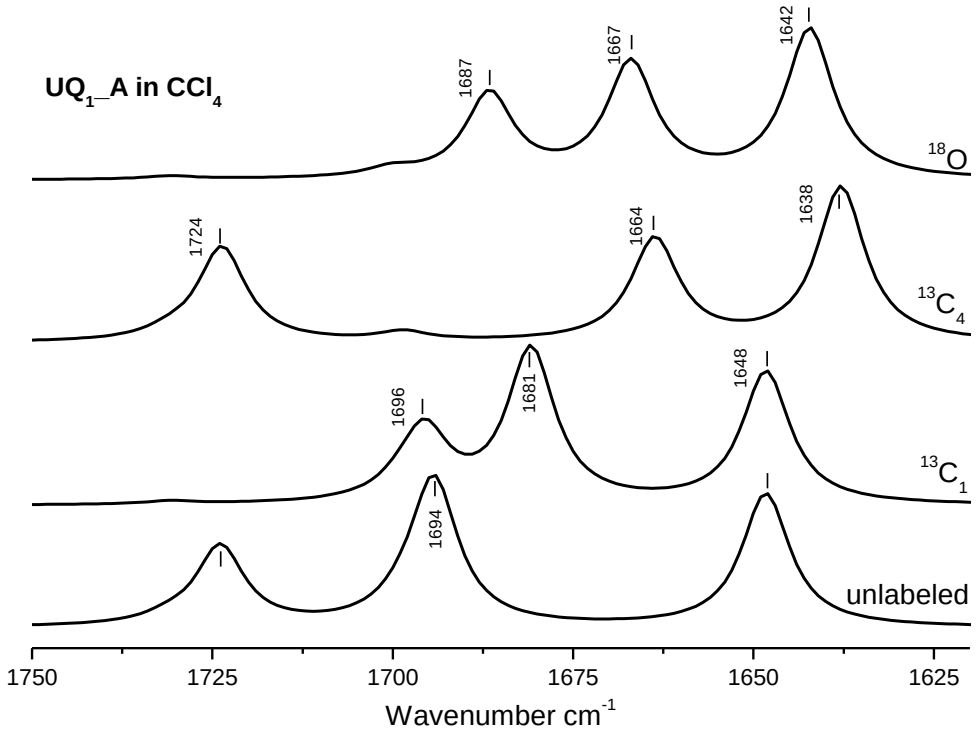

Fig. 2.6. Calculated IR spectra for unlabeled and specifically labeled UQ_1_A in CCl_4.

found experimentally (Fig. 2.2). Clearly, the experimental isotope-labeled spectra cannot be simulated by considering just a single conformation, such as UQ_1_A. The spectra of all eight conformers have to be considered. We have calculated spectra for all of the unlabeled and labeled conformers. From these spectra we have then produced a spectrum that is the sum of the Boltzmann weighted spectra of all eight conformers. The final spectra are shown in Fig. 2.7. The calculated spectra in Fig. 2.7 are in line with the experimental spectra in Fig. 2.2. To further highlight the similarities and differences between the experimental and calculated spectra, table

2.4 compares calculated and experimental isotope-induced vibrational frequency shifts for UQ_1 models in the gas phase and CCl_4.

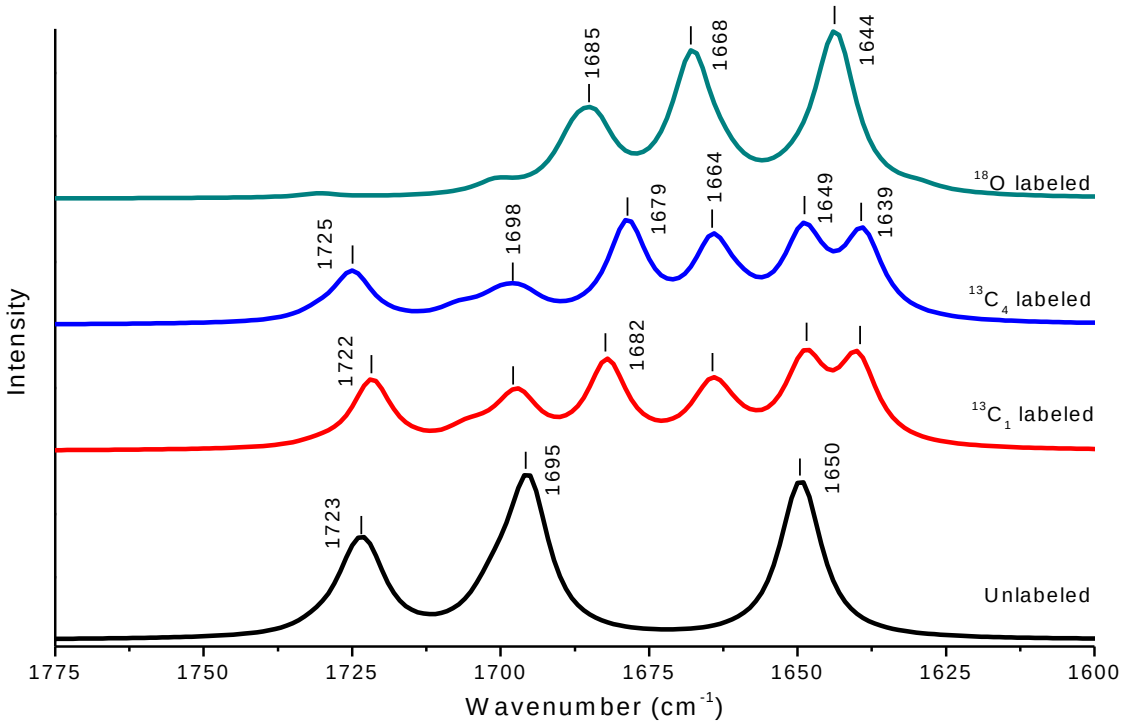

Fig. 2.7. Calculated IR spectra for unlabeled and specifically labeled UQ_1 in CCl_4. The spectra shown are the sum of the eight weighted spectra for each conformer.

Fig. 2.7 (and table 2.4) shows that the bands at 1723 and 1695 cm^{-1} are both impacted similarly by $^{13}C_1$ and $^{13}C_4$ labeling, with both bands down-shifting 41-47 cm^{-1} with either label. Experimentally it is found that the 1664/1650 cm^{-1} bands down-shift 40-45 cm^{-1}. In addition, a large part of the 1723 and 1695 cm^{-1} bands in the unlabeled UQ_1 spectrum are also found in the labeled spectra. This again is observed experimentally. The computed spectra thus model

excellently the experimentally observed $^{13}C_1$ and $^{13}C_4$ isotope-induced frequency down-shifts and relative intensity changes of absorption bands.

Upon ^{18}O labeling of UQ, the 1664 and 1650 bands down-shift 41 and 28 cm^{-1} (Fig. 2.2). The predicted down-shifts (Fig. 2.7) are 38 and 29 cm^{-1}. Again, there is excellent agreement between calculation and experiment.

The 1611 cm^{-1} band downshifts 5/10/10 cm^{-1} upon $^{18}O/^{13}C_1/^{13}C_4$ labeling of UQ, respectively. The calculations predict down-shifts of 8/10/11 cm^{-1} (table 2.4), respectively.

Table 2.4 Comparison between calculated and experimental isotope induced frequency shifts, for specific $^{13}C_1$ and $^{13}C_4$ labeling, and global ^{18}O labeling of UQ. Calculated data are for UQ_1 in the gas phase (A) and CCl_4 (B). Frequencies are in cm^{-1} and have not been scaled. Experimental band shifts are estimated from the data in Fig. 2.2.

Gas Phase							
	ν	ν (^{18}O)	Δν (^{18}O)	ν ($^{13}C_1$)	Δν ($^{13}C_1$)	ν ($^{13}C_4$)	Δν ($^{13}C_4$)
Calc.	1732	1693	39	1690	42	1690	42
Exp.	1663	1622	41	1618	45	1620	43
	1703	1671	32	1666	37	1668	35
	1650	1622	28	1611	39	1611	39
	1652	1646	6	1646	6	1646	6
	1611	1606	5	1601	10	1601	10
CCl_4							
Calc.	1723	1685	38	1682	41	1679	44
Exp.	1663	1622	41	1618	45	1620	43
	1695	1667	28	1664	31	1664	31
	1650	1622	28	1611	39	1611	39
	1649	1643	6	1640	9	1639	10
	1611	1606	5	1601	10	1601	10

2.5 Discussion

For neutral UQs in solution, the FTIR spectra are independent of the number of isoprene units in the chain, so long as there is at least one unit [25]. Our calculations suggest that this is because the C=O mode is either coupled to the C=C vibration of the first isoprene unit, or the C=C mode occurs as an independent vibration at similar frequencies to that of the C=O modes. The structural model outlined in Fig. 2.3 is likely the minimum required for any calculation aimed at modeling the vibrational properties of biologically relevant, poly-isoprene chain containing UQs. In some previous studies, UQ analogues containing a hydrogen atom at position 6 [26, 31], a methyl group at position 6 [26], or a prenyl unit with the methyl groups replaced with hydrogen atoms [27, 30] were considered. It may be unwise to extrapolate the results of these calculations to FTIR spectra obtained for poly-prenyl chain containing UQs embedded in protein complexes.

For neutral UQs in solution, the FTIR spectra show three bands. The 1650 cm^{-1} band is the most intense, followed by the 1611 cm^{-1} band then the 1664 cm^{-1} band, which is about 20% lower in intensity than the 1650 cm^{-1} band. Although experimentally observed band frequencies cannot be directly compared to calculated values without some kind of nonlinear scaling [41], the overall band pattern (which includes relative intensity information) may be expected to agree with calculation [39]. Comparing the spectra for unlabeled UQ in Fig. 2.2 with the calculated unlabeled spectrum in Fig. 2.7 confirm this expectation. We therefore associate the ~1723, ~1695 and ~1649 cm^{-1} bands in the calculated unlabeled spectrum in Fig. 2.7 with the 1664, 1650 and 1611 cm^{-1} bands in the experimental spectra. Such an association would suggest a scaling factor of 0.966-0.976 for the three bands, in the calculated spectrum (in CCl_4).

For the calculated averaged unlabeled spectrum shown in Fig. 2.7 the separation of the two, higher frequency (partly C=O) bands, is ~28 cm^{-1}. Experimentally the separation is ~14 cm^{-1} (Fig. 2.2). It is not entirely clear why DFT calculations poorly model this aspect of the experimental spectra. The problem is not related to the level of the calculation, however, since a virtually identical separation is calculated at the 6-31G++(p, d) level.

From semiempirical PM3 calculations of a UQ_1 model, the separation between the two C=O bands (at 1664 and 1650 cm^{-1}) appeared to be accurately modeled. In addition, the particular calculated isotope-induced frequency shifts that were presented appeared to be close to that observed experimentally [28]. However, the calculated intensities of the two C=O bands differed by about a factor of three. Experimentally the intensity difference between the 1664 and 1650 cm^{-1} bands is about 20% (Fig. 2.2). The spectra calculated at the PM3 level therefore do not accurately model the relative intensities of the bands in the experimental spectra. In addition, in the PM3 calculations [28], how the C=C bands (there was no discrimination between C=C tail and ring modes) were shifted upon labeling was never considered. In order to more fully assess the applicability of the calculations it is important to consider how all of the bands in the spectra are affected by labeling.

Experimentally, a portion of the band at 1611 cm^{-1} downshifts 10 cm^{-1} upon either $^{13}C_1$ or $^{13}C_4$ labeling (Fig. 2.2). In addition, the whole band downshifts 5 cm^{-1} upon ^{18}O labeling. From our calculated spectra in Fig. 2.7, approximately half of the 1650 cm^{-1} band downshifts ~10 cm^{-1} to 1640 cm^{-1} upon $^{13}C_1$ or $^{13}C_4$ labeling and the whole band downshifts 8 cm^{-1} upon ^{18}O labeling. The agreement between calculation and experiment is therefore extremely good. Fig. 2.5I indicates that the 1652 cm^{-1} band for UQ_1_A in the gas phase is due to the anti-symmetric

vibration of the C_2=C_3 and C_5=C_6 groups, coupled to the C_4=O vibration. For conformers C or D the anti-symmetric C=C quinine ring mode will couple to the C_1=O vibration.

In the calculated unlabeled spectrum shown in Fig. 2.7 the separation for the two lower frequency bands is ~45 cm^{-1}. Experimentally the separation is 39 cm^{-1} (Fig. 2). Our calculations do therefore appear to model well this separation between the two lower frequency bands.

It is now well established that the splitting of the C_1=O and C_4=O groups into independent modes for UQ is a consequence of the inequivalence of the two methoxy groups [42], with one being almost in the plane of the quinone ring and the other having a dihedral angle of ~120^o. We have considered four near-isoenergetic methoxy group conformations in this paper (Fig. 2.3). None of these conformations impact the orientation of the isoprene chain, which is directed at an angle of ~111^o above the quinone ring plane.

We have in fact considered a fifth stable UQ molecule with the methoxy groups having dihedral angles of +146^o and -129^o. This optimized conformation, however, is ~50 m*eV* higher in energy than that of the four conformations shown in Fig. 2.3, and a large population of this conformer is unlikely to exist in solution at room temperature. Our prediction is at odds with previous semi-empirical calculations of a similar conformer, which was predicted to be near iso-energetic with other conformations. In addition, the calculated IR spectrum for this fifth conformer is very different to that of the other four conformations, displaying bands associated with strongly coupled C=O groups. The FTIR spectra (as well as our calculations) rule out the possibility of a large population of this conformer being present in solution at room temperature. We note, however, that this type of conformation may be of some relevance in modeling the properties of UQ molecules in proteins, a subject we will address next.

2.6 Conclusions

We have accurately modeled experimentally observed relative band intensities found in spectra of neutral UQ in solution. We have also accurately modeled all observed ^{18}O, $^{13}C_1$ and $^{13}C_4$ isotope-induced frequency shifts found in FTIR spectra of neutral UQ in solution. Modeling of such a wide array of observables in UQ FTIR spectra has never been achieved previously. This is because the many features we consider in our modeling were not included previously. For example; the need for a UQ model containing a chain with one isoprene unit, consideration of several UQ methoxy group conformations, the need to include solvent effects in the calculation, and the level of theory that the calculations were undertaken.

For FTIR spectra in solution, two bands are found at ~1663 and ~1650 cm^{-1}. Calculations show that for any given UQ conformer the two C=O groups (C_1=O and C_4=O) separately give rise to these bands. Which C=O groups gives rise to each band, and the bands relative intensity, is dependent on the conformer considered. Our calculations predict that all four conformers will be present in roughly equal proportions in solution at room temperature. Therefore, the calculations predict that both the C_1=O and C_4=O groups of UQ contribute roughly equally to both the 1663 and 1650 cm^{-1} bands in the experimental spectra.

2.7 Supplementary Section

2.7.1 Supplementary Information Section 1

Figure 2.S1 shows the atom numbering scheme for geometry optimized UQ_1_B in CCl_4. The C_2/C_3 methoxy dihedral angles are $10.7^o/-121.7^o$, respectively. The difference between UQ_1_B and UQ_1_A is that the C_3 methoxy dihedral angle is -127.7^o instead of $+120.9^o$. Spectra calculated for UQ_1_A and UQ_1_B are virtually identical.

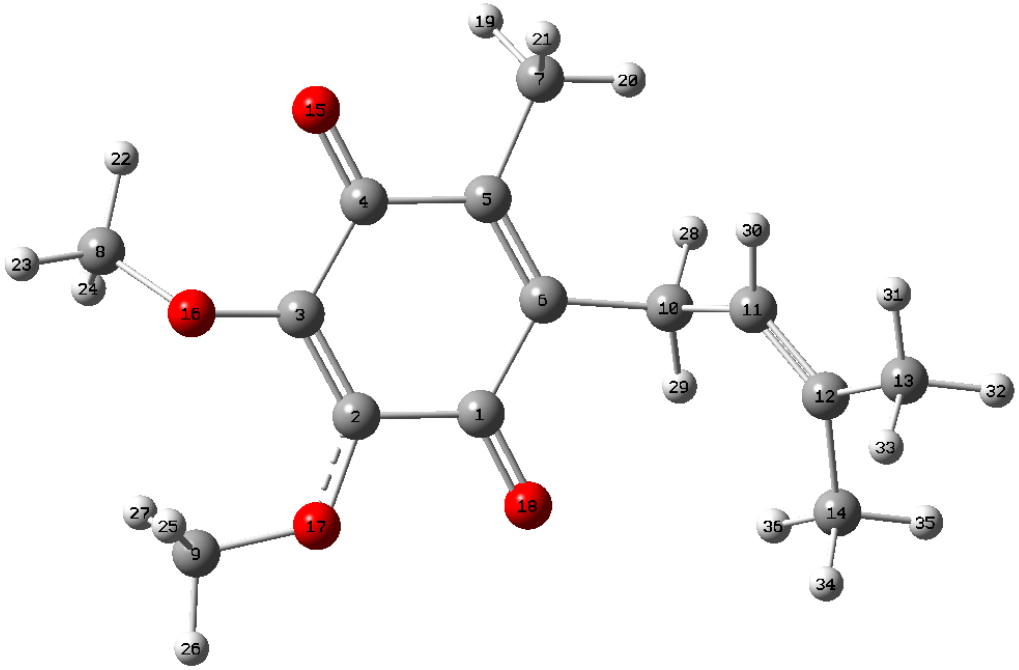

Figure 2.S1: Atom numbering scheme for UQ_1_B in CCl_4.

Table 2.S1 lists the atomic displacements (in Å, in Cartesian coordinates) for the 1649, 1696 and 1725 cm^{-1} normal modes of UQ_1_B. The data in Table 2.S1 quantifies the modes that are qualitatively outlined in Table 2B, and figures 4D, H and J of the manuscript.

Table 2.S1: Atomic displacements associated with three normal modes of UQ_1_B in CCl_4.

Frequency		1649				1696				1725	
Atom	X	Y	Z		X	Y	Z		X	Y	Z
1	-0.01	-0.01	0		-0.04	0.08	0.02		-0.42	0.65	0.2
2	-0.21	0.42	0.08		0	-0.1	0		0.03	-0.03	-0.01
3	0.31	-0.32	-0.12		-0.01	-0.01	0		0.03	0.01	-0.01
4	-0.14	0.13	0.06		-0.37	0.57	0.19		0.05	-0.08	-0.03
5	-0.15	0.26	0.06		0.13	-0.23	-0.06		-0.04	0.01	0.01
6	0.19	-0.24	-0.08		-0.09	0.17	0.04		0.05	-0.07	-0.02
7	0	-0.04	0		0	0.05	0		0	0	0
8	-0.03	0.01	0		-0.01	0.01	-0.01		0.01	0	0
9	-0.02	0	0		-0.01	0	0		0.01	-0.01	0
10	-0.03	0.02	0.02		0.01	-0.02	-0.01		-0.01	0.01	0.02
11	0.01	-0.01	0		-0.02	0.02	-0.01		-0.05	0.04	-0.03
12	-0.02	0.02	0		0.02	-0.02	0.01		0.05	-0.05	0.03
13	0	0	0		0	0	0		-0.01	0	0
14	0	0	0		0	0	0		-0.01	0.01	0
15	0.08	-0.08	-0.04		0.23	-0.36	-0.12		-0.03	0.05	0.02
16	-0.07	0.02	0.01		0.01	0.01	-0.01		-0.02	0	0.01
17	-0.02	-0.1	0		0.01	0.04	0		-0.01	0	0
18	0.02	0.01	-0.01		0.03	-0.07	-0.02		0.28	-0.42	-0.14
H-Atoms											
19	0	-0.15	-0.12		-0.07	0.09	0.1		0.01	-0.02	-0.02
20	-0.01	0.14	0.02		0.01	-0.27	-0.02		0	0.06	0.01
21	0.08	-0.15	0.06		-0.11	0.09	-0.01		0.03	-0.01	0.01
22	0.15	0	0.07		0.12	0	0.05		0	-0.01	-0.01
23	0.04	-0.05	0.09		0.02	-0.08	0.01		0.01	0	0
24	0.16	-0.09	0.03		0.01	-0.05	0.02		0	0.02	-0.01
25	0.14	0.08	0.04		0	-0.01	0.01		0	0	0
26	0.22	0.01	-0.03		-0.03	-0.01	0.01		-0.03	-0.01	0.01
27	0.12	0.11	-0.07		0	0	-0.01		0.01	0.01	0
28	0.08	-0.04	-0.03		-0.05	0.02	0.03		0.13	-0.06	-0.05
29	-0.16	0	-0.01		0.1	0.01	0		-0.01	0.08	-0.05
30	0	-0.01	0		0	0.01	0.01		0.03	0.01	0.04
31	-0.01	0	-0.01		0.01	0	0.01		0.02	-0.01	0.02
32	0	-0.01	0.02		-0.01	0.01	-0.02		-0.01	0.01	-0.02
33	0.02	0	0		-0.02	0	-0.01		-0.02	0	0
34	0.01	-0.01	-0.01		-0.01	0.01	0.01		-0.02	0.02	0.02
35	0	-0.02	0		-0.01	0.01	-0.01		-0.02	0.01	-0.04
36	0	0	0		0.02	-0.01	-0.01		0.06	-0.04	-0.04

CHAPTER 3
CALCULATED VIBRATIONAL PROPERTIES OF UBISEMIQUINONES

3.1 Abstract

Density functional theory has been used to calculate harmonic vibrational frequencies and intensities of the unlabeled and labeled 2,3-dimethoxy-5-methyl-6-polyprenyl-1,4-benzoquinone radical anion (ubisemiquinone) in both the gas phase and in solution (CCl_4). Raman activities were also calculated. Calculations for ubisemiquinone with different chain lengths (containing 1, 2, 3, 6 or 8 isoprene units) all gave similar results.

Single point energy calculations for ubisemiquinone with all possible methoxy group (dihedral angle) orientations were undertaken, and it is shown that only four methoxy group conformations are likely to be present in solution at room temperature. Boltzmann weighted spectra for the four conformers were calculated, and composite spectra that are the sum of the Boltzmann weighted spectra were produced. These composite spectra can be compared to experimental spectra. It is shown that the calculated composite spectra simulate well corresponding experimental FTIR and resonance Raman spectra.

Calculations show that the carbonyl modes and C=C modes of ubisemiquinone strongly mix with methyl torsional bending modes of the methoxy groups, resulting in complicated changes in mode frequencies, intensities and composition upon isotope labeling. Upon consideration of the calculated potential energy distributions of the normal modes of ubisemiquinone, and how they change upon isotope labeling, some of the peculiarities in previously published Raman and FTIR spectra can be explained

The calculated spectra for ubisemiquinone presented here provide a robust foundation from which to consider and assess future modeling of the vibrational properties of ubiquinone anion radicals in protein complexes.

3.2 Introduction

Ubiquinones (UQ_n: 2,3-dimethoxy-5-methyl-6-polyprenyl-1,4-benzoquinones) play an important role in biological electron and proton transfer processes that occur in both respiration and photosynthesis[20]. In photosynthetic reaction centers from purple bacteria, two UQ molecules, called Q_A and Q_B, act as terminal electron acceptors [4, 21]. In purple bacterial reaction centers (PBRCs)[3] from *Rhodobacter* (*Rb.*) *sphaeroides*, Q_A and Q_B are both ubiquinone-10 (UQ_{10}) molecules. Q_A and Q_B have very different functions, however. Q_A is an intermediary cofactor involved in transferring electrons from bacteriopheophytin to Q_B, while Q_B couples electron and proton transfer processes [4, 22, 23]. The very different redox functions of Q_A and Q_B is testimony to the flexibility of UQs in biological processes. Since Q_A and Q_B are both UQ_{10} molecules, pigment-protein interactions must modulate the functional properties of UQ_{10} in PBRCs. Elucidation of these pigment-protein interactions is at the heart of much current research in photosynthesis[13, 43].

Fourier transform infrared (FTIR) difference spectroscopy (DS) is a sensitive molecular-level probe of pigment-protein interactions, and it is widely used to study both the neutral and reduced states of the quinones occupying the Q_A and Q_B binding sites in PBRCs[24]. Although Q_A^-/Q_A and Q_B^-/Q_B FTIR difference spectra have been obtained under a wide range of conditions for

[3]Abbreviations: Density functional theory, DFT; difference spectra, DS; Fourier transform infrared, FTIR; infrared, IR; integral equation formalism; IEF; purple bacterial reaction centers, PBRCs; polarizable continuum model, PCM; PED potential energy distribution; ubiquinone, UQ; ubisemiquinone, UQ^-;

variously treated PBRC's, these spectra continue to be difficult to interpret because many bands not associated with the quinone also contribute to the spectra. Reconstitution of PBRCs with isotopically labeled quinones, however, has allowed some separation of the contributions of the quinones from those of the protein to the spectra[24]. Nonetheless the hypothesized band assignments in the experimental spectra, particularly those assignments associated with the ubiquinone anion radical, are still somewhat ambiguous and have not been modeled computationally. Here we present work aimed at modeling the vibrational properties of ubiquinone anion radicals (ubisemiquinone or UQ^{-}).

One basis for developing an understanding of bands in Q_A^{-}/Q_A and Q_B^{-}/Q_B FTIR DS is to first consider spectra of the relevant quinones in solution. Infrared (IR) absorption spectra [44, 45] and resonance Raman spectra [46] for ubisemiquinone in solution have been obtained. However, from a computational standpoint, even these simpler solution spectra are poorly understood. The work outlined in this manuscript is aimed at addressing this problem.

Few computational studies aimed at modeling the vibrational properties of ubisemiquinone (UQ^{-}) have been undertaken. The work that has been undertaken [31, 47] is limited in one way or another, for example tail-less quinone models in only the gas phase were considered, using relatively low-levels of theory. In this manuscript we describe the simulation of vibrational spectra associated with labeled and unlabeled tail-containing UQ anions in both the gas phase and in solvent using DFT methods employing appropriate functional and basis sets.

3.3 Materials and methods

3.3.1 Calculations. Molecular geometry optimizations and harmonic vibrational frequency calculations were performed using hybrid DFT methods, employing the B3LYP functional and the 6-31+G(d) method within Gaussian 03 [33, 48]. For calculations including solvent, the

integral equation formalism (IEF) [34-36] of the polarizable continuum model (PCM) [37, 38] was used. The potential energy distribution (PED) of normal modes were calculated using gar2ped[49].

Calculated normal mode vibrational frequencies presented here are unscaled. We choose to do this because we are primarily interested in vibrational frequency changes that occur upon isotope labeling, and we have shown previously that such frequency differences are accurately calculated without scaling[40, 50].

3.4 Results

3.4.1 UQ structure and numbering.

Figure 1A shows the structure and IUPAC numbering scheme for UQ_n. The subscript, *n*, refers to the number of isoprene units in the chain at C_6. The ubiquinone molecule has two carbonyl groups (C_1=O and C_4=O), two methoxy groups (C_3–O_{16}–C_8H_3 and C_2–O_{17}–C_9H_3), and a methyl group at C_5 and an isoprene unit at C_6. As outlined previously[50], only UQ models with a single isoprene unit are considered (UQ_1 or UQ_1^-). Figure 3.1B shows a geometry optimized UQ_1^- model with the atom numbering scheme and relevant internal coordinates displayed. The normal modes discussed in this manuscript will be expressed in terms of the contributions from the internal coordinates.

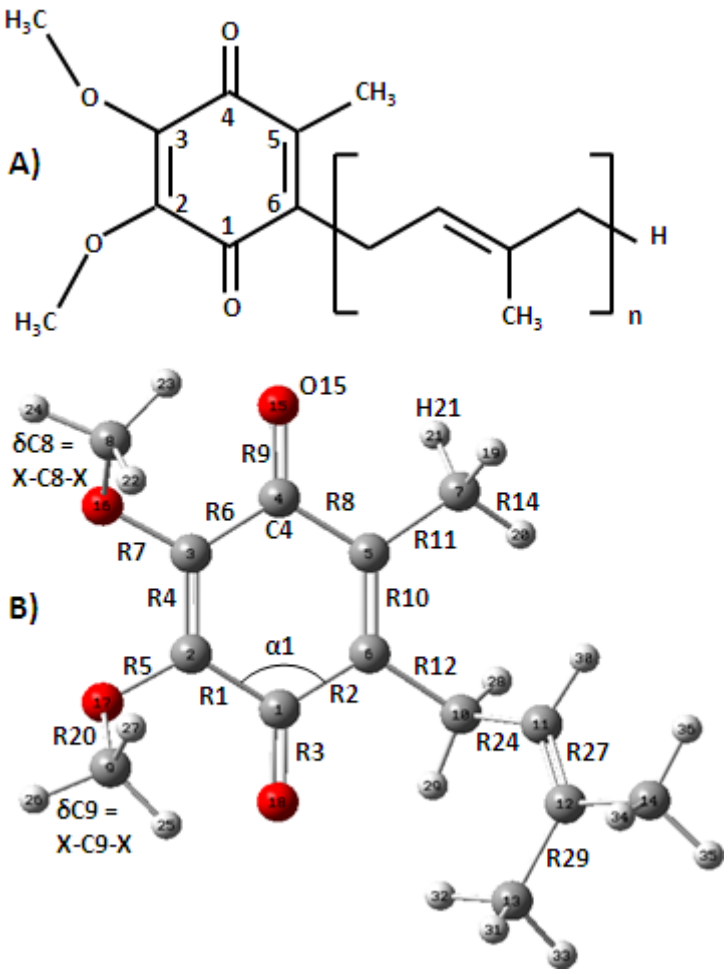

Figure 3.1. (A) Structure and IUPAC numbering scheme for UQ_n. The subscript *n* refers to the number of isoprene units associated with the chain attached at position 6. (B) Energy minimized UQ_1^- model used in calculations. The atom numbering scheme and a description of internal coordinates are shown. R represents bond stretching, α represents a bending of the angle between two bonds and δ represents and combination of angle bending centered at a vertex atom. For example R4 represents a C_2=C_3 stretching vibration, α1 represents a bending of the angle between the C_1=C_2 and C_1=C_6 bonds, and δC8 represents a bending vibration of the three C_8-H groups.

3.4.2 Calculated structure of ubisemiquinone$_1$.

(UQ_1^-) Previously we showed that neutral UQ_1 can adopt at least eight different methoxy group conformations at room temperature[50]. To establish which conformations may be present for UQ_1^-, single point energy calculations were undertaken for methoxy group dihedral angles that were stepped in 10^o increments. That is, 36x36 structures with fixed methoxy group dihedral angles were geometry optimized.

A contour plot of energy versus the C_2 and C_3 dihedral angles is shown in Figure 3.2. Figure 2 indicates four low energy UQ_1^- conformations, each with C_2 and C_3 dihedral angles close to ±120^o. The four conformers are labeled A, B, E and F, as shown in the figure. These four conformers are similar to the neutral UQ_1 conformers labeled J, L, I and K, respectively, that were described previously[50].

Following single point energy calculations the four UQ_1^- conformations were further geometry optimized (energy minimized) without constraining the dihedral angles. Calculations were undertaken for the four conformations in the gas phase and in CCl_4. Calculated bond lengths and the C–C–C bond angle for conformer F in both the gas phase and in CCl_4 are listed in Table 3.1A. Corresponding values for the other three conformers are within 0.0011 Å or 0.1^o. Data for UQ_{10}/UQ_{10}^- in the Q_A/Q_B binding site is also listed in Table 3.1A, respectively. The geometry optimized dihedral angles for the relative energies for the four low energy conformers in the gas phase and in CCl_4 are listed in table 3.1B. Corresponding data for UQ_{10}^- in the Q_B binding site is also listed in Table 3.1B.

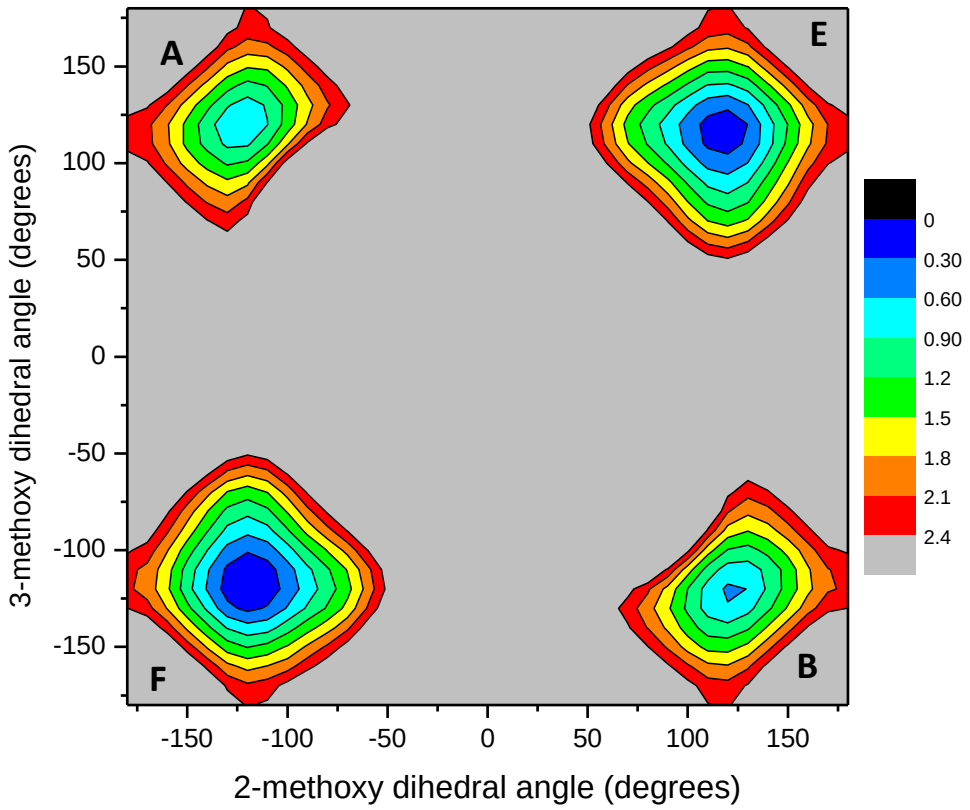

Figure 3.2. Calculated optimized energy (in kcal/mol) of ubisemiquinone$_1$ for all C_2 (C_3-C_2-O_{17}-C_9) and C_3 (C_2-C_3-O_{16}-C_8) dihedral angles. The energy axis was shifted so that the lowest energy conformer was set to zero.

Table 3.1B and figure 3.2 demonstrate that conformers E and F are very close in energy and considerably lower in energy than conformers A and B. Figure 3.3 shows the orientation of the methoxy groups of the four optimized conformers (in CCl_4). Conformers A and B have both methoxy groups on the same side of the quinone ring while conformers E and F have methoxy groups lying on either side of the quinone ring.

The dihedral angles of the methoxy groups of the conformers changed little upon optimization, and are within 10^o of that found for neutral UQ_{10} occupying the Q_A binding site in

the 1AIJ crystal structure. The dihedral angles are very different for the UQ^{-} occupying the Q_B binding site, however (table 3.1B). The hydrocarbon chain (isoprene unit) attached at C_6 makes a

Table 3.1. (A) Calculated bond lengths and bond angles for UQ_{1F}^{-} (conformer F) in the gas phase and CCl_4. Bond lengths for the other conformers are all within 0.0011 Å of that shown for conformer F. The C_6-C_{10}-C_{11} bond angle is also within 0.1° for all of the other conformers. Bond lengths and angles for neutral UQ_{10} in the Q_A binding site (1AIJ PDB file) and UQ_{10}^{-} in the Q_B binding site (1AIG PDB file) are also listed. (B) Calculated methoxy group dihedral angles and optimized relative energies for all conformers in the gas phase and in CCl_4. Conformer F is the lowest energy conformer in both the gas phase and CCl_4 calculations. The energy of conformer F is set to zero and the energies of UQ_1^{-} conformers relative to conformer F are listed. Methoxy group dihedral angles for neutral UQ_{10} in the Q_A binding site and UQ_{10}^{-} in the Q_B binding site are also listed.

A	Q_A	Q_B^{-}	CCl_4	GP
C_1⋯⋯O	1.2337	1.2273	1.2734	1.2731
C_4⋯⋯O	1.2320	1.2212	1.2736	1.2713
C_2⋯⋯C_3	1.4041	1.3788	1.3785	1.3792
C_5⋯⋯C_6	1.4191	1.3976	1.3846	1.3843
C_1–C_2	1.4003	1.4047	1.4564	1.4565
C_3–C_4	1.4045	1.3897	1.4555	1.4569
C_1–C_6	1.4130	1.3959	1.4612	1.4610
C_4–C_5	1.4070	1.4029	1.4587	1.4591
C_2–O	1.3929	1.3839	1.3805	1.3807
C_3–O	1.3937	1.3835	1.3805	1.3802
C_{11}⋯⋯C_{12}	1.3802	1.3729	1.3451	1.3450
C_6–C_{10}– C_{11}	113.0	111.0	113.2	113.5

B	At Binding Site		UQ_1^{-} in CCl_4			
	Q_A	Q_B^{-}	A	B	E	F
C_3–C_2–O–CH_3	-57.1	79.9	-118.5	116.1	111.8	-113.6
C_2–C_3–O–CH_3	109.5	-121.3	118.2	-117.7	111.6	-113.6
ΔE (kcal/mol)			0.4500	0.3870	0.0024	0
			UQ_1^{-} in GP			
C_3–C_2–O–CH_3			-121.8	120.8	116.7	-117.3

C_2–C_3–O–CH_3			122.4	-123.2	118.3	-119.0
ΔE (kcal/mol)			0.5366	0.6457	0.1062	0

distinct kink at C_{10}. The C_6–C_{10}–C_{11} angle is close to 113° for all four conformers. This angle is virtually the same as that found for the UQ_{10}/UQ_{10}^{-} molecule occupying the Q_A/Q_B binding site, respectively (table 3.1A).

The calculated carbonyl bond lengths of UQ^{-} in the gas phase and in CCl_4 are longer than the bond lengths of UQ_{10}^{-} in the Q_B binding site. The C_2⋯C_3 and C_5⋯C_6 bond lengths of UQ_1^{-} in the gas phase and CCl_4 are shorter than the corresponding values for neutral UQ_{10} in the Q_A binding site, but similar to that for UQ_{10}^{-} in the Q_B binding site.

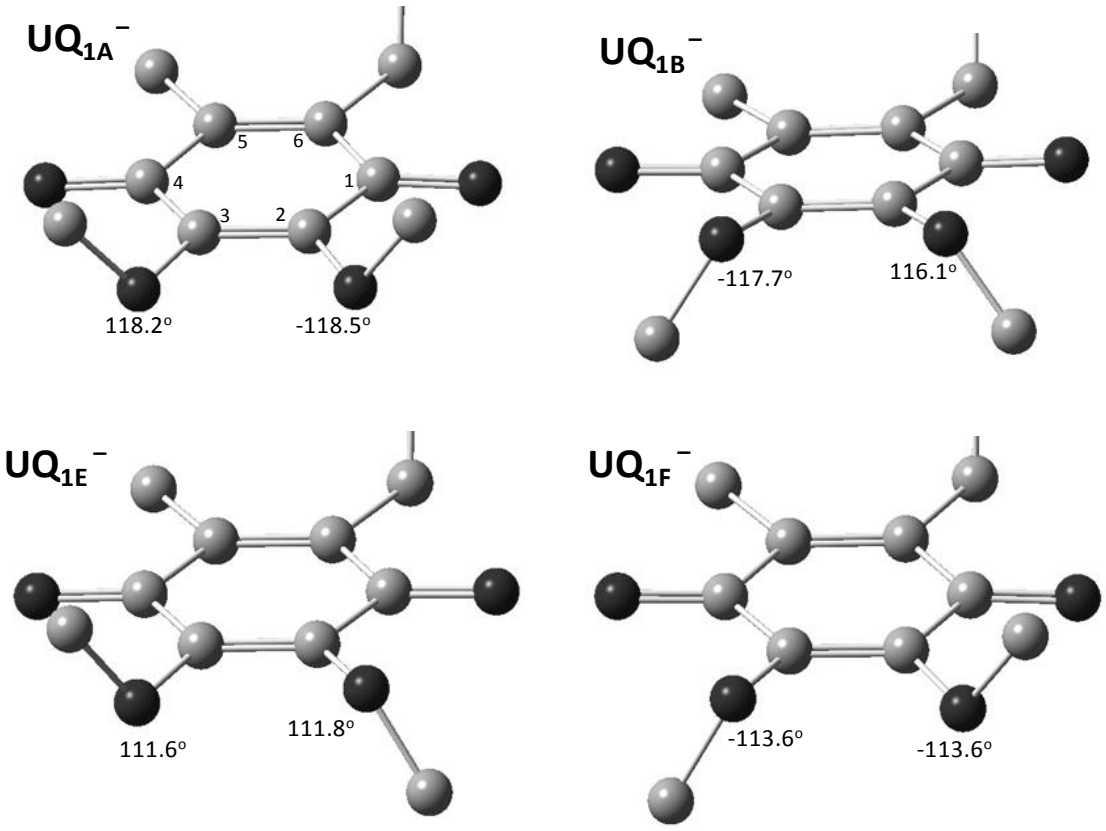

Figure 3.3: Structure of the four optimized methoxy group conformers. The emphasis is on displaying the methoxy group orientations, so hydrogen atoms have been removed and the tail at C_6 is not shown. Oxygen/carbon atoms are dark/light shade, respectively. Values for C_2 and C_3 dihedral angles are shown.

3.4.3 Calculated Vibrational Frequencies of UQ_1^-

Figure 4 shows calculated IR spectra for the four UQ_1^- conformers in (A) CCl_4 and (B) in the gas phase in the 1575-1450 cm^{-1} region. This spectral region is chosen because it is the region where the main C⋯O and C⋯C modes of UQ^- lie, and it is therefore the region generally focused upon in FTIR studies of UQ^- in solution [44, 45]. The spectra of the conformers in figure 3.4A and B have been scaled by the appropriate Boltzmann factors, which were calculated based on the relative energies of the four conformations (Table 3.1B). A composite spectrum which is the sum of the four Boltzmann weighted spectra is also shown in Figure 3.4A and 3.4B.

Figure 3.4A and 3.4B demonstrate that the spectra of all four conformers are very similar. The composite spectrum therefore closely resembles the spectrum of each conformer. For the calculated composite spectrum for UQ_1^- in CCl_4, an intense band is found at 1522 cm^{-1}. Lower intensity peaks are observed at 1553, 1512, 1500 and 1478 cm^{-1}. For the calculated composite spectrum for UQ_1^- in the gas phase, an intense band is observed at 1529 cm^{-1}. Peaks with considerably lower intensity are found at 1554, 1514, 1500 and 1475 cm^{-1}.

Table 3.2 lists the frequencies and intensities of the normal modes that contribute to the bands in the spectra of conformer F in CCl_4 (A) and in the gas phase (B). The mode compositions, frequencies and intensities for conformers A, B and E are very similar (all frequencies within a few cm^{-1} and all intensities within 5%).

The band at 1522 cm^{-1} in the composite spectrum in figure 4A is due to two high intensity normal modes at ~1520 and ~1524 cm^{-1}. The 1520 cm^{-1} normal mode is due predominantly to C_4⋯O stretching [R9(56%)] while the 1524 cm^{-1} normal mode is due predominantly to C_1⋯O stretching [R3(46%)]. For all four conformers, the C_1⋯O and C_4⋯O groups vibrate separately at a similar frequency with similar intensity. This is different from that found in calculations for neutral UQ_1 where most of the intensity is in only one of the C⋯O modes (the C_1=O or C_4=O mode of neutral UQ_1 that carries the intensity is conformation dependent)[50].

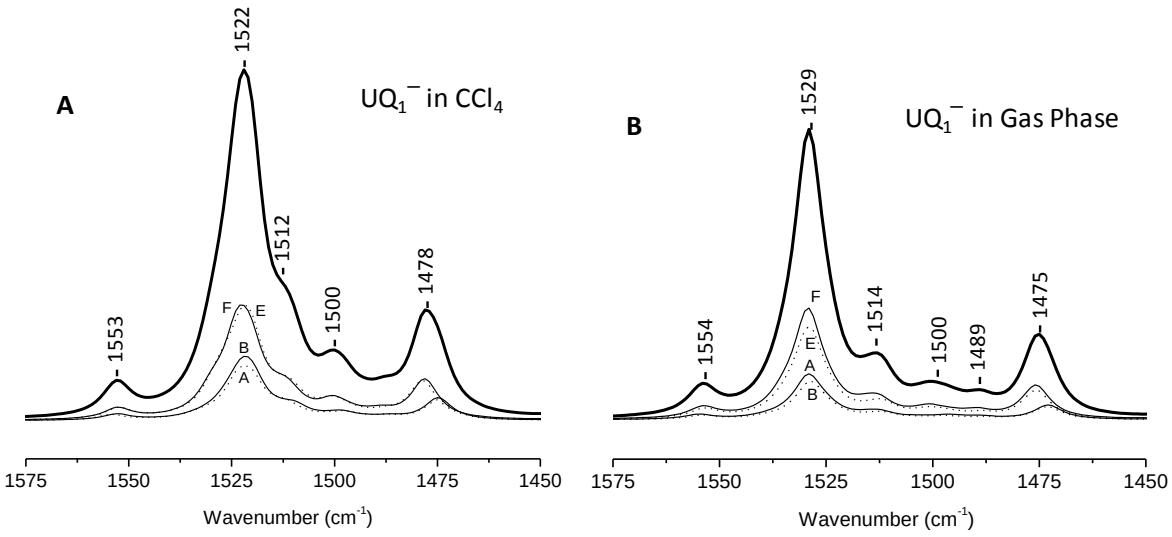

Figure 3.4. Calculated Boltzmann weighted IR spectra UQ_1^- conformations in (A) CCl_4 and (B) the gas phase in the 1575-1450 cm^{-1} region. UQ_{1A}^- (purple), UQ_{1B}^- (red), UQ_{1E}^- (blue) and UQ_{1F}^- (gray). The spectra of conformers A, B, E and F have been weighted by 0.1567, 0.1743, 0.3338 and 0.3352 in CCl_4, and 0.1568, 0.1304, 0.3245 and 0.3882 in the gas phase, respectively. A composite spectrum that is the sum of the Boltzmann weighted spectra of the four conformers is also shown.

The normal mode composition of the 1529 cm^{-1} band in gas phase calculation (figure 3.4B) also differs from the composition of the corresponding band at 1522 cm^{-1} for calculations in CCl_4. The 1529 cm^{-1} band in gas phase calculations is due mainly to the out-of-phase vibration of both C⋯O groups [R3(29%)-R9(27%)]. In the gas phase, the in phase vibration of both C⋯O groups is found at 1525 cm^{-1}, but it is approximately a factor of seven lower in intensity than the out-of-phase C⋯O vibration (Table 3.2B).

Table 3.2. Calculated vibrational frequencies, intensities, Raman activities, and potential energy distributions (in parenthesis in %) of selected normal modes of unlabeled UQ_{1F}^{-} conformers in (A) CCl_4 and (B) the gas phase.

A	ν (cm^{-1})	IR Intensity (km/mol)	Raman Activity ($Å^4$/amu)	Potential Energy Distribution
	1478	134	6	R3(5)-R1(5)+R6(5)+δC8(29)+δC9(23)
	1489	17	11	R3(9)+δC10(28)+δC7(27)+δC9(9)
	1520	184	328	R9(56)-R10(8)
	1524	238	163	R3(46)+δC13(14)+RD1(6)+δC7(5)+δC9(5)
	1553	36	27	R4(32)-R10(17)-R5(6)-R7(6)+δC7(6)
	1638	11	869	R4(27)+R10(23)+RD2(12)
B				
	1476	94	5	R1(6)-R6(5)+δC8(26)+δC9(25)
	1489	16	10	R3(9)-R10(5)+δC10(26)+δC7(31)+δC9(8)
	1525	33	247	R9(34)+R3(22)-R10(10))+δC7(8)
	1529	287	3	R3(29)-R9(27)+RD(9)+δC14(9)
	1554	30	21	R4(33)-R10(16)-R5(6)-R7(6)+δC7(6)
	1639	9	451	R4(26)+R10(23)+RD(12)

Ri = i^{th} bond stretching; δCi = X–C_i–X bending for -CH_3, –CH_2– and –CH= groups; X = atom bonded to C_i; RD1 = $6^{-1/2}$(α1-α2+α3-α4+α5-α6); RD2 = $12^{-1/2}$(2α1-α2-α3+2α4-α5-α6) = ring deformation; αi=C_{i-1}–C_i–C_{i+1} angle bending of ring atoms.

In gas phase calculations the in phase C⋯O vibration is very strongly Raman active while the out of phase C⋯O vibration is not. For calculations in CCl_4 both the C_1⋯O and C_4⋯O vibrations are strongly Raman active.

In the composite spectra in figure 3.4A and 3.4B the weak band at 1553-1554 cm^{-1} is due to an out-of-phase vibration of the C⋯C groups of the quinone ring (R4-R10). Given the antisymmetric nature of the vibration it is very weakly Raman active. The in-phase vibration of the C⋯C groups of the quinone ring occurs at 1638-1639 cm^{-1} and is IR silent but very strongly Raman active (Table 3.2). A relatively intense band is found at ~1478/1475 cm^{-1} in the composite spectrum in figure 3.4A/B, respectively, and is due predominantly to CH bending

vibrations of both methoxy methyl groups (δC8 and δC9) (Table 3). Given that the mode is due to CH bending vibrations of the methoxy methyl groups it is not surprising that the precise frequency of this normal mode varies by as much as 5 cm^{-1} among the four conformers in calculations in the gas phase or CCl_4 (Figure 3.4).

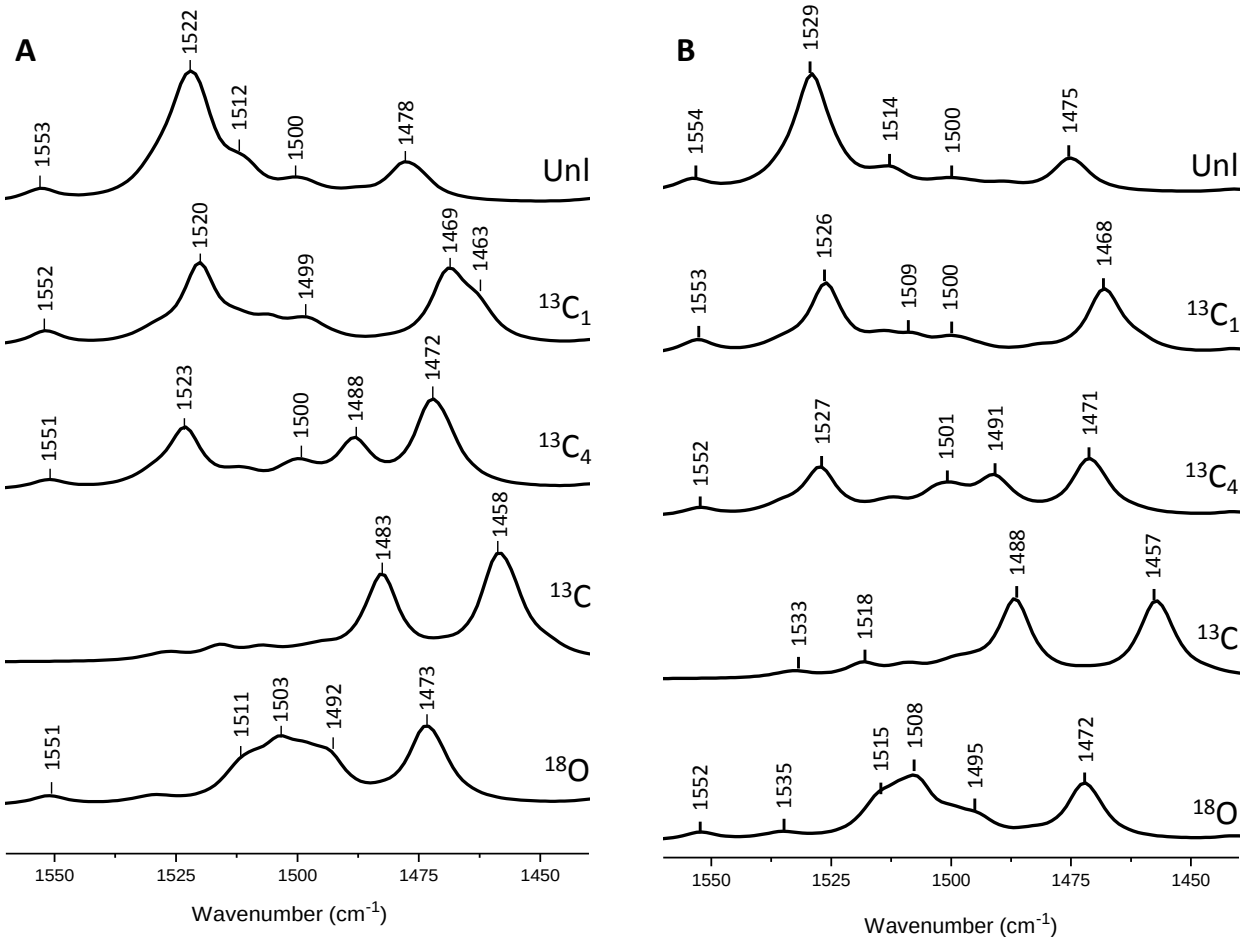

Figure 3.5. Calculated Boltzmann weighted composite spectra for unlabeled, $^{13}C_1$-, $^{13}C_4$-, ^{13}C- and ^{18}O-labeled UQ_1^- in (A) CCl_4 and in (B) the gas phase. For ^{13}C labeling all carbon atoms are labeled. For ^{18}O isotope labeling only the carbonyl oxygen atoms are labeled.

Table 3.3. Calculated vibrational frequencies (in cm^{-1}), intensities (in km/mol), Raman activities (in $Å^4$/amu), and potential energy distributions (in %) of $^{13}C_1$, $^{13}C_4$, ^{13}C and ^{18}O labeled UQ_{1F}^- in (A) CCl_4 and (B) in the gas phase.

A	ν	IR Intensity	Raman Activity	Potential Energy Distribution
				$^{13}C_1$
67	1463	79	61	δC9(36)+δC8(19)+R3(17)
68	1469	230	46	δC8(39)-R3(27)
69	1483	5	39	δC9(40)+δC8(15)-R3(11)+δC10(6)
71	1496	13	69	δC7(20)+δC14(20)+δC9(10)+δC10(9)+R3(7)+δC13(5)
75	1507	48	77	δC7(37)+δC9(18)-R3(9)+δC13(9)
78	1520	233	259	R9(57)-R10(7)
82	1552	43	18	R4(31)-R10(18)+δC7(7)-R7(6)-R5(6)
83	1635	18	818	R4(28)+R10(24)+RD2(11)
				$^{13}C_4$
64	1425	86	47	δC7(49)+R11(8)-R8(7)+R9(6)+δC14(5)
67	1465	5	30	δC8(43)+δC9(38)
68	1473	303	42	δC9(22)-R9(22)+δC8(11)+R6(7)
69	1488	30	122	R9(24)+δC10(18)+δC8(11)+δC7(9)+R3(7)-R10(7)
70	1489	102	61	δC9(16)+δC8(16)+R9(15)+δC7(19)+δC10(11)
78	1524	170	248	R3(49)+δC13(11)+δC7(7)+δC9(6)
82	1551	26	16	R4(30)-R10(20)+δC7(7)-R5(6)-R7(5)
83	1635	12	803	R4(29)+R10(24)+RD2(11)
				^{13}C
64	1412	51	33	δC7(79)+R11(7)+R9(5)
67	1449	21	42	δC9(28)+δC8(18)-R10(13)+R4(11)+R3(9)
68	1459	365	7	δC8(32)-R3(24)+R9(11)
69	1471	15	91	δC9(39)+R10(14)-R9(12)-R3(11)+δC7(6)
70	1483	243	48	R9(32)+δC8(27)+δC9(12)-RD1(6)
71	1486	17	156	R3(15)- R4(11)+δC9(8)+δC8(8)+R9(7)+R10(6)+δC7(12)
76	1502	7	190	δC9(38)+δC8(23)+δC7(11)-R3(6)-R9(6)
77	1507	27	34	δC13(39)+δC10(19)+δC14(14)+R3(6)
79	1516	39	16	δC7(28)+δC13(24)-R4(13)+δC14(5)
83	1579	9	752	R4(24)+R10(22)+RD2(11)
				^{18}O
68	1474	259	19	δC8(22)-R3(20)+R1(8)+δC9(6)-R6(6)
69	1483	9	101	δC9(24)-R3(17)+δC10(10)-R9(9)+δC7(8)+R10(6)
71	1494	97	131	R9(27)+δC7(18)+δC8(19)
75	1504	112	112	δC8(49)-R9(23)
76	1510	55	134	δC7(41)-R3(14)+δC9(10)
77	1512	52	49	δC14(52)+δC13(18)-R3(7)
82	1551	26	9	R4(30)-R10(21)+δC7(8)-R5(6)-R7(6)
83	1637	12	828	R4(28)+R10(24)+RD2(11)

B				
$^{13}C_1$				
67	1461	20	22	δC9(39)+δC8(30)+R3(8)
68	1469	179	28	δC8(32)-R3(25)+R1(6)
69	1482	11	32	δC9(36)-R3(18)+δC8(8)+δC10(7)
75	1508	30	51	δC7(44)-R3(11)+δC14(9)+δC9(11)
78	1526	183	124	R9(59)-R10(8)
82	1553	36	16	R4(31)-R10(17)- δC7(7)-R7(6)-R5(6)-R9(5)
83	1636	13	430	R4(28)+R10(24)+RD2(11)
$^{13}C_4$				
64	1423	59	29	δC7(50)+R11(8)-R8(7)+R9(6)
68	1472	165	11	δC9(27)+δC8(15)-R9(12)+R6(6)-R1(5)
69	1489	13	12	δC10(27)+δC7(30)+R3(10)+δC9(7)-R10(5)
70	1491	82	82	R9(39)+δC8(18)+δC7(8)
74	1503	14	77	δC8(43)-R9(11)+δC14(11)+δC13(12)
78	1527	128	111	R3(51)+δC10(6)+δC14(6)+δC7(5)
82	1552	21	15	R4(31)-R10(19)+δC7(7)-R5(6)-R7(5)
83	1636	13	420	R4(28)+R10(24)+RD2(11)
^{13}C				
67	1447	7	23	δC9(29)+δC8(22)+R4(12)-R10(11)+R3(6)
68	1458	218	6	δC8(35)-R3(20)+R9(8)+δC9(7)
69	1471	6	47	δC9(38)-R3(14)+R10(14)+δC7(7)-R9(6)
70	1486	13	61	R3(14)-R4(12)+δC9(10)+δC8(9)+R9(8)+δC7(6)+R10(6)
71	1487	195	25	R9(34)+δC8(22)+δC9(6)-RD1(6)-R10(5)
76	1503	8	130	δC8(32)+δC7(14)-R9(11)+δC9(20)-R3(6)
77	1509	23	23	δC14(37)+δC10(20)+δC13(13)+R3(7)
79	1519	34	18	δC7(33)-R4(15)+δC14(12)+δC13(5)
83	1580	7	384	R4(23)+R10(22)+RD2(11)
^{18}O				
68	1473	160	11	δC8(22)-R3(14)+δC9(12)+R1(8)-R6(6)
69	1484	11	53	R3(22)+δC9(21)+δC10(12)+δC7(8)-R10(6)+R9(5)
70	1494	10	33	δC14(24)+δC7(18)+δC13(16)+δC10(7)-R9(6)
71	1495	27	17	δC13(20)+δC7(19)+δC14(19)+R9(9)
75	1507	108	115	R9(37)+δC8(28)
76	1511	62	46	δC7(41)-R3(12)+δC14(5)
77	1515	46	33	δC13(57)+δC14(10)-R3(8)
78	1517	28	7	δC10(28)+δC13(23)+δC14(17)-R3(10)
82	1552	21	12	R4(31)-R10(20)+δC7(8)-R5(6)-R7(5)
83	1638	10	432	R4(27)+R10(24)+RD2(11)

Figure 3.4 shows that the calculated spectra of the four UQ_1^- conformers are very similar. We also find that the spectra are very similar for isotope labeled versions of the conformers. For this reason we will consider only the Boltzmann weighted composite spectra below. Figure 3.5 shows calculated spectra for unlabeled, $^{13}C_1$, $^{13}C_4$, ^{13}C and ^{18}O isotope labeled UQ_1^- in the gas phase (B) and CCl_4 (A). The normal modes (frequencies, intensities and PEDs) that give rise to the bands in the spectra in figure 3.5A and B are listed in tables 3.3A and B, respectively. The Raman activities of the normal modes are also listed in table 3.3.

As discussed above, for unlabeled UQ_1^- in CCl_4 the 1522 cm^{-1} band is due to separate C_4⋯O (R9-60%) C_1⋯O (R3-60%) vibrations. Upon ^{13}C labeling the 1522 cm^{-1} band appears to downshift 39 cm^{-1} to 1483 cm^{-1} (figure 5A) Such a downshift is expected for a band that is due to C⋯O groups. Table 3A indicates that the 1483 cm^{-1} band in the spectrum of ^{13}C labeled UQ_{1F}^- in CCl_4 is due to a C_4⋯O stretching vibration mixed with CH methyl bending (associated with both methoxy methyl groups). A very low intensity normal mode at 1486 cm^{-1} also contributes to the 1483 cm^{-1} band. This 1486 cm^{-1} mode is due to a C_1⋯O stretching vibration mixed with CH methyl bending vibrations associated both methoxy methyl groups. Similar ^{13}C isotope induced changes are found for calculations in the gas phase (Table 3.3B).

Upon ^{13}C labeling of UQ_1^- (in CCl_4) an intense band appears at 1459 cm^{-1}. The 1459 cm^{-1} mode is due to the out-of-phase vibration of both C⋯O groups (–R3(24%)+R9(11%)) coupled to C_3 methoxy methyl bending vibrations. Besides the two intense normal modes just discussed, C⋯O stretching vibrations (R9 and R3) contribute to at least 6 other modes in the 1510-1410 cm^{-1} region for ^{13}C labeled UQ_1^-. Similar observations to those discussed above can also be made upon consideration of calculations undertaken for ^{13}C labeled UQ_{1F}^- in the gas phase.

Upon specific $^{13}C_1$ and $^{13}C_4$ labeling of UQ_1^- in CCl_4 the C⋯O band at 1522 cm^{-1} decreases by approximately a factor of two in intensity in both cases. This is because the 1522 cm^{-1} band in the spectrum of the unlabeled species is due to two modes that are due to predominantly C_1⋯O or C_4⋯O vibrations, and only the contributions of one of these modes is downshifted upon specific $^{13}C_1$ or $^{13}C_4$ labeling. Upon $^{13}C_1$ labeling the C_1⋯O mode mixes with methyl bending vibrations, and the C_1⋯O stretching now contributes to several normal modes in the 1460-1500 cm^{-1} region (Table 3A). Upon $^{13}C_4$ labeling the C_4⋯O mode downshifts and, again, mixes with methyl bending vibrations (Table 3.3A).

In the unlabeled spectrum of UQ_1^- in CCl_4 the weak band at 1553 cm^{-1} is due predominantly to out-of-phase C⋯C vibrations (R4-R10). The in phase C⋯C vibration (R4+R10) occurs at 1635 cm^{-1} and has negligible IR intensity but very high Raman activity. The in phase C⋯C mode downshifts 61 cm^{-1} to 1579 cm^{-1} upon ^{13}C labeling with little change in the mode composition (table 3A). On the other hand the C⋯C out-of-phase vibration (at 1553 cm^{-1}) mixes considerably with methyl bending modes upon ^{13}C labeling, and the mode at 1486 cm^{-1} in the ^{13}C labeled species contains a contribution from the C⋯C out-of-phase vibration (Table 3.3A).

In the unlabeled species the relatively pure C⋯O modes are found near 1522 cm^{-1} (in CCl_4). Upon ^{18}O labeling these modes are expected to downshift ~40 cm^{-1} to ~1480 cm^{-1}. In the unlabeled species the methoxy-methyl bending mode is found at 1475 cm^{-1}. So, upon ^{18}O labeling the C⋯O modes and methyl bending modes will be similar in frequency, and will therefore strongly mix. Table 3 shows that upon ^{18}O labeling the C⋯O stretching vibrations do mix extensively with methyl bending vibrations, and that the C⋯O modes are distributed amongst at least five different mixed modes in CCl_4 (eight modes in the gas phase).

Table 3.4. Calculated and experimental frequencies of selected normal modes of UQ^{-}. Isotope induced frequency shifts are shown in parenthesis.

Mode	Unlabeled			^{13}C			^{18}O	
	Calc	Raman[a]	FTIR[b]	Calc	Raman[a]	FTIR[b]	Calc	FTIR[b]
C$\underline{\cdots\cdots}$C$_r$ (s)	1638	1605 Q_A 1613 Q_B 1608 Solvent		1579(59)	1556(49) Q_A 1555(58) Q_B		1637(1)	
C$\underline{\cdots\cdots}$C$_r$ (as)	1553	1523 Q_A 1532 Q_B 1522 Solvent	1483	1516(37) 1486(67) 1471(82) 1449(104)	1456(58) 1462(70)	1412(71)	1551(2)	
C$\underline{\cdots\cdots}$O	1522	1486 Q_A 1489 Q_B 1489 Solvent	1483	1483(39) 1458(64)	1456(30) 1462(27)	1442(41)	1512(10) 1510(12) 1503(19) 1493(29)	1468(15)

[a]Data from resonance Raman experiments [46]. [b]Data from FTIR experiments [44].

3.5 Discussion

The calculated changes in frequency, intensity and mode composition upon isotope labeling of ubisemiquinone are considerably more complex than that found for the neutral species. In spite of this, however, the calculated data allow a very detailed interpretation of bands in Raman and FTIR spectra of ubisemiquinones.

3.5.1 Modeling Isotope Induced Bandshifts Observed in Resonance Raman Spectra

Resonance Raman spectra of unlabeled and ^{13}C labeled UQ_{10}^{-} in the Q_A and Q_B binding sites in purple bacterial reaction centers have been obtained [46]. For comparison, resonance Raman spectra of unlabeled UQ_{10}^{-} in solution were also obtained [46]. For both *in vivo* and *in vitro* cases an intense Raman band was observed near 1608 cm^{-1}, with two weaker bands observed near 1523 and 1488 cm^{-1} (Table 3.4). For UQ_{10}^{-} in the Q_A/Q_B binding site the ~1608 cm^{-1} band was assigned to a C$\underline{\cdots\cdots}$C mode, weakly coupled to a C$\underline{\cdots\cdots}$O mode, because it downshifted 49/58 cm^{-1} upon ^{13}C labeling, respectively (Table 4). The ~1488 cm^{-1} band was assigned to a C$\underline{\cdots\cdots}$O mode because it downshifted 27-30 cm^{-1} upon ^{13}C labeling (Table 3.4). The ~1523 cm^{-1} band disappeared upon ^{13}C labeling. It was suggested, however, that the ~1523 cm^{-1} band was also due to a C$\underline{\cdots\cdots}$C mode [46]. Although not suggested in the original manuscript, it is possible that

(part of) the 1523/1532 cm^{-1} band of UQ_{10}^- in the Q_A/Q_B binding site downshifts 58-70 cm^{-1} to 1456/1462 cm^{-1} upon ^{13}C labeling, and is masked by the C⋯⋯O band at 1456/1462 cm^{-1}, respectively (Table 3.4).

Given the similarity of the UQ_{10}^- *in vivo* and *in vitro* resonance Raman spectra it was suggested that the distribution of the charge over the quinone ring was similar in both environments. Corresponding FTIR data do not support this interpretation, however (see below).

The calculated data presented here allow a detailed assessment of these experimental resonance Raman spectra. The C⋯⋯C tail stretching vibration of UQ_1^- is calculated to be near 1730 cm^{-1} with negligible IR intensity but strong Raman activity (not shown). This C⋯⋯C tail vibration is not observed in resonance Raman spectra because the molecular group is distant from the quinone ring. Since no information is available from experiment on this C⋯⋯C tail vibration it will not be considered further.

In calculations the C_2⋯⋯C_3 and C_5⋯⋯C_6 stretching vibrations of the quinone ring couple to give C⋯⋯C ring in-phase and out-of-phase vibrations. For UQ_1^- in CCl_4 the C⋯⋯C ring in phase vibration is at 1635 cm^{-1} (table 3.2A). This is 86 cm^{-1} higher in frequency than the out-of-phase vibration. Unlike the out of phase vibration, the C⋯⋯C ring in phase vibration is not coupled with methyl bending and carbonyl stretching modes (table 3.2A). The C⋯⋯C in phase vibration has negligible IR intensity but huge Raman activity. It is basically unaffected by ^{18}O, $^{13}C_1$ and $^{13}C_4$ labeling, but downshifts 59 cm^{-1} upon ^{13}C labeling (table 3.4). The intensely Raman active band calculated at 1638 cm^{-1} for UQ_1^- clearly corresponds to the band observed at ~1608 cm^{-1} experimentally[46].

The out-of-phase C⋯⋯C ring vibrational mode at 1553 cm^{-1} mixes with methyl bending vibrations upon ^{13}C labeling and is not easily identifiable. In table 3A a mode is calculated at

1486 cm^{-1}. The out of phase C⋯⋯C vibration contributes 17% to the PED of this mode. We associate the calculated band at 1553 cm^{-1} with the band observed at ~1521 cm^{-1} in resonance Raman spectra of UQ_{10}^- in solution [46]. We also suggest that this 1553 cm^{-1} mode downshifts 67 cm^{-1} to1486 cm^{-1} upon ^{13}C labeling of UQ_{10}^- (Table 3.4). If this is the case then it will overlap with a band due to a C⋯⋯O mode of ^{13}C labeled UQ_{10}^- at 1483 cm^{-1} (Table 4). Given the validity of the above observations, our calculated data provides a reasonable explanation as to why the ~1521 cm^{-1} resonance Raman band that is observed experimentally is not identified upon ^{13}C labeling[46].

Bands at 1486/1489 cm^{-1} in resonance Raman spectra of UQ_{10}^- in the Q_A/Q_B binding site downshift 30/27 cm^{-1} upon ^{13}C labeling of UQ_{10}^- (Table 3.4). They were therefore associated with C⋯⋯O modes coupled to C⋯⋯C modes. Computationally, we find two C=O modes at 1520 and 1524 cm^{-1} that downshift 30 and 27 cm^{-1} upon ^{13}C labeling of UQ_1^- (Table 3.4). The calculated data are in excellent agreement with the experimental data. We note that bands in the experimental spectra are very broad, and isotope induced frequency shifts are difficult to determine precisely.

3.5.2 Modeling Isotope Induced Bandshifts Observed in FTIR Spectra

Electrochemically generated FTIR difference spectra of UQ_1 and UQ_{10} in various solvents have been obtained[40]. For UQ_{10}^- in acetonitrile, THF or dichloromethane a single intense FTIR absorption band was observed at 1483-1488 cm^{-1}. The observation of single intense band in experimental FTIR spectra of UQ_{10}^- and UQ_1^- in solution is in line with our calculated IR spectra which are dominated by an intense band at 1522/1529 cm^{-1} for UQ_1^- in CCl_4/gas phase, respectively.

Although there are differences in the mode compositions that contribute to the bands in the spectra in the gas phase and in CCl_4, the calculated isotope induced frequency shifts and intensity changes of bands are similar in both gas phase and solvent calculations (figure 3.5). Based on the available calculated data therefore, it appears that modeling of the solvent is not required to more accurately simulate the experimental FTIR spectra.

For UQ_{10}^- in dichloromethane, upon ^{13}C labeling the 1483 cm^{-1} band downshifted 41 cm^{-1} to 1442 cm^{-1} (Table 3.4)[44]. From figure 3.5A it can be seen that upon ^{13}C labeling the 1522 cm^{-1} band appears to downshift 39 cm^{-1} to 1483 cm^{-1}. This calculated result agrees very well with the experimental observation.

For UQ_{10}^- in dichloromethane, upon ^{18}O labeling of the carbonyl oxygen atoms, a band at 1483 cm^{-1} downshifts 15 cm^{-1} to 1468 cm^{-1}. In figure 5A, it is not entirely clear what happens to the 1522 cm^{-1} band upon ^{18}O labeling. It could downshift 10, 12, 19 or 29 cm^{-1} to 1512, 1510, 1503 or 1493 cm^{-1} respectively (Table 3.4). The calculated PED's in table 3.3 show how complicated the situation actually is: The 1524 and 1520 cm^{-1} modes of unlabeled UQ_{1F}^- are due to R3(46%) and R9(56%), respectively. Upon ^{18}O labeling modes appear at 1504 [R9(23%)] and 1494 cm^{-1} [R9(27%)]. Thus the 1520 cm^{-1} mode in the unlabeled species appears to split and downshift 16 and 26 cm^{-1} upon ^{18}O labeling. The former is in excellent agreement with experiment [44]. Upon ^{18}O labeling modes appear at 1512 [R3(7%)] and 1510 cm^{-1} [R3(14%)]. Thus the 1524 cm^{-1} mode in the unlabeled species therefore also appears to split and downshift 12 and 14 cm^{-1} upon ^{18}O labeling. Again, these conclusions are in agreement with experiment[44].

From electrochemically generated FTIR difference spectra of ^{13}C labeled UQ_{10}^- in various solvents [44] a band was observed at 1412 cm^{-1}. It was suggested that this band was due to a ^{13}C

C=^{13}C vibration that was downshifted 71 cm^{-1} from 1483 cm^{-1} in the unlabeled species. Neither the calculated data presented here, nor the resonance Raman data presented previously support this hypothesis. However, we observe that a 72 cm^{-1} band shift (figure 5 B) is not due to C=C vibration but results from band coupling between carbonyl modes and methyl bending modes up on ^{13}C labeling.

3.5.3 Experimental Q_A^-/Q_A and Q_B^-/Q_B FTIR DS

Q_A^-/Q_A and Q_B^-/Q_B FTIR DS have been obtained using purple bacterial reaction centers (PBRCs) from *Rb. sphaeroides[24]*. In Q_A^-/Q_A FTIR DS three intense IR bands are observed near 1485, 1466 and 1449 cm^{-1}[14, 16, 24]. On the basis of ^{18}O, ^{13}C, $^{13}C_1$ and $^{13}C_4$ labeling the 1486/1466 cm^{-1} bands were assigned to C=O/C=C vibrations, respectively[16]. The modes were suggested to be considerably mixed. The origin of the 1449 cm^{-1} band was not considered. Another group, which undertook identical labeling experiments [14], assigned the 1485 cm^{-1} band to a C_1=O vibration, the 1466 cm^{-1} band to C_4=O vibration, and the 1447 cm^{-1} band to C=C vibration. All modes were suggested to be strongly mixed.

Our calculated spectra for UQ_1^- in solution poorly model observed FTIR bands of UQ^- in the Q_A binding site. For UQ^- in the Q_A binding site, the C=O modes appear to be separated by 19 cm^{-1}. In calculations in solvent the two C=O modes do appear to be distinct, although the separation of the modes is only 4 cm^{-1}. In gas phase calculations the two C=O modes are coupled. The separation of C=O modes of UQ^- in the Q_A binding site is due to asymmetric interactions with the protein environment. Calculations of UQ^- in solvent cannot model these interactions. Calculations including effects of the protein environment are essential. Such calculations are underway in our lab and will be presented elsewhere.

3.5.4 Previous Calculations of Ubisemiquinones

Density functional theory based vibrational frequency calculations (using the BP86 functional) have been undertaken for 2,3-dimethoxy-1,4-benzoquinone and 2,3-dimethoxy-5,6-dimethyl-1,4-benzoquinone in the gas phase [47]. Comparison of calculated data for the two models showed that substituents at C_5 and C_6 are required in order to better model the properties of ubiquinones and ubisemiquinones. In the above study isotope shifts were calculated. How the C⋯O and C⋯C modes couple with each other, and with CH methoxy methyl bending vibrations was not considered, however. As we have shown above, the extent of mode mixing can be considerably altered upon labeling, making it difficult to identify how the different bands shift upon labeling. As we also show here, the detailed PED's are a crucial tool in the analysis of how calculated bands shift upon isotope labeling.

3.6 Conclusions

We calculate that four UQ_1^- conformers are likely present in solution at room temperature. Calculated IR spectra for all four UQ_1^- conformers are very similar. Calculated IR spectra of unlabeled and isotope labeled UQ_1^- in the gas phase and in solution are very similar, although there are some differences in the composition of the modes that contribute to the bands in the spectra. Based on a consideration of calculated vibrational frequencies and intensities, as well as isotope induced frequency shifts, it appears that inclusion of the solvent in calculations does not give result that better model the experimental data.

Calculations show that upon isotope labeling the out-of-phase C⋯C ring modes and C⋯O modes of UQ_1^- strongly couple with methyl C-H bending vibrations. This leads to complicated splitting of modes and unusual downshifts upon isotope labeling. Nonetheless by consideration of PED's of the calculated normal modes, sense can be made of the isotope induced shifts and intensity changes, and it is shown that the calculated data provide a rational and detailed

interpretation of experimentally observed isotope induced band shifts in experimental FTIR and Raman spectra of UQ_1^- in solution.

CHAPTER 4

CALCULATED VIBRATIONAL PROPERTIES OF PIGMENTS IN PROTEIN BINDING SITES

4.1 Abstract

FTIR difference spectroscopy is widely used to probe molecular bonding interactions of protein-bound electron transfer cofactors. The technique is particularly attractive because it provides information on both neutral and radical cofactor states. Such dual information is not easily obtainable using other techniques. Although FTIR difference spectroscopy has been used to study cofactors in biological protein complexes, in nearly all cases interpretation of the spectra has been purely qualitative. Virtually no computational work has been undertaken in an attempt to model the spectra. To address this problem we have developed the use of ONIOM (our own N-layered integrated molecular Orbital + Molecular mechanics package) (quantum mechanical:molecular mechanics) methods to calculate FTIR difference spectra associated with protein-bound cofactors. As a specific example showing the utility of the approach we have calculated isotope edited FTIR difference spectra associated with unlabeled and labeled ubiquinones in the Q_A binding site in Rhodobacter sphaeroides photosynthetic reaction centers. The calculated spectra are in remarkable agreement with experiment. Such agreement cannot be obtained by considering ubiquinone molecules in the gas phase or in solution. A calculation including the protein environment is required. The ONIOM calculated spectra agree well with experiment but indicate a very different interpretation of the experimental data compared to that proposed previously. In particular the calculations do not predict that one of the carbonyl groups of Q_A is very strongly hydrogen bonded. We show that a computational-based interpretation of

FTIR difference spectra associated with protein-bound cofactors is now possible. This approach will be applicable to FTIR studies of many cofactor-containing proteins.

4.2 Introduction

Ubiquinones play an important role in biological electron and proton transfer processes that occur in both respiration and photosynthesis (1). In photosynthetic reaction centers from purple bacteria, two ubiquinone (UQ) molecules, called Q_A and Q_B, act as terminal electron acceptors (2). In Rhodobacter (Rb.) sphaeroides purple bacterial reaction centers (PBRCs), Q_A and Q_B are both ubiquinone-10 (UQ_{10}) molecules. Q_A and Q_B have very different functions, however. $_{QA}$ is an intermediary cofactor involved in transferring electrons from bacteriopheophytin to Q_B, whereas Q_B couples electron and proton transfer processes (3, 4). The very different redox functions of Q_A and Q_B is testimony to the flexibility of UQs in biological processes. Because Q_A and Q_B are both UQ_{10} molecules, pigment–protein interactions must modulate their functional properties. Elucidation of how protein interactions modulate the functional properties of quinone cofactors is at the heart of much current research in photosynthesis (5, 6).

FTIR difference spectroscopy is a sensitive molecular-level probe of pigment–protein interactions, and it is widely used to study both the neutral and radical states of cofactors in a range of protein complexes (7–9). In particular, it has been widely used to study both the neutral and reduced states of quinones in PBRCs (10). Q_A^-/Q_A and Q_B^-/Q_B FTIR difference spectra (DS) were first obtained in the early 1990s (11) and were difficult to interpret because many bands not associated with the quinines also contributed to the spectra. Reconstitution of PBRCs with isotopically labeled quinones, however, has allowed some separation of the contributions of the quinones from those of the protein in Q_A^-/Q_A and Q_B^-/Q_B FTIR DS (10).

Q_A^-/Q_A FTIR DS obtained for PBRCs with specific isotope labeled quinones incorporated (12, 13) indicate that the vibrational frequency of the C_1═O group of Q_A is similar to that found for nonhydrogen (H) bonded UQ in solution, whereas the vibrational frequency of the C_4═O group is downshifted 50–65 cm^{-1} compared to that found for UQ in solution. From these results it was concluded that the C_1═O group of Q_A is very weakly H-bonded, whereas the C_4═O group is very strongly H-bonded (12, 13). These conclusions are not supported by crystal structural models (Fig. 1B) and other types of FTIR spectroscopic data (6, 14).

Although experimental Q_A^-/Q_A FTIR DS have been obtained under a myriad of conditions, very little work has been undertaken with the aim of modeling the experimental FTIR DS, and in particular computational work aimed at modeling the very large downshift in frequency of the Q_A C_4═O mode. Several studies have been undertaken to assess the vibrational properties of UQs in solution [(15) and articles cited therein]. However, based on the available experimental data, it is clear that the vibrational properties of neutral UQ in solution (frequencies and intensities of the C═O and C═C modes) are quite different from the properties of the UQ occupying the $_{QA}$ binding site. The protein environment clearly modifies the vibrational properties of the pigment. Any calculations undertaken to model the (vibrational) properties of UQ in the Q_A binding site must therefore include or account for this protein environment. Quantum mechanical (QM) calculations of such a large molecular system are unfeasible. However, methods have been developed that allow one to "parse" the problem into distinct layers. In one layer the chemical properties of the principal species (the pigment) can be calculated at a QM level, whereas the surrounding protein environment is included and calculated using less computationally expensive molecular mechanics (MM) methods. Here we have implemented such QM:MM calculation for UQ in the Q_A binding site using the ONIOM

method (16, 17). ONIOM is an acronym for our own N-layered integrated molecular Orbital + Molecular mechanics package. In our calculations the quinone is treated at the QM level using density functional theory (DFT) based methods, whereas the protein environment is treated at the MM level using AMBER (Assisted Model Building with Energy Refinement) (18).

In an attempt to model the unique vibrational properties of the Q_A C_4═O group, Nonella and coworkers (19) used a QM:MM method to calculate the vibrational properties of a UQ molecule in the $_{QA}$ site. They showed that they could model the large frequency downshift of the Q_A C_4═O mode. They also showed that the downshift was mainly due to the charge on the nonheme iron atom and not to a strong H bond. The software used for these calculations is not widely available, and the conclusions derived from their calculations have never been tested/ verified. Below we show that conclusions derived from these previous calculations are incorrect.

Here we present ONIOM-based calculations aimed at modeling experimental isotope edited Q_A^-/Q_A FTIR DS obtained using PBRCs. All of our calculated spectra are found to agree well with corresponding experimental spectra. However, our calculations show that a strongly H-bonded C_4═O group of UQ in the Q_A binding site is not required in order to explain the experimental spectra.

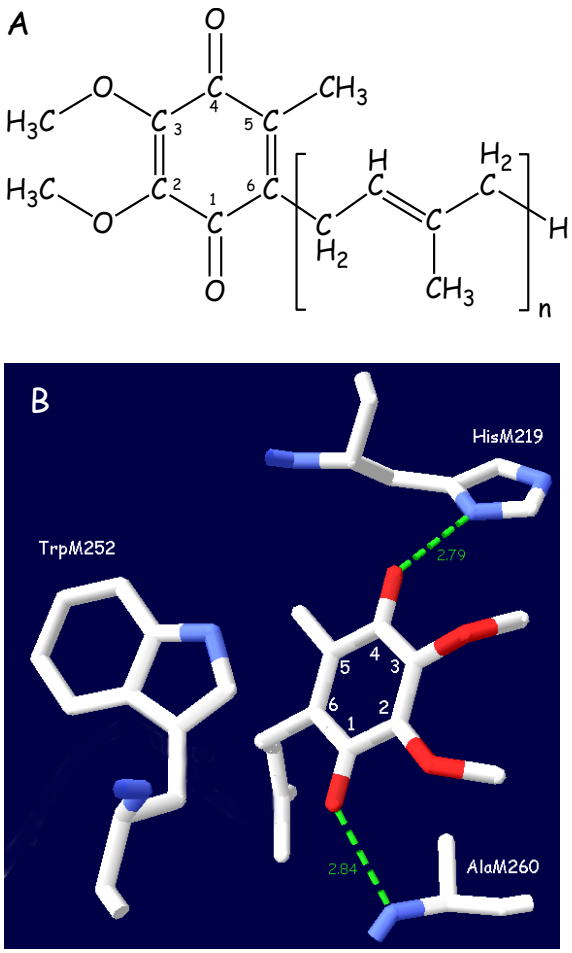

Figure 4.1: (A) Structure and IUPAC numbering scheme for UQ_n. The subscript *n* refers to the number of isoprene units in the chain attached at position 6. (B) Structure of UQ_{10} and some surrounding amino acids in the $_{QA}$ binding site in PBRCs from *Rb. sphaeroides*. Picture was derived from the crystal structure PDB file 1AIJ. The green dotted lines represent possible H-bonds and the distances are in Å. The non-heme iron atom is ligated to the second imidazole nitrogen atom of HisM219. The iron atom is 2.08 Å from the imidazole nitrogen atom. The UQ_{10} molecule shown is truncated after the first isoprene unit.

4.3 Results

4.3.1 UQ Structure and Numbering.

UQ is a 2,3-dimethoxy,5-methyl, 6-isoprenoid benzoquinone. Fig. 4.1A shows the structure and International Union of Pure and Applied Chemistry (IUPAC) numbering for UQn. Fig. 4.1B shows a picture of UQ in the $_{QA}$ site with four of the surrounding amino acids. Fig. 4.1B was generated using the PDB ID code 1AIJ (20). Fig. 4.1B indicates that both UQ carbonyl (C═O) groups are H-bonded. The C_1═O is H-bonded to the backbone NH group of AlaM260. The C_4═O is H-bonded to one of the imidazole NH groups of HisM219. It is this H bond that FTIR data suggest is exceptionally strong. The other imidazole nitrogen atom of HisM219 provides a ligand to the nonheme iron atom and is 2.19 Å from the iron atom.

The starting model structure used in ONIOM calculations (derived from the PDB ID code1AIJ) includes UQ_1 and all atoms within 10 Å of both UQ carbonyl oxygen atoms. Geometry optimization of the starting structure using ONIOM methods leads to only very small modifications in bond lengths (<3.5%) and angles (see SI Text).

Fig. 4.2A (spectrum a) shows ONIOM calculated IR spectra for neutral unlabeled UQ_1 in the $_{QA}$ binding site. Throughout this manuscript the term “ONIOM calculated” will be used to refer to calculations for UQ_1 in which the surrounding protein atoms are included. Fig. 4.2B (spectrum a) shows DFTcalculated spectra for UQ_{1A} in the gas phase. The subscript “1A” refers to a UQ_1 conformation with C_2 and C_3 methoxy group dihedral angles of −8.9 and 123.6 ° (15). The C_2⁄C_3 dihedral angles are defined as the C_3-C_2-O-CH_3⁄C_2-C_3-O-CH_3 dihedral angles, respectively (see Fig. 4.1A for numbering). The UQ1A conformer was one of eight conformers studied previously (15) and is structurally the most similar to the UQ_1 optimized geometry

calculated using ONIOM methods, which has C_2 and C_3 dihedral angles of −25.3 and 150.5 °, respectively.

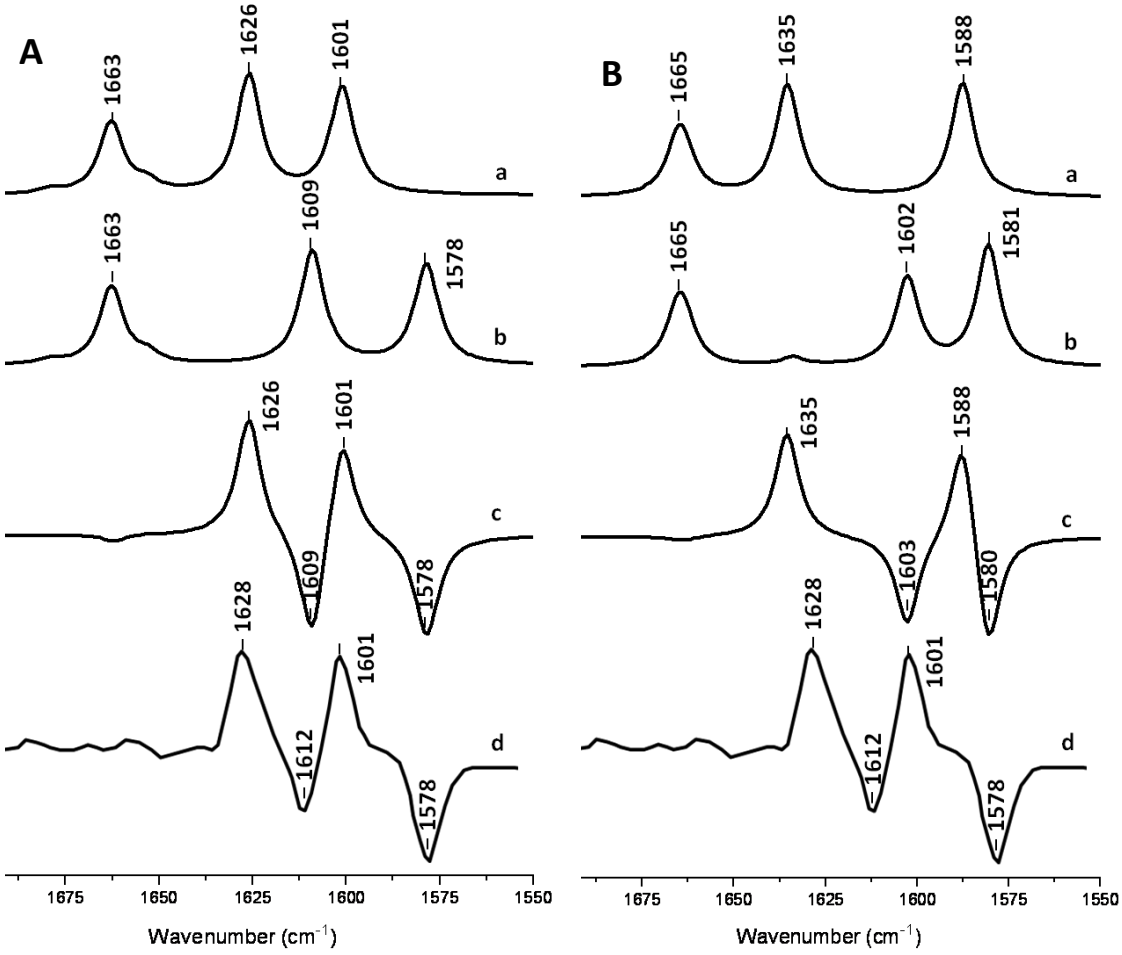

Figure 4.2: (A) Spectra of unlabeled (a) and $^{13}C_4$ labeled (b) UQ_1 calculated using ONIOM methods. (B) Spectra of unlabeled (a) and $^{13}C_4$ labeled (b) UQ_{1A} in the gas phase calculated using DFT methods. The spectra in (A)/(B) were scaled by 0.9718/0.9608, respectively. Spectrum c is the isotope edited spectrum obtained by subtracting spectrum b from a. Spectrum d is the corresponding experimental isotope edited FTIR DDS, taken from [15], with permission.

Also shown in Fig. 4.2 A and B are calculated IR spectra for neutral $^{13}C_4$ labeled UQ_1/UQ_{1A} (spectra labeled b), respectively. Subtracting spectrum b from spectrum a produces an

isotope edited IR double difference spectrum (DDS) that is shown as spectrum c in Fig. 4.2 A and B. For a detailed comparison between experimental and calculated spectra, Fig. 4.2 A and B shows the experimental $^{13}C_4$ isotope edited FTIR DDS obtained using PBRCs from Rb. sphaeroides (spectrum d). The ONIOM calculated and experimental IR DDS in Fig. 4.2A (spectra c and d) are very similar. This is not the case for the corresponding spectra calculated for UQ_{1A} in the gas phase. The ONIOM calculated spectra are clearly more in line with the experimental spectra.

From the ONIOM/gas phase calculated IR spectra in Fig. 4.2 A and B, neutral unlabeled UQ1 displays three prominent bands at 1663⁄1665, 1626⁄1635, and 1601⁄1588 cm^{-1}, respectively. Five vibrational modes contribute to these three bands. The frequencies, intensities, and potential energy distributions (PEDs) of these five modes are listed in Table 4.1. In the ONIOM calculations the 1679 and 1653 cm^{-1} vibrational modes have negligible intensity (Table 4.1) and will not be considered further. Although less clear-cut for gas phase calculations, the corresponding low intensity vibrations appear to be at 1663 and 1634 cm^{-1} (Table 4.1).

In the ONIOM calculated spectra the 1663 cm^{-1} band is due predominantly to the C_1═O stretching vibration (81%). The 1626 cm^{-1} band is due mainly to the C_4═O stretching vibration (68%). In the gas phase calculation for UQ1A the 1665 band contains contributions from both the in-phase and out-of-phase vibration of the C1═O group and the C═C group of the isoprene unit (labeled C═Ct in Table 4.1). The 1636 cm^{-1} band is due predominantly to the C_4═O group (79%).

Table 4.1: Normal mode frequencies (in cm^{-1}), intensities (in km/mol) and PED's calculated using ONIOM (*top*) and DFT (*bottom*) methods for unlabeled and $^{13}C_4$ labeled neutral UQ_1. $^{13}C_4$ isotope induced band-shifts are also listed. For the PED's the negative signs refer to the relative phase of the vibration of the internal coordinates. Only internal coordinates that contribute at least 6% to the normal modes are shown.

ONIOM Calculated Normal Modes						
ν (cm^{-1})	Intensity (km/mol)	Potential Energy Distribution	ν (cm^{-1}) $^{13}C_4$	Intensity (km/mol)	Potential Energy Distribution	$\Delta\nu$
1679	12	C=C tail (66%)	1679	11	$C=C_t$ (66%)	0
1663	185	C_1=O (81%)	1663	200	C_1=O (82%)	0
1653	26	$C_5=C_6$ (45%) $C_2=C_3$ (19%)	1653	23	$C_5=C_6$ (45%) $C_2=C_3$ (19%)	0
1626	305	C_4=O (68%) $-C_2=C_3$ (9%)	1579	258	C_4=O (71%) $C_2=C_3$ (6%)	47
1601	275	$C_2=C_3$ (35%) $-C_5=C_6$ (18%) C_4=O (14%) $-C_2-$O (6%)	1609	293	$C_2=C_3$ (38%) $-C_5=C_6$ (19%) C_2-O (10%) $-C_4$=O (9%)	-8
Gas Phase Calculated Normal Modes						
ν (cm^{-1})	Intensity (km/mol)	Potential Energy Distribution	ν (cm^{-1}) $^{13}C_4$	Intensity (km/mol)	Potential Energy Distribution	$\Delta\nu$
1665	129	C_1=O (46%) $C=C_t$ (31%)	1665	135	C_1=O (45%) $C=C_t$ (32%)	0
1663	65	C_1=O (40%) $-C=C_t$ (33%)	1663	70	C_1=O (41%) $-C=C_t$ (33%)	0
1634	37	$C_5=C_6$ (46%) $C_2=C_3$ (16%)	1634	22	$C_5=C_6$ (45%) $C_2=C_3$ (20%)	0
1636	255	C_4=O (79%)	1603	228	C_4=O (48%) $-C_2=C_3$ (16%) $C_5=C_6$ (11%) C_2-O (6%)	33
1588	293	$C_2=C_3$ (42%) $-C_5=C_6$ (20%) $-C_2-$O (9%)	1581	309	C_4=O (34%) $C_2=C_3$ (27%) $-C_5=C_6$ (11%)	7

In ONIOM calculations the relatively pure C_4=O mode (at 1626 cm^{-1}) downshifts 47 cm^{-1} upon $^{13}C_4$ labeling. The PED of the mode and its intensity are changed little by the labeling.

This is very different from that found in gas phase calculations, in which the relatively pure C_4═O mode (at 1636 cm^{-1}) downshifts only 33 cm^{-1} upon $^{13}C_4$ labeling with a considerable alteration in its mode composition (Table 4.1).

ONIOM calculations indicate that the lower frequency band at1601 cm^{-1} is due to an out-of-phase vibration of the C═C groups of the quinone ring (35% C_2═C_3 and 18% C_5═C_6) mixed somewhat with the stretching vibration of the C_4═O group (14%). The 1601 cm^{-1} mode is calculated to upshift 8 cm^{-1} upon $^{13}C_4$ labeling, with little change in mode composition or intensity. This upshift is unexpected and is caused by a change in the coupling of the C═C (C_2═C_3 and C_5═C_6) and C_4═O groups upon labeling. This coupling change arises because in the unlabeled case the C_4═O mode has a higher frequency than the C═C mode, whereas in the $^{13}C_4$ labeled case the C_4═O mode has a lower frequency than the C═C mode. Thus in the unlabeled/$^{13}C_4$ labeled species coupling of the C═C and C_4═O groups causes the resultant mode to downshift/upshift, respectively. The net effect is that the coupled mode upshifts upon labeling. The behavior of the 1601 cm^{-1} mode upon $^{13}C_4$ labeling is quite different from that found in gas phase calculations for the corresponding mode at 1588 cm^{-1}.

We have also used ONIOM methods to calculate the normal modes of neutral UQ_1 that has been isotope labeled in many different ways. From these calculated unlabeled and labeled spectra we have constructed IR DDS (in the same way as outlined in Fig. 4.2). The different ONIOM calculated isotope edited IR DDS for neutral UQ1 are presented in Fig. 4.3 A–F (spectra labeled a). The corresponding experimental isotope edited FTIR DDS (reproduced from a variety of sources) are also presented in Fig. 4.3 A–F (spectra labeled b) for comparison. The spectra in Fig. 4.3 A–F indicate a quite outstanding similarity between (ONIOM) calculated and experimental spectra.

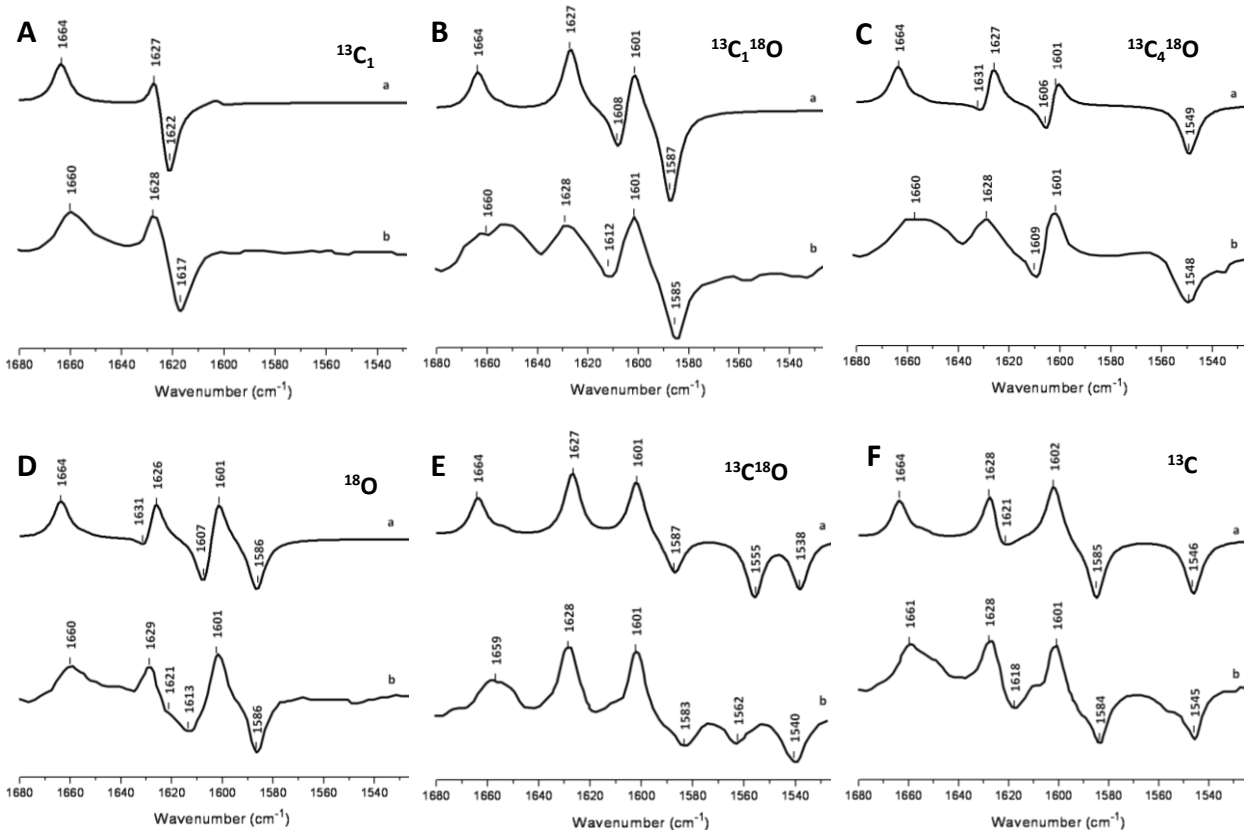

Figure 4.3: ONIOM calculated (a) and experimental (b) isotope edited DDS for neutral UQ in the $_{QA}$ binding site. UQ isotope labels are (A) $^{13}C_1$, (B) $^{13}C_1{}^{18}O$, (C) $^{13}C_4{}^{18}O$, (D) ^{18}O, (E) $^{13}C^{18}O$, (F) ^{13}C. For ^{18}O labeling only the carbonyl oxygen atoms (and not the methoxy group oxygen atoms) are labeled. Experimental spectra in panels (A), (B), (C) were taken from [15] with permission. Experimental Spectra in panels (D), (E), (F) were taken from [16] with permission. Calculated spectra were scaled by 0.9718.

Isotope edited IR DDS were also calculated for all of the differently labeled UQ1A molecules in the gas phase, and these spectra are presented in the SI Text, where they are also compared to the corresponding experimental spectra. As was evident in Fig. 4.2, the calculated gas phase spectra poorly model the experimental spectra, compared to the ONIOM calculated spectra. Given this, the calculated gas phase spectra will not be considered further in this manuscript.

Table 4.2: ONIOM calculated frequencies, intensities and PEDs for the three most intense vibrational modes of unlabeled and variously labeled UQ_1 in the Q_A binding site. The row labels refer the relevant panels in Figure 4.3 (or Figure 4.2).

	Isotope Label	ν (cm^{-1})	Intensity	$\Delta\nu$	Potential Energy Distribution
Fig. 2A	$^{12}C^{16}O$	1663	185		C_1=O (81%)
Fig. 2A	$^{13}C_4$	1663	200	0	C_1=O (82%)
A	$^{13}C_1$	1621	412	42	C_1=O (63%), -C_4=O (19%)
B	$^{13}C_1{}^{18}O$	1587	287	76	C_1=O (78%)
C	$^{13}C_4{}^{18}O$	1629	195	34	C_1=O (82%)
D	^{18}O	1629	187	34	C_1=O (82%)
E	$^{13}C^{18}O$	1587	172	76	C_1=O (81%)
F	^{13}C	1623	155	40	C_1=O (65%), -C=C_t (16%)
Fig. 2A	$^{12}C^{16}O$	1626	305		C_4=O (68%), -C_2=C_3 (9%)
Fig. 2A	$^{13}C_4$	1579	258	47	C_4=O (71%), C_2=C_3 (6%)
A	$^{13}C_1$	1628	85	-2	C_4=O (50%), C_1=O (20%), -C_2=C_3 (8%)
B	$^{13}C_1{}^{18}O$	1586	175	40	C_4=O (61%), C_2=C_3 (8%), -C_5=C_6 (7%)
C	$^{13}C_4{}^{18}O$	1549	231	77	C_4=O (77%)
D	^{18}O	1586	249	40	C_4=O (65%), C_2=C_3 (7%), -C_5=C_6 (6%)
E	$^{13}C^{18}O$	1558	289	68	C_4=O (42%), -C_2=C_3 (21%), C_2-O (8%), C_5=C_6 (7%)
F	^{13}C	1584	287	42	C_4=O (76%)
Figure 2	$^{12}C^{16}O$	1601	275		C_2= C_3 (35%), -C_5= C_6 (18%), C_4= O (14%), -C_2-O (6%)
Figure 2	$^{13}C_4$	1609	293	-8	C_2= C_3 (38%), -C_5= C_6 (19%), C_2-O (10%), -C_4= O (9%)
A	$^{13}C_1$	1601	260	0	C_2= C_3 (35%), -C_5= C_6 (18%), C_4= O (14%), -C_2-O (6%)
B	$^{13}C_1{}^{18}O$	1610	265	-9	C_2= C_3 (38%), -C_5= C_6 (15%), -C_4= O (13%), -C_2-O (10%)
C	$^{13}C_4{}^{18}O$	1607	296	-6	C_2= C_3 (42%), -C_5= C_6 (20%), C_2-O (10%)
D	^{18}O	1609	308	-8	C_2= C_3 (37%), -C_5= C_6 (15%), -C_4= O (13%), -C_2-O (10%)
E	$^{13}C^{18}O$	1539	233	62	C_4= O (37%), C_2= C_3 (20%), -C_5= C_6 (13%)
F	^{13}C	1545	256	56	C_2= C_3 (38%), -C_5= C_6 (19%), -C_2-O (8%), C_4= O (6%)

In ONIOM calculations, in the spectral region considered, only the three high intensity modes need to be considered (Table 4.1). The frequencies, intensities, and PEDs for these three

modes, for different types of isotope labeled UQ_1, are listed in Table 4.2. The frequency shifts that occur upon labeling are also listed in Table 4.2.

4.3.1. ^{18}O Labeling. Upon ^{18}O labeling of UQ_1 the ONIOM calculated data indicates that the 1663/1626 cm^{-1} mode downshifts 34/40 cm^{-1} to 1629/1586 cm^{-1}, respectively, without much change in the mode composition (Table 2). The C═C/C_4═O mode at 1601 cm^{-1} upshifts 8 cm^{-1} upon ^{18}O labeling (Table 4.2).It is easy to see how these ^{18}O induced shifts give rise to the features in the DDS shown in Fig. 4.3D (spectrum a). The calculated ^{18}O induced band shifts differ from previous interpretations based on experimental FTIR DDS. The accepted interpretation for the bands in the isotope edited DDS in Fig. 4.3D (spectrum b) is that the 1660, 1,629 and 1601 cm^{-1} bands downshift to 1625, 1613, and 1586 cm^{-1}, respectively (table 1 in ref. 21).

4.3.2. ^{13}C Labeling. Upon global ^{13}C labeling of UQ_1 the ONIOM calculated data indicate that the 1663/1626/1601 cm^{-1} modes downshift 40/42/56 cm^{-1} to 1623/1584/1545 cm^{-1}, respectively (Table 4.2). Again, these ^{13}C induced shifts are easily visualized in the DDS shown in Fig. 4.3F. The bands in the experimental ^{13}C FTIR DDS are interpreted to shift similarly (21). The observation that the 1601 cm^{-1} band downshifts 56 cm^{-1} upon ^{13}C labeling is a strong indication that it is due to a predominantly C═C mode.

4.3.3. $^{13}C_1$ Labeling. For unlabeled UQ_1 the 1663 cm^{-1} mode is due mainly to a C_1═O stretching vibration (81%). Upon $^{13}C_1$ labeling the C_1═O vibration is expected to downshift approximately 40 cm^{-1} (to approximately 1623 cm^{-1}). This lower frequency is close to the vibrational frequency of the mode associated with the out-of-phase vibration of the C_4═O and C_2═C_3 groups (approximately 1626 cm^{-1}). This similarity in frequency will result in mixing of the two modes upon $^{13}C_1$ labeling. Indeed, upon $^{13}C_1$ labeling the 1663 cm^{-1} C_1═O mode downshifts to 1621

cm^{-1} and increases in intensity by 122% (Table 4.2). The 1621 cm^{-1} mode in the $^{13}C_1$ labeled species is now due to the out-of-phase vibrations of the C_1═O and C_4═O groups (Table 4.2). The 1626 cm^{-1} mode [C_4═O (68%), C2═C3 (9%)] upshifts 2 cm^{-1} upon $^{13}C_1$ labeling and decreases in intensity by 72%. It is this intensity decrease that gives rise to the positive feature at 1627 cm^{-1} in the calculated DDS in Fig. 4.3A. This is different from the experimental interpretation in which it is hypothesized that the 1628 cm^{-1} band (due to a C═C mode) downshifts to 1617 cm^{-1} (12).

The 1601 cm^{-1} mode is essentially unaffected by $^{13}C_1$ labeling and does not show up in the calculated or experimental DDS.

4.3.4. $^{13}C_1{}^{18}O$ Labeling. Upon $^{13}C_1{}^{18}O$ labeling the 1626 cm^{-1} mode of unlabeled UQ_1 downshifts 41 cm^{-1} to 1586 cm^{-1}. This large downshift leads to a clear and intense positive band at 1626 cm^{-1} in the DDS (Fig. 3B). Upon $^{13}C_1{}^{18}O$ labeling, the C_1═O stretching mode at 1663 cm^{-1} downshifts 76 cm^{-1} to 1587 cm^{-1} without much change in mode composition. Thus two modes overlap near 1587 cm^{-1} giving rise to an intense negative band at 1587 cm^{-1} in the calculated DDS in Fig. 4.3B. The 1601 cm^{-1} mode of unlabeled UQ_1 upshifts 9 cm^{-1} upon $^{13}C_1{}^{18}O$ labeling, similar to that found upon 18O labeling.

4.3.5. $^{13}C_4{}^{18}O$ Labeling. Upon $^{13}C_4{}^{18}O$ labeling, the 1663 cm^{-1} (C_1═O) mode downshifts to 1629 cm^{-1}, as it also does for ^{18}O labeling. The 1626 cm^{-1} mode downshifts 77 cm^{-1} to 1549 cm^{-1}. The 1549 cm^{-1} mode in the labeled species is an almost pure C_4═O mode (77%). The 1601 cm^{-1} mode upshifts 6 cm^{-1} upon $^{13}C_4{}^{18}O$ labeling and increases in intensity.

4.3.6. $^{13}C^{18}O$ Labeling. The isotope induced downshift in frequencies of the modes of UQ_1 upon $^{13}C^{18}O$ labeling are sufficiently large (64–77 cm^{-1}) to allow all of the bands of unlabeled UQ_1 to

be clearly distinguished, without overlapping contributions from other modes of the labeled species. The calculated and experimental spectra above 1600 cm^{-1} in Fig. 4.3E thus represent an almost pure absorption spectrum of neutral UQ in the Q_A binding site.

4.4 Discussion

Previously we have calculated IR spectra for unlabeled and labeled neutral UQ_1 in the gas phase and in solvent (CCl_4). The calculation is complicated by the fact that at least eight UQ_1 methoxy group conformers (each with different IR spectra) contribute to the overall spectrum at room temperature (15). The situation discussed here for ONIOM calculations is simpler because fewer UQ conformers are calculated to be present in the Q_A binding site. We have used ONIOM methods to geometry optimize all eight UQ methoxy group conformers (studied previously) in the $_{QA}$ binding site. Three of these conformations cannot be optimized (upon optimization the UQ leaves the binding site), and the remaining five optimize to one of two possible UQ conformers. Both of these conformations lead to calculated isotope edited DDS that are similar to experimental spectra. The two possible conformers are UQ_{1A} and UQ_{1B}. UQ_{1A} and UQ_{1B} differ in that the C_3 methoxy dihedral is approximately reflected in the quinone ring plane (15). Given that the crystal structure suggests a UQ_{1A} model is appropriate for the Q_A binding site, and that the calculated spectra for UQ_{1A} and UQ_{1B} are similar, we consider spectra only for UQ_{1A} in the Q_A binding site. There is a suggestion of some substructure to the 1660 cm^{-1} band in the experimental FTIR DDS [Fig. 3 A–F(b)]. This substructure may be an indication that more than one UQ conformation (with IR bands slightly shifted in frequency) is present in the $_{QA}$ binding site.

Conclusions originally derived from the experimental isotope edited DDS (12, 13) are (i) the C1═O vibration of unlabeled UQ occurs at 1660 cm^{-1}, (ii) the C_4═O vibration occurs at

1601 cm^{-1} and (iii) the 1628 cm^{-1} band is due to C═C ring vibration. These conclusions are at odds with our ONIOM calculations, which suggest that the 1660 and 1628 cm^{-1} bands are due to C_1═O and C_4═O vibrations, respectively, whereas the 1601 cm^{-1} band is due predominantly to a C═C ring vibration (Table 4.2).

The interpretation of bands in experimental spectra arose mainly from a consideration of $^{13}C_1$ and $^{13}C_4$ isotope edited DDS. The experimental $^{13}C_1$ isotope edited DDS (Fig. 4.3A, spectrum b) displays two positive bands at 1660 and 1628 cm^{-1}, and a negative band at 1617 cm^{-1}. The experimental $^{13}C_4$ isotope edited DDS (Fig. 4.2A, spectrum d) displays two positive bands at 1,628 and 1601 cm^{-1}, and two negative bands at 1,612 and 1578 cm^{-1}. The conclusions from these spectra are that (i) the 1660 cm^{-1} band downshifts approximately 43 cm^{-1} to 1617 cm^{-1} upon $^{13}C_1$ labeling, (ii) the 1601 cm^{-1} band downshifts approximately 23 cm^{-1} to 1578 cm^{-1} upon $^{13}C_4$ labeling, (iii) the 1628 cm^{-1} band downshifts approximately 11⁄16 cm^{-1} to 1617⁄1612 cm^{-1} upon $^{13}C_1$⁄$^{13}C_4$ labeling, respectively. An alternative possibility, which was not considered, is that the 1628 cm^{-1} band in the $^{13}C_4$ isotope edited DDS downshifts 50 cm^{-1} to 1578 cm^{-1}. This hypothesis was probably rejected because it implies that the 1601 cm^{-1} band must upshift to 1612 cm^{-1} upon $^{13}C_4$ labeling. Such a conclusion may seem counterintuitive without additional supporting evidence.

Nonella and coworkers (19) have used a DFT based QM:MM method to calculate vibrational frequencies of a tailless UQ (UQ0) occupying the $_{QA}$ and $_{QB}$ binding sites in PBRCs from Rb. sphaeroides. Normal mode vibrational frequencies were considered in this work, but mode intensities were not. This is unfortunate as this lack of consideration led them to wrongly correlate calculated modes with experimental bands. For example, in ref. 19

the UQ C_5═C_6 mode frequency is calculated to lie between the two C═O modes, and it is claimed that it is this C_5═C_6 mode that gives rise to the 1628 cm^{-1} band in the experimental spectrum. Furthermore, the C_2═C_3 vibration is calculated to lie more than 30 cm^{-1} lower in frequency than the UQ C_4═O mode, but this mode is not considered (19).

We showed above (Table 4.2) that the C_5═C_6 mode (at 1653 cm^{-1}) has a frequency that does lie between the two C═O modes. However, this C═C mode has negligible intensity and could not give rise to the 1628 cm^{-1} band in the experimental spectrum. We also showed that the lower frequency C_2═C_3 mode is very intense, and it is this mode that must give rise to the 1601 cm^{-1} band in the experimental spectrum. The C_4═O mode cannot give rise to the 1601 cm^{-1} band in the experimental spectrum.

The C_4═O group is suggested to be very strongly H-bonded based only on the assignment of a FTIR band at 1601 cm^{-1} to the C_4═O vibration (12, 13). Our calculations very clearly show that it is the 1628 cm^{-1} band that is associated with the C_4═O vibration. The C_4═O group is therefore not very strongly H-bonded. This conclusion is in fact supported by results from other experiments:

First, the crystal structure suggests that the C_1═O/C_4═O group is H-bonded to the peptide nitrogen of AlaM260/imidazole nitrogen of HisM219, respectively. The distance to the H-bonding nitrogen atoms of AlaM260 or HisM219 to the respective C═O groups is similar, so similar H-bond strengths might be expected. On the other hand, because the second imidazole nitrogen atom of HisM219 ligates with the non-heme iron atom (Fig. 4.1B), it was suggested that this doubly bonded imidazole may lead to a very strong H bond to the C_4═O group. Upon consideration of possible mechanisms, however, it was concluded that this uniquely bound imidazole will not lead to strong H bonding (6).

Second, the vibrational frequency associated with the C4═O group of Q_A (1601 cm^{-1}) appears unaffected by incubation of PBRCs in D_2O (14). Although solvent exchange experiments are not entirely free from ambiguity, this result also suggests that the C_4═O group is not strongly H bonded.

Third, labeled and unlabeled versions of chainless symmetrical naphthoquinones, benzoquinones, and ubiquinones have been incorporated into the Q_A binding site in Rb. sphaeroides PBRCs, and these RCs have been studied using FTIR DS (22). These studies indicated no strong H bond to the C_4═O group of the incorporated quinones. These studies therefore do not support the idea of strong H bonding to the C_4═O group of native UQ in the Q_A binding site.

If the C_4═O group of Q_A absorbs at 1628 cm^{-1} and not 1601 cm^{-1}, then there is no need to suggest that the C_4═O group is very strongly H bonded. The C_4═O mode of UQ in the Q_A site is still downshifted approximately 22 cm^{-1} compared to that found for UQ in solution (1628 cm^{-1} instead of 1650 cm^{-1}). This may suggest that the C_4═O mode of UQ in the Q_A site is still H bonded, albeit less strongly. The C_4═O mode downshift of 22 cm^{-1} is probably not all due to H bonding. Our calculations suggest that the electrostatic environment around UQ in the Q_A site gives rise to an approximately 8 cm^{-1} separation of the C_1═O and C_4═O modes (in ONIOM calculations the difference in frequency between the C_1═O and C_4═O modes is 37 cm^{-1}, compared to 29 cm^{-1} in gas phase calculations). From this perspective, the downshift of frequency due to H bonding of the C_4═O group may be only approximately 14 cm^{-1} instead of 22 cm^{-1}. The H bond to the C_4═O group may therefore not be considerably stronger than the H bond to the C_1═O group provided by AlaM260. This hypothesis is in line with predictions based on the X-ray crystal structural data (Fig. 4.1B).

The picture emerging from the calculated and experimental FTIR data (for UQ in solution and in the Q_A binding site) concerning the factors governing the asymmetry in the environment of UQ in the Q_A site, is that the orientation of the methoxy groups, weakly asymmetric H bonding to the C═O groups, and the electrostatic environment around the UQ, all contribute roughly equally and additively in the sense that all three mechanisms lead to increasing the separation of the vibrational frequencies of the C_1═O and C_4═O modes.

Recently, a mutant reaction center has been made in which the alanine residue at M260 has been changed to cysteine (23). Q_A^-/Q_A FTIR DS obtained using this mutant show that the 1601 cm^{-1} band has disappeared. However, the mutant RC functions similarly to wild type. It is concluded that the unusually strong H bond between the carbonyl of Q_A and His M219 is not required for efficient electron transfer from Q_A^- to Q_B. This conclusion of course needs to be reconsidered in the light of the FTIR band assignments presented here. At present we are undertaking calculations aimed at modeling Q_A^-/Q_A FTIR DS for this mutant RC.

In conclusion, we have shown that ONIOM type QM:MM calculations can be used to model (extremely well) experimental isotope edited Q_A^-/Q_A FTIR difference spectra. Our ONIOM calculations point to an interpretation of experimental FTIR DS that is more in line with results from several other types of experiments. In this way we were able to resolve a long-standing and perplexing problem related to H bonding of the UQ occupying the Q_A binding site in PBRCs. Although we have focused on the neutral state of UQ that occupies the Q_A binding site in PBRCs, the procedures developed and outlined in this manuscript are sufficiently general to be applicable to not only other quinone-containing photosynthetic and respiratory proteins, but

also to other types of cofactors in a wide range of proteins. In this manuscript we show that an era of FTIR DS is emerging in which spectral band interpretation is based upon computational simulation in combination with physical intuition.

ONIOM-type calculations aimed at modeling EPR data associated with cofactor radicals in protein complexes are being developed (24). In the near future computational studies will be undertaken in which both the EPR and FTIR data are simulated using the same ONIOM optimized structural model. Such an approach involving the simulation of different types of data will provide a very stringent test of the appropriateness of the ONIOM computational method in the various areas of application.

4.5 Materials and Methods

4.5.1 Model Construction

All molecular models were constructed using the crystal structure of Rb. sphaeroides PBRCs at 2.2 Å resolution (20) (PDB ID code 1AIJ). The ONIOM model includes all amino acid atoms within 10 Å of either carbonyl oxygen atom of UQ. The UQ tail is truncated after the first isoprene unit. This is reasonable because Q_A^-/Q_A FTIR DS obtained using PBRCs with UQ_1, UQ_3, UQ_6, and UQ_{10} incorporated into the Q_A site are all identical (12, 13, 21). The model used in ONIOM calculations contains UQ, one iron atom, seven water molecules, and 49 amino acids. The amino acids included are listed in SI Text.

4.5.2 Calculations. For geometry optimization using ONIOM methods all atoms associated with the protein backbone are held fixed. All atoms of the amino acid side chains and UQ are unconstrained. For calculation of UQ molecules in the gas phase, and for the QM part of

ONIOM calculations, molecular geometry optimizations and harmonic vibrational frequency calculations were undertaken using hybrid DFT methods, employing the B3LYP functional and the 6-31+G(d) method within Gaussian 03 (25). The MM part of the ONIOM calculation is undertaken using AMBER (18). Following ONIOM geometry optimization of the protein–quinone system, the optimized UQ1 molecule is considered separately for vibrational frequency analysis. Calculated normal mode vibrational frequencies presented here are scaled by 0.9608 (gas phase) and 0.9718 (ONIOM). Such scaling factors are standard (26).

4.5.3 Normal Mode Assessment. Assignment of calculated vibrational frequencies to molecular groups is based on a consideration of the calculated atomic displacements (in Cartesian coordinates) associated with the normal modes. These atomic displacements can be animated using software (GaussView03), and the molecular groups that most prominently contribute to the normal modes can be assessed visually. In addition, PEDs of the normal modes are calculated using the freeware GAR2PED (27). PEDs allow an assessment of the contribution of different internal coordinates to the normal modes. The GAR2PED program first generates a set of nonredundant internal coordinates for the molecule of interest, and then the percentage contribution of these internal coordinates to the total energy of each normal mode is calculated.

In our work all normal mode frequencies and intensities are calculated. With both the frequency and intensity information IR stick spectra can be constructed. By convolving these stick spectra with a Gaussian function (4 cm^{-1} half-width) more realistic-looking spectra are constructed. We refer to these convolved stick spectra as absorption spectra.

4.6 Supplementary Information

4.6.1 Supplementary Information Section 1

Figure 4.6.S1 shows DFT calculated (a) and experimental (b) isotope edited DDS. DFT calculations are for UQ_{1A} in the gas phase. Experimental spectra are for UQ in the $_{QA}$ binding site in PBRCs from *Rb. sphaeroides*. In panels (B), (D)-(F), the calculated spectra deviate considerably from the experimental spectra.

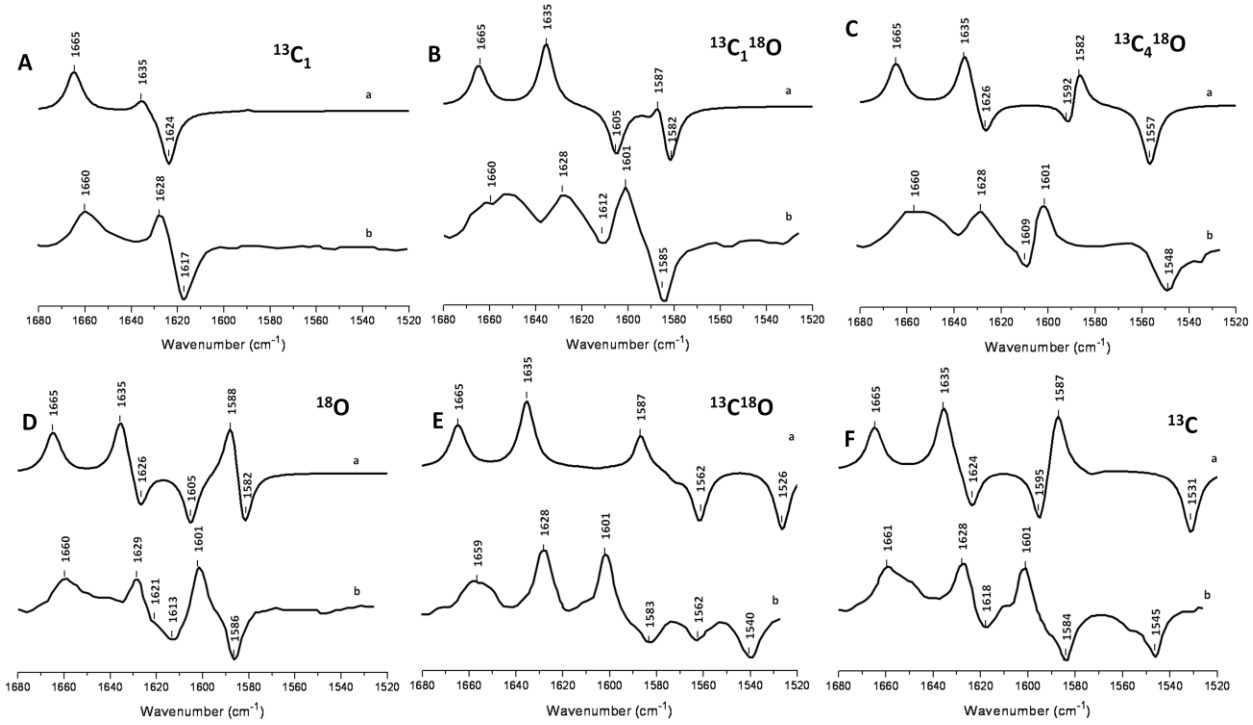

Figure 4.S1: DFT calculated (a) and experimental (b) isotope edited DDS. DFT calculations are for neutral UQ_{1A} in the gas phase. Experimental spectra are for UQ in the $_{QA}$ binding site. UQ isotope labels are (A) $^{13}C_1$, (B) $^{13}C_1{}^{18}O$, (C) $^{13}C_4{}^{18}O$, (D) ^{18}O, (E) $^{13}C^{18}O$, (F) ^{13}C. For ^{18}O labeling only the carbonyl oxygen atoms (and not the methoxy group oxygen atoms) are labeled. Experimental DDS in panels (A), (B) and (C) were taken from[15], with permission. Experimental Spectra in panels (D), (E), (F) were taken from[16], with permission. Calculated normal mode frequencies were scaled by 0.9608.

Table 4.S1. Comparison of bond lengths and angles derived from the crystal structure and the ONIOM calculated optimized geometry of neutral UQ in the Q_A binding site

UQ_1 Parameters	Crystal Structure	Optimized Structure
C_1=O	1.2337	1.2272
C_4=O	1.2320	1.2379
C_2=C_3	1.4041	1.3659
C_5=C_6	1.4191	1.3544
C_4=O-- H-bond	2.788	2.868
C_1=O-- H-bond	2.837	2.837
C_4=O - Fe	6.832	6.7415
C_2-dihedryl	-57.1	-25.3
C_3-dihedryl	109.5	150.5

Distances are in angstroms and angles are in degrees. The C_2/C_3 dihedral angles are defined as the C_3-C_2-O-CH_3/C_2-C_3-O-CH_3 dihedral angles, respectively (see Fig. 4.1A for numbering).

Table 4.S2 DFT calculated frequencies, intensities, and PEDs for the three most intense vibrational modes of unlabeled and variously labeled UQ_{1A} in the gas phase Isotope label ν, cm^{-1} Intensity, km/mol $\Delta\nu$, cm^{-1} Potential energy distribution

	Isotope Label	ν (cm^{-1})	Intensity	Δν	Potential Energy Distribution
Fig. 2B	$^{12}C^{16}O$	1665	129		C_1=O (46%), -C=C_t (31%)
Fig. 2B	$^{13}C_4$	1665	135	0	C_1=O (45%), -C=C_t (32%)
A	$^{13}C_1$	1624	242	41	C_1=O (82%)
B	$^{13}C_1{}^{18}O$	1589	244	76	C_1=O (82%)
C	$^{13}C_4{}^{18}O$	1627	160	38	C_1=O (63%), -C_5=C_6 (16%), -C_2=C_3 (7%)
D	^{18}O	1627	176	38	C_1=O (63%), -C_5=C_6 (15%), -C_2=C_3 (6%)
E	$^{13}C^{18}O$	1589	156	76	C_1=O (80%)
F	^{13}C	1624	180	41	C_1=O (86%)
Fig. 2B	$^{12}C^{16}O$	1636	255		C_4=O (79%)
Fig. 2B	$^{13}C_4$	1603	228	33	C_4=O (48%), - C_2=C_3 (6%), C_5=C_6 (11%), C_2=O (6%)

A	$^{13}C_1$	1636	188	0	C_4=O (79%)
B	$^{13}C_1{}^{18}O$	1607	208	29	C_4=O (60%), -C_2=C_3 (15%), C_5=C_6 (5%)
C	$^{13}C_4{}^{18}O$	1557	254	79	C_4=O (73%)
D	^{18}O	1607	231	29	C_4=O (64%), -C_2=C_3 (14%), C_5=C_6 (5%)
E	$^{13}C^{18}O$	1563	232	73	C_4=O (74%), -C_2=C_3 (6%)
F	^{13}C	1595	263	41	C_4=O (82%)
Fig. 2B	$^{12}C^{16}O$	1588	293		C_2= C_3 (42%), -C_5= C_6 (20%) -C_2-O (9%)
Fig. 2B	$^{13}C_4$	1581	309	7	C_4= O (34%)C_2= C_3 (27%), -C_5= C_6 (11%)
A	$^{13}C_1$	1588	288	0	C_2= C_3 (42%), -C_5= C_6 (20%), -C_2-O (9%)
B	$^{13}C_1{}^{18}O$	1584	253	4	C_2= C_3 (30%), C_4= O (20%), -C_5= C_6 (17%), -C_2-O (6%)
C	$^{13}C_4{}^{18}O$	1593	258	-5	C_2= C_3 (40%), -C_5= C_6 (19%), -C_2-O (11%), -C_4= O (7%)
D	^{18}O	1584	297	4	C_2= C_3 (31%), C_4= O (22%), -C_5= C_6 (17%), -C_2-O (6%)
E	$^{13}C^{18}O$	1529	270	59	C_2= C_3 (36%), -C_5= C_6 (19%), C_4= O (9%), -C_2-O (8%)
F	^{13}C	1531	266	57	C_2= C_3 (40%), -C_5= C_6 (19%), -C_2-O (10%)

The row labels refer the relevant panels in Fig. 4.S1 (or Fig. 4.2 of the main text).

CHAPTER 5
CALCULATED VIBRATIONAL PROPERTIES OF UBIQUINONE RADICAL ANIONS IN PROTEIN BINDING SITES

5.1 Abstract

ONIOM type QM:MM calculations have been undertaken in an attempt to gain a detailed understanding of the vibrational properties of the ubiquinone radical anion in the Q_A binding site in purple bacterial reaction centers from *Rhodobacter sphaeroides*. In particular we focus on simulating parts of the (Q_A^- -Q_A) isotope edited FTIR double difference spectra that are associated with the ubiquinone radical anion. We show that the ONIOM calculated spectra are in remarkable agreement with experimental spectra. The ONIOM calculated spectra allow a new and more detailed interpretation of the experimental spectra compared to what has been proposed previously: The IR spectrum of ubisemiquinone in the gas phase (or solvent) displays a single intense carbonyl absorption band. This band splits into three separate bands at ~1480, 1467 and 1451 cm^{-1} for ubisemiquinone in the Q_A binding site. The 1480 and 1467 cm^{-1} bands are due to primarily C_1=O and C_4=O stretching vibrations (coupled to C-H methyl bending vibrations), respectively. The 1451 cm^{-1} band is due to a coupled vibration of both carbonyl groups.

The ONIOM calculations indicate that the C_4=O group of ubisemiquinone is not strongly hydrogen bonded. They also indicate an asymmetric interaction of the carbonyl groups with the protein.

5.2 Introduction

Structure and properties of ubiquinone (UQn: 2,3-dimethoxy-5-methyl-6-polyprenyl-1,4-benzoquinone, see Fig. 1 for structure and numbering) molecule depend on type of solvent or protein binding site [14-16, 44, 50, 51]. In particular the same ubiquinone molecule in the purple bacteria reaction centers (PBRCs) has very different functions at Q_A and Q_B binding sites. Q_A is an intermediary cofactor involved in transferring electrons from bacteriopheophytin to Q_B, while Q_B couples electron and proton transfer processes [22, 23].

Prior to ~2000, several groups had undertaken computational work aimed at modeling the physical and chemical properties of UQ and UQ^{-} [27-31, 52]. The work that has been undertaken is limited in one way or another, for example tail-less quinone models in only the gas phase were considered, using relatively low-levels of theory. To address this problem we embarked on a systematic study of the vibrational properties of UQ and UQ^{-} both in solution and in PBRCs.

One feature of Q^{-}/Q IR difference spectra (in both solution and in protein binding sites) is that the [C=O and C=C] bands of the neutral state are well separated (>100 cm^{-1}) from bands associated with the anion radical. Computationally, this means that the vibrational properties of neutral quinones can be studied separately from semiquinones. Previously we have used DFT based methods to study the vibrational properties of neutral UQs in the gas phase and in solution[50]. In this study the goal was to simulate the many available experimental FTIR spectra associated with unlabeled and isotope labeled neutral UQs in solution. Although the calculations were complicated by the fact that at least eight different UQ methoxy group conformations could exist in solution at room temperature (RT), it was shown that calculated and experimental spectra were in good agreement. Given this agreement a new, detailed

interpretation of the experimental spectra could be developed. Following on from this work we used ONIOM type QM:MM methods to study the vibrational properties of neutral UQ in the Q_A binding site in PBRCs[53]. Study of the Q_A binding site was a natural choice given that experimental FTIR difference spectra are available for various types of quinones (both labeled and unlabeled) occupying the Q_A binding site in PBRCs. In the above study, and in a second follow up study (see chapter 6), we showed that the ONIOM approach could be used to calculate isotope edited FTIR difference spectra associated with neutral UQ in the Q_A binding site that were in remarkable agreement with the many available experimental spectra.

Recently we have used DFT based methods to calculate the vibrational properties of ubisemiquinones in the gas phase and in solution (see chapter 3). The normal modes of UQ^- are considerably more complex (due to mode mixing) than that found for the neutral state. Nonetheless the calculated normal modes frequencies, and how they shift upon labeling, were found to be in good agreement with experimental IR and Raman spectra of ubisemiquinones.

In the studies of UQ^- in solution we noted that the calculated spectra could not simulate the spectra associated with UQ^- in the Q_A binding site. Calculations including the protein environment were required.

Here we describe how we have used ONIOM type QM:MM calculations in order to model isotope edited FTIR difference spectra associated with the ubiquinone anion radical in the Q_A protein binding site in PBRCs from *Rb. sphaeroides*. In order to include Van der Waals, electronic and hydrogen bonding effect of protein binding site on QA, we have used AMBER force field at low level calculation in the ONIOM method.

5.3. Materials and methods

5.3.1 Model Construction.

All molecular models were constructed using the crystal structure of *Rb. sphaeroides* PBRCs at 2.2 Å resolution (PDB file 1AIJ) [6]. The ONIOM model includes all amino acid atoms within 10 Å of either carbonyl oxygen atom of UQ. The UQ tail is truncated after the first isoprene unit. This is reasonable since QA^{-}/QA FTIR DS obtained using PBRCs with UQ1, UQ3, UQ6 and UQ10 incorporated into the QA site are all identical [14-17]. The model used in ONIOM calculations contains UQ, one iron atom, seven water molecules and 49 amino acids. Hydrogen atoms were added to the model using GaussView version 05.

5.3.2 Calculations.

For geometry optimization using ONIOM methods all atoms associated with the protein backbone were held fixed. All atoms of the amino acid side chains and UQ^{-} are unconstrained. For calculation of UQ^{-} molecules in the gas phase, and for the QM part of ONIOM calculations, molecular geometry optimizations and harmonic vibrational frequency calculations were undertaken using hybrid DFT methods, employing the B3LYP functional and the 6-31+G(d) method within Gaussian 03 [48]. This choice of functional and basis set has been shown to appropriate for calculation of the vibrational properties of semiquinones[37, 40, 53]. The MM part of the ONIOM calculation is undertaken using the AMBER (Assisted Model Building with Energy Refinement) molecular dynamics package [54, 55]. The AMBER charges and parameters for UQ^{-} were calculated using the antechamber program. The non-heme iron atom was treated as a doubly ionized fixed atom. Following ONIOM geometry optimization of

the protein-quinone system, the optimized UQ_1^- molecule is considered separately for vibrational frequency analysis. Calculated normal mode vibrational frequencies presented here are scaled by 0.9771. This scale factor was calculated from the correlation of calculated anion UQ frequencies and the experimental FTIR double difference band frequencies [14, 15]. Such a scaling factor is standard [18].

5.3.3 Normal Mode Assessment.

Assignment of calculated vibrational frequencies to molecular groups is based on a consideration of the calculated atomic displacements (in Cartesian coordinates) associated with the normal modes. These atomic displacements can be animated using software (in our case we used GaussView version 5), and the molecular groups that most prominently contribute to the normal modes can be assessed visually. In addition, potential energy distributions (PEDs) of the normal modes are calculated using the freeware GAR2PED [49]. PEDs allow an assessment of the contribution of different internal coordinates to the normal modes. The GAR2PED program first generates a set of non-redundant internal coordinates for the molecule of interest, and then the percentage contribution of these internal coordinates to the total energy of each normal mode is calculated. In our work all normal mode frequencies and intensities are calculated. With both the frequency and intensity information IR stick spectra can be constructed. By convolving these stick spectra with a Gaussian function (4 cm^{-1} half-width) more realistic-looking spectra are constructed. We refer to these convolved stick spectra as absorption spectra.

5.4. Results

5.4.1 UQ_1 structure and numbering

Fig. 5.1A shows the atom numbering scheme we have used in this manuscript for UQ_1. The atom type is also specified. As described previously (see chapter 3) we consider UQ with

only a single isoprene unit. Consideration of UQ models with more than one isoprene unit gives similar results. Figure 5.1A also shows some of the internal coordinates that are used in this manuscript to describe the calculated potential energy distributions of the normal modes. Of particular interest in this work are the internal coordinates involving stretching of the C=O (R3 and R9) and C=C (R4 and R10) bonds.

5.4.2 Calculated structure of the ubiquinone radical anion (ubisemiquinone or UQ_1^-)

Previously, from calculations of UQ_1^- in the gas phase and in solvent (CCl_4) we find that UQ_1^- can adopt four different conformers that differ in the orientation of the C_2 and C_3 methoxy groups (see chapter 3). The conformers were labeled A, B, E and F. In ONIOM calculations we have attempted to geometry optimize models of the Q_A binding site in which all four UQ_1^- conformers were initially incorporated. Conformer B in the Q_A site could not be optimized, and the other three conformers all converged to a conformer A type structure. This is interesting because conformer A in solution or the gas phase is high in energy compared to conformer E or F. Figure 5.1B show the ONIOM calculated geometry optimized structure of UQ_1^- in the Q_A binding site. Also shown are four of the surrounding amino acids that may interact with UQ_1^-.

Table 5.1 lists several ONIOM calculated parameters for UQ_1^- in the Q_A binding site. These parameters are compared with parameters derived for neutral UQ in the Q_A binding site derived from the 1AIJ crystal structure. Corresponding parameters are also listed for UQ^- (conformer A) in the gas phase (calculated using DFT), and for ONIOM calculated neutral UQ.

Figure 5.1B gives a detailed view of the amino acids surrounding the UQ^- cofactor, and suggests several possible pigment-protein interactions (show as dotted lines). The indole ring of TrpM252 may be involved in a π-stack interaction with the quinone ring. The C_1=O oxygen atom of UQ^- could be H bonded to the peptide NH group of AlaM260, while the C_4=O oxygen

atom of UQ^{-} could be H bonded to the imidazole nitrogen of HisM219. The other imidazole nitrogen atom of HisM219 provides a ligand to the non-heme iron atom.

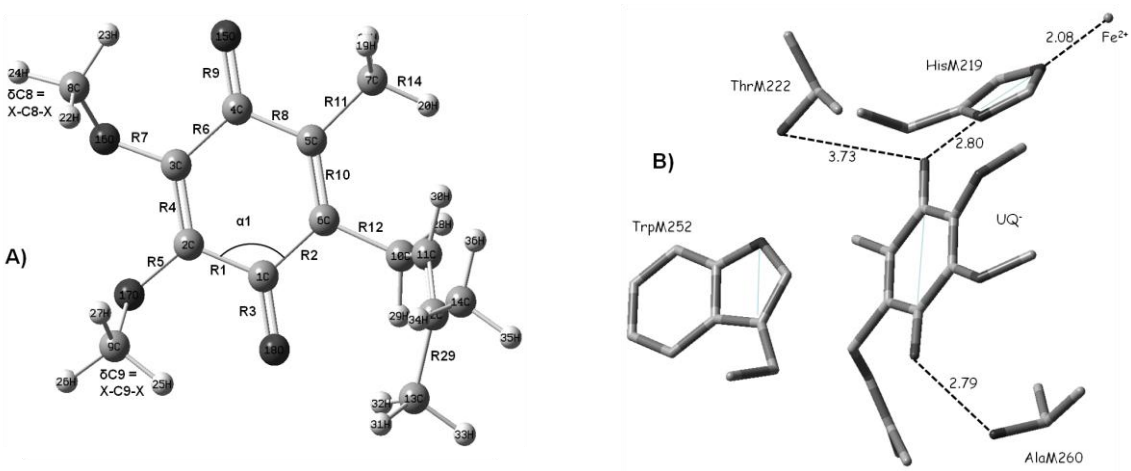

Figure 5.1 (A) Atom labeling and numbering scheme for UQ_1. The subscript refers to the number of isoprene units in the chain attached at C6. In our model the chain consists of a single isoprene unit. Some of the internal coordinates are also shown. R, α and δ represent bond stretching, angle bending and a combination of angle bends at a vertex atom respectively. (B) ONIOM calculated geometry optimized structure of UQ_1^{-} and four surrounding amino acids in the Q_A binding site. The dotted lines indicate possible hydrogen bonds. The possible hydrogen bond lengths are also shown. Three solid lines traversing the Trp, His and UQ rings are shown. The dihedral angles between these lines are listed in Table 5.1.

Table 5.1 indicates that the ONIOM calculated hydrogen bonding distances for both carbonyl groups of UQ^{-} are slightly shorter than that found for the neutral state. This is probably because the carbonyl bond lengths are longer for UQ^{-}, however.

The calculated C⋯⋯C bond lengths of UQ^{-} in the Q_A site are slightly longer than that calculated for the neutral state. The C⋯⋯O and C⋯⋯C bond lengths of UQ^{-} in the Q_A binding site are comparable to the corresponding values for UQ^{-} in the gas phase.

Table 5.1: Bond lengths (in Å) and angles (in degrees) for UQ_1 and UQ_1^{-} calculated using ONIOM methods. Corresponding parameters calculated for UQ_{1A} in the gas phase, and parameters for neutral UQ in the Q_A binding site derived from the 1AIJ crystal structure are also listed. The C_2 (C_3–C_2–O–CH_3) and C_3 (C_2–C_3–O–CH_3) dihedral angles are also listed, along with the angle of the H-bond to the C_1=O and C_4=O groups. Final, the dihedral angles between the solid lines across the Trp, UQ^{-} and His rings (shown in figure 5.1B) are also listed.

	Q_A	UQ_1 ONIOM	UQ_1^{-} ONIOM	UQ_{1A}^{-} Gas Phase
C_1⋯⋯O	1.234	1.227	1.272	1.273
C_4⋯⋯O	1.232	1.238	1.281	1.272
C_2⋯⋯C_3	1.404	1.366	1.382	1.380
C_5⋯⋯C_6	1.419	1.354	1.383	1.384
C_1⋯⋯O H-bond	2.837	2.837	2.790	
C_4⋯⋯O H-bond	2.788	2.868	2.798	
C_4=O - Fe	6.832	6.742	6.611	
H---O_1	1.912[a]	1.894	1.814	
H---O_4	1.788[a]	1.849	1.773	
N-H---O_1	150.2[a]	153.3	159.0	
N-H---O_4	166.2[a]	175.8	174.1	
H---O-C_1	133.4[a]	128.7	128.0	
H---O-C_4	140.6[a]	139.4	134.2	
C_2-dihedral angle	-57.1	-25.3	-35.3	-121.8
C_3-dihedral angle	109.5	150.5	123.1	122.4
C_2–C_1–O–HN (AlaM260)	-57.8[a]	-57.5	-62.4	
C_3–C_4–O–HN (HisM219)	77.1[a]	87.4	98.7	
Trp ring – UQ ring	-6.0	-3.4	-2.8	
His ring – UQ ring	-25.2	-55.2	-65.0	

a – values taken from hydrogen-optimized geometry.

For UQ^{-} in the Q_A binding site the C_4⋯O bond is slightly longer than C_1⋯O bond. This difference is not observed in gas phase calculations, and demonstrates an asymmetric interaction of the protein environment with the carbonyl groups of UQ^{-}.

The increase in C⋯C and C⋯O bond lengths seems to cause a decrease in the length of the hydrogen bonds between the carbonyl groups and nearby amino acids. From this one might expect more pronounced hydrogen bonding effects for UQ^{-} compared to UQ in the Q_A binding site.

The calculated methoxy group dihedral angles for UQ_1^{-} in Q_A binding site are close to that found for neutral UQ in the crystal structure. The C_3 methoxy dihedral angle for UQ_1^{-} is similar in both gas phase and ONIOM calculations. The C_2 methoxy dihedral angle in ONIOM calculations is rotated by ~ 86° from the angle found in gas phase calculations, however.

Table 1 demonstrates that both carbonyl hydrogen bonds (to Ala M260 and His M219) do not lie on the quinone ring plane. This indicates that any calculations based on the assumption of an O-H bond axis lying on the quinone ring plane cannot be valid [13, 56].

5.4.3 Calculated Vibrational Frequency of UQ_1^{-}

The ONIOM calculated IR absorption spectrum for UQ_1^{-} in the Q_A binding site in the 1540-1390 cm^{-1} region is shown in figure 5.2b. The DFT calculated spectrum for UQ_1^{-} in the gas phase is shown in figure 5.2a. Experimental spectra generally focus on this spectral region because this is where intense absorption bands associated with the C⋯C and C⋯O modes occur.

Clearly, the spectra in figure 5.2a and b differ considerably. The normal modes (frequencies, IR intensities, Raman activities and potential energy distributions) that contribute to the bands in the spectra in figure 5.2a and b are listed in Table 5.2.

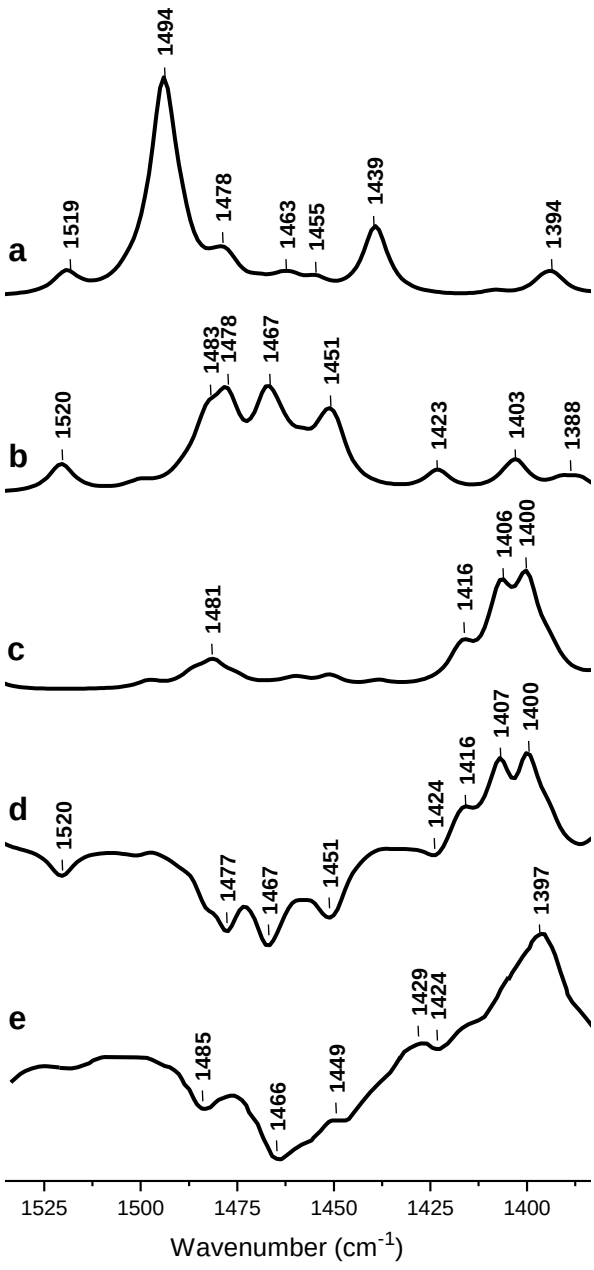

Figure 5.2. Calculated IR spectra for (a) unlabeled UQ_1^- in the gas phase, (b) unlabeled UQ_1^- in the Q_A binding site, (c) $^{13}C^{18}O$ labeled UQ_1^- in the Q_A binding site. (d) Isotope edited spectrum obtained by subtracting spectrum b from spectrum c. (e) Experimental $^{13}C^{18}O$ isotope edited FTIR double difference spectrum (taken from [16] with permission. Frequencies were scaled by 0.9771.

Table 5.2. Calculated IR frequencies, intensities, Raman activities and potential energy distributions of normal modes of UQ_1^- in the gas phase (*top*) and in the Q_A binding site (*bottom*).

ν	IR Intensity	Raman Activity	Potential Energy Distribution
UQ_{1A}^- Gas Phase			
1439	101	7	δCH3
1455	16	9	R3(9)-R10(5)+δCH2(29)+δCH3(43)
1464	12	1	δCH3
1477	36	39	δCH3(71)+δCH2(12)
1480	19	14	δCH3(65)+δCH2(13)
1490	44	234	R9(38)+R3(20)-R10(11)
1494	292	8	R3(31)-R9(24)+RD1(9)+δC13(8)
1499	15	39	δCH3(51)+δCH2(25)
1519	31	18	R4(33)-R10(17)-R5(6)-R7(6)+δC7(5)
1602	10	452	R4(26)+R10(24)+RD2(11)
UQ_1^- Q_A Binding Site			
1403	42	26	R8(18)-R2(11)+ δCH3(14)-RD3(9)
1423	29	10	δCH3
1450	66	19	R9(11)-R6(6)+δCH3(53)
1452	52	8	R3(14)-R10(5)+δCH3(37)+δCH2(18)
1458	33	17	R9(11)+δCH3(68)
1464	31	25	R9(7)+δCH3(56)+δCH2(7)
1466	25	72	R9(15)+δCH3(60)
1468	84	56	R9(24)+δCH3(49)
1477	93	104	R3(24)+δCH3(45)+δCH2(6)
1483	75	87	R3(33)+δCH3(31)+δCH2(10)
1499	9	11	δCH3
1521	41	33	R4(33)-R10(19)-R5(9)-R7(6)
1599	29	401	R10(27)+R4(24)+RD2(11)

Internal coordinates are defined in Figure 5.1B. Ri = i^{th} bond stretching; δCi = X-C_i-X bending for -CH_3, -CH_2- and –CH= groups; X = atom bonded to the atom C_i; RD1 = $6^{-1/2}$(α1- α2+ α3- α4+ α5- α6); RD2 = $12^{-1/2}$(2α1- α2- α3+2α4- α5- α6); RD3 = (½)(α2- α3+ α5- α6) = ring deformation; αi = C_{i-1}-C_i-C_{i+1} angle bending of ring atoms

For UQ_{1A}^- in the gas phase the calculated spectrum displays an intense band at 1494 cm^{-1} that is due mainly to the out of phase (antisymmetric) coupled vibration of both carbonyl groups

[R3(31)-R9(24%), where the minus sign indicates the relative phase of the vibration of the C=O group]. The in-phase stretching vibration of both carbonyl groups occurs at 1490 cm^{-1} and has very low intensity but considerable Raman activity (Table 5.2(*top*)).

The ONIOM calculated spectrum for UQ_1^- in the Q_A binding site (figure 5.2b) is very different from the DFT calculated gas phase spectrum (figure 2a), and displays three intense bands at ~1480, 1467 and 1451 cm^{-1}. The band at ~1480 cm^{-1} displays some substructure, with peaks near 1483 and 1478 cm^{-1}. Both of these peaks are due to normal modes that are predominantly C_1=O stretching vibrations (C_1=O stretching corresponds to internal coordinate R3) mixed with methyl group C-H bending vibrations (Table 5.2).

The band at 1467 cm^{-1} in the spectrum in figure 2b contains contributions from four normal modes (at 1468, 1466, 1464 and 1458 cm^{-1}), all of which are due to C_4=O stretching vibrations (R9) coupled to methyl group C-H bending vibrations (Table 5.2).

The calculated band at 1451 cm^{-1} is the spectrum in figure 2b contains contributions from two normal modes at 1452 and 1450 cm^{-1}. The 1450/1452 cm^{-1} mode contains some contribution from C_1=O/C_4=O stretching vibrations, respectively (Table 5.2).

The ONIOM calculated band at 1520 cm^{-1} is due mainly to the out of phase stretching vibrations of both C=C bonds. The in phase stretching vibrations of C=C lie 80 cm-1 above the out of phase vibrations. The bands due to C=C modes are thus at a higher frequency than the bands due to C=O modes for UQ^-.

Experimentally, it has proven difficult to establish which bands in (Q_A^- - Q_A) FTIR difference spectra are due to UQ or UQ^-. To address this problem the best approach has been to compare spectra obtained using PBRCs with unlabeled and specifically labeled UQ incorporated into the Q_A binding site. Only bands due to UQ will shift upon labeling, allowing their

identification. In addition the molecular group of UQ that gives rise to the different bands can be established by considering spectra obtained from samples with different types of isotope labeled UQ incorporated. One problem that has arisen in the interpretation of isotope edited FTIR difference spectra is that bands due to the labeled species downshift to frequencies where bands of the unlabeled species occur. This type of overlap causes spectral features to cancel out, making interpretation difficult. This problem is more pronounced for the anion state where isotope induced shifts are smaller. However, for UQ that has both carbonyl oxygen atoms ^{18}O labeled, as well as all carbon atoms ^{13}C labeled, the isotope induced downshifts are sufficiently large to minimize these band overlap effects.

Table 5.3. ONIOM calculated normal mode frequencies, intensities and potential energy distributions for $^{13}C^{18}O$ and $^{13}C_4$ labeled UQ_1^- in the Q_A binding. Isotope induced frequency shifts are also listed.

ν (cm^{-1})	$\Delta\nu$ (cm^{-1})	Intensity (km/mol)	Potential Energy Distribution (%)
$^{13}C^{18}O$ labeled Anion UQ_1			
1370	96, 17	163	R9(24)+R11(6)+δCH_3(52)
1400	68, -13	133	R9(29)-R6(7)+δCH_3(42)
1407	76, 70	119	R3(63)-R10(6)-R1(5)
1417	104	48	R4(11)-R9(11)+ δCH_3(58)
1439	19	8	R10(7)-R4(5)+ δCH_3(59)
1451	13	17	R10(9)+R3(7)+ δCH_3(55)
1481	40	33	R4(17)+ δCH_3(34)
1540	59	26	R10(26)+R4(23)+RD2(10)

Figure 5.2c shows ONIOM calculated IR spectra for simultaneously ^{13}C and ^{18}O labeled UQ^- in the Q_A binding site. By subtracting the spectrum in figure 5.2b from the spectrum in figure 5.2c, a $^{13}C^{18}O$ isotope edited IR double difference spectrum is obtained, which is shown in figure 2d. The spectrum in figure 2d can be directly compared to the corresponding experimental spectrum, which is shown in figure 5.2e. In figure 5.2d and e negative/positive

bands are associated with unlabeled/$^{13}C^{18}O$ labeled UQ_1^-, respectively. The agreement between the calculated and experimental spectra in figure 2d and e is striking.

Given the large $^{13}C^{18}O$ isotope induced band-shifts the experimental spectrum in figure 5.2e, above ~1430 cm^{-1}, represents a nearly pure absorption spectrum (inverted) of unlabeled UQ^- in the Q_A binding site. Similarly the spectrum below ~1430 cm^{-1} represents a nearly pure absorption spectrum of $^{13}C^{18}O$ labeled UQ^- in the Q_A binding site. Above ~1430 cm^{-1}, all of the calculated bands associated with unlabeled UQ_1^- clearly correspond to bands in the experimental spectrum. That is, negative bands at 1477, 1467, 1451 and 1424 cm^{-1} in the calculated spectrum correspond to bands at 1485, 1466, 1449 and 1424 cm^{-1} in the experimental spectrum. Suggestions as to the origin of the bands in the experimental spectrum have been made [15, 16]. However, the calculated data presented here allow a more detailed analysis and interpretation. The normal modes that contribute to the bands in the spectrum of unlabeled UQ^- (figure 5.2b, or the negative bands in figure 5.2d) were described above. The normal modes that contribute to the bands of $^{13}C^{18}O$ labeled UQ^- are listed in Table 5.3. The $^{13}C^{18}O$ isotope induced frequency shifts are also listed. The symmetric C⋯C ring stretching mode downshifts by 59 cm^{-1} upon $^{13}C^{18}O$ labeling from 1599 cm^{-1} of unlabeled ubisemiquinone in Q_A binding site of PBRCs. The weak band at 1520 cm^{-1} is mainly due to C⋯C asymmetric stretching vibration with contribution from C_2-O and C_3-O. This mode mixes with the C⋯O stretching and C-H bending modes upon $^{13}C^{18}O$ labeling and hence contributes to at least five bands. The broad band ~ 1480 cm^{-1} is due to mixed C_1⋯O stretching and methoxy bending vibrations. Similarly, the 1667 cm^{-1} is due to mixed C_4⋯O stretching and methoxy bending vibrations. The third intense band at 1451 cm^{-1} is contributed from both C_1⋯O and C_4⋯O stretching vibrations. Upon $^{13}C^{18}O$ labeling of UQ^- the

C⋯C also mix with carbonyl stretching and methyl bending vibrations and several complex IR bands appears in the frequency region below 1450 cm^{-1}.

Calculated IR spectra, frequency, isotope labeled frequency shifts and potential energy distribution of $^{13}C_1$, $^{13}C_4$, ^{13}C and ^{18}O labeled ubisemiquinone in the Q_A binding site of Rb. sphaeroides reaction centers are given in appendix D.

5.5 Discussion

5.5.1 Anion UQ geometry and H-bonding distances

The methoxy group orientations of UQ in the Q_A binding site of the Rb. sphaeroides RC do not alter much upon reduction of the molecule. In both cases the molecule remains as conformer A [50, 53]. However, the carbonyl and C⋯C bond lengths have lengthened in the radical ubiquinone molecule compared to the neutral ubiquinone molecule. These phenomena observed both in the gas phase and in the Q_A binding site of Rb. sphaeroides reaction center. The increase in the size of the ubiquinone upon reduction causes the decrease in the hydrogen bonding lengths of either carbonyl group to the surrounding amino acids in the Q_A binding site of Rb. sphaeroides RC. This observation supports the observation made by W. Lubitz and G. Feher that Q_A^- should have at least two hydrogen bonds of different strengths to the carbonyl oxygens [57]. However, the observation that both of the Ala M260 hydrogen and the His M219 hydrogen do lie in the position almost perpendicular to the quinone ring plane in both neutral and reduced state of the quinone and any calculations based on the assumption of O-H bond axis in the quinone plane cannot be valid [13, 56, 57]. This observation does not support very strong hydrogen bonding to either carbonyl group of Q_A.

5.5.2 Anion UQ C⋯⋯C vibrations and experimental resonance Raman spectra

The anion ubiquinone C⋯⋯C tail FTIR band lies at least 90 cm^{-1} higher frequency than the C=C ring and carbonyl FTIR bands also in the Q_A site of Rb. sphaeroides RC like it is observed in the gas phase and the solvents (see chapter 3). The C⋯⋯C tail vibration has negligible IR intensity and does not expect to be seen in the FTIR spectrum. This is also not observed in the experimental resonance Raman spectra [46]. Hence we can conclude that tail C⋯⋯C stretching vibration does not have any appreciable trace in the FTIR spectrum of anion UQ.

The C⋯⋯C ring in-phase vibration has very high Raman activity compared to C⋯⋯C ring out-of-phase vibration and Carbonyl stretching vibrations. The C⋯⋯C in-phase and out-of-phase modes of anion UQ_1 in the Q_A binding site are observed 3 cm^{-1} below and 2 cm^{-1} above the corresponding bands in the gas phase calculations. This observation is consistent with the experimental anion resonance Raman bands of anion UQ in the Q_A binding site of Rb. sphaeroides RC and in dichloroethane [46]. Hence, we can claim that the C⋯⋯C ring stretching vibrations of anion UQ should not be responsible for the splitting of carbonyl band in to three equivalent modes in the Rb. sphaeroides RC. The calculated C⋯⋯C ring FTIR bands of anion UQ in the Q_A binding site of Rb. sphaeroides RC do not change upon $^{13}C_1$, $^{13}C_4$ and ^{18}O labeling (see Table 8.2). However, the C⋯⋯C ring out-of-phase mode mixes with the carbonyl and CH bending modes upon ^{13}C (see Table 8.2) and $^{13}C^{18}O$ labeling.

5.5.3 Carbonyl bands

Why the unique intense carbonyl FTIR band of anion UQ in the solution into three equivalent bands [14, 16, 44] in the QA site of Rb. sphaeroides RC is the key point of this research. The carbonyl groups of UQ are much sensitive to the protein binding site. They can be affected by hydrogen bonding with the nearby amino acids, π-electron interaction from the

tryptophan ring and electronic embedding from the electronic charge on the atoms in the binding site. Vibrational properties of UQ carbonyl groups also depend on the orientation of methoxy groups [50]. The anion UQ has four conformations with respect to methoxy group orientations in the gas phase and in solvent (see chapter 3). However, all four anion UQ conformers have similar carbonyl FTIR bands both in the gas phase and in solvent. The anion UQ_1 optimized in the Q_A binding site is much closer to the conformer A of the anion UQ in the gas phase and in solvent. Hence, the orientation of carbonyl group cannot be the reason for splitting of the carbonyl band in Q_A binding site. The hydrogen bonding direction and distances of carbonyl groups with respect to the imidazole NH and peptide NH are not much different from each other. C_1⋯O to backbone nitrogen atom of alanine is 0.008 Å shorter than C_4⋯O to N_ϵ of histidine in the optimized geometry. The main reason of carbonyl band splitting may be the collective effect of electronic charge in the Q_A binding site including iron charge and the π-electron interaction from the tryptophan ring.

We have observed that the carbonyl vibrations highly mix with the CH bending vibrations in the unlabeled anion UQ in the Q_A binding site of Rb. sphaeroides RC. Such effect has never been considered [14-16, 44]. In the gas phase or in solvents the carbonyl vibration lie at higher frequency region than the CH bending vibration. The collective effect of the protein binding site should lower the carbonyl band position to the CH bending region in order to have coupling with the CH bending modes. Analysis of a vibrational mode becomes complex when more than two modes couple. From the complicated nature of vibrational modes it is even more difficult to precisely measure the extent of impact of the binding site on the individual carbonyl groups.

CHAPTER 6
CALCULATED VIBRATIONAL PROPERTIES OF CHAINLESS SYMMETRICAL QUINONES OCCUPYING THE Q_A BINDING SITE IN PURPLE BACTERIAL PHOTOSYNTHETIC REACTION CENTERS

6.1 Abstract

ONIOM (QM/MM) calculations were undertaken in order to simulate Q_A^-/Q_A isotope edited FTIR difference spectra obtained using *Rhodobacter sphaeroides* photosynthetic reaction centers with unlabeled and ^{18}O labeled chainless symmetrical quinones incorporated into the Q_A binding site. Isotope edited FTIR difference spectra were calculated for reaction centers with 2,3-dimethoxy-5,6-dimethyl-1,4-benzoquinone (MQ_0), 2,3,5,6-tetramethyl-1,4-benzoquinone (duroquinone, DQ), and 2,3-dimethyl-l,4-naphthoquinone (DMNQ) incorporated, and compared to corresponding experimental spectra. The calculated and experimental spectra agree remarkably well. Such good agreement cannot be obtained by considering quinone molecules in the gas phase. Calculations including the protein environment are required.

For all quinones incorporated the ONIOM calculations indicate that both quinone carbonyl groups are relatively weakly hydrogen bonded. The protein provides an asymmetric hydrogen bonding environment for the incorporated quinones, however. For DMNQ and DQ the carbonyl vibrational modes are calculated to be separated by 10-13 cm^{-1}. For MQ_0 incorporated into the Q_A binding site the separation of the carbonyl modes is likely similar to that for the DMNQ and DQ.

Isotope edited FTIR difference spectra were calculated for reaction centers with corresponding "tail" containing quinones incorporated into the Q_A binding site, and is found that replacement of the quinone methyl group by a phytyl or prenyl chain does not alter ONIOM calculated spectra.

The quinone “tail” does not significantly modify the asymmetrical bonding of the quinone head-group in the Q_A binding site, although calculations show that it does appear to impose a small geometrical constraint on the orientation of the quinone ring.

6.2 Introduction

Quinones play an important role in biological proton and electron transfer processes that occur in both respiration and photosynthesis [58]. In type II photosynthetic reaction centers two quinone molecules act as terminal electron acceptors [21, 59]. The two quinones are often termed Q_A and Q_B. In this manuscript we will refer to the quinone binding site as Q_A and Q_B, however. The quinones that occupy the Q_A and Q_B binding sites have very different functions. The Q_A quinone is an intermediary cofactor involved in transferring electrons from (bacterio)pheophytin to Q_B, while the Q_B quinone couples proton and electron transfer processes [22, 23, 59].

In this manuscript we focus on the Q_A binding site. The quinone occupying the Q_A binding site is species dependent. In *Rhodobacter* (*Rb.*) *sphaeroides* purple bacterial reaction centers (PBRCs) a ubiquinone (UQ) molecule occupies the Q_A binding site. In PBRCs from *Blastochloris Viridis* [60] and *Chloroflexus aurantiacus* [61] a menaquinone occupies the Q_A binding site. In photosystem II reaction centers from oxygen evolving organisms, a plastoquinone (PQ) molecule occupies the Q_A binding site. In photosystem I the secondary electron acceptor, termed A_1, is a vitamin k_1 (VK) molecule (also called phylloquinone).

Figure 1 shows the structure, numbering and abbreviations we will use for the various quinones discussed in this manuscript. MQ_0 and DMNQ are UQ and VK analogues, respectively, in which the hydrocarbon tail has been replaced with a methyl group. DQ is a PQ analogue in which methyl groups have been substituted at C_5 and C_6.

It has been suggested that the role of the hydrocarbon chain at C_6 is to anchor and orient the quinone head-group in a specific way [62]. Data is available that may argue against this proposal, however[43].

Comparison of the properties of PBRCs with MQ_0 and UQ_n, or VK and DMNQ, incorporated into the Q_A binding site will allow one to assess how or if the hydrocarbon chain at C_6 modifies the quinones functional properties. Similarly, comparison of the properties of PBRCs with MQ_0 and DQ incorporated into the Q_A binding site will allow one to assess how or if the methoxy groups at C_2 and C_3 modifies the quinones functional properties.

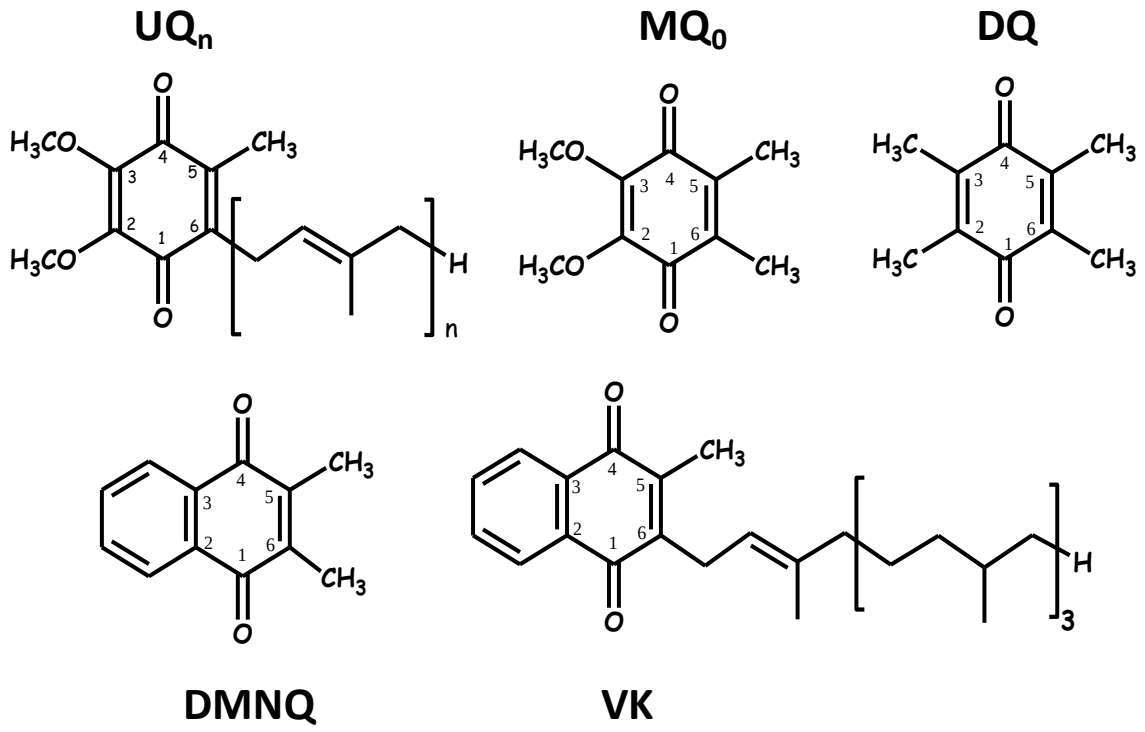

Figure 6.1: Structure and numbering for ubiquinone (2,3-dimethoxy, 5-methyl,6-prenyl benzoquinone) (UQ_n), 2,3-dimethoxy, 5,6-methyl benzoquinone (MQ_0), 2,3,5,6-methyl benzoquinone (duroquinone or DQ), 2,3-dimethyl, 1,4-naphthoquinone (DMNQ) and 2-methyl, 3-phytyl 1,4-naphthoquinone [vitamin K_1 (VK)]. Menaquinone is identical to vitamin K_1 except for the degree of saturation of the tail at C_6. The numbering scheme employed here for the naphthoquinone structures is non standard. This numbering scheme was chosen to facilitate comparison between naphthoquinone and ubiquinone structures.

Fourier transform infrared (FTIR) difference spectroscopy (DS) is a sensitive molecular-level probe of pigment-protein interactions, and it is widely used to study both the neutral and reduced states of quinones in PBRCs [24] and in photosystem II [63]. In this manuscript we focus on Q_A^-/Q_A FTIR DS. Many molecular species contribute to Q_A^-/Q_A FTIR DS, and in the past it has been difficult to identify which bands are associated specifically with UQ in the Q_A site. However, fully functional quinones can be incorporated into Q_A depleted PBRCs, and by collecting Q_A^-/Q_A FTIR DS using PBRCs with unlabeled and isotopically labeled quinones incorporated it has proven possible to separate contributions of the quinones from those of the protein in Q_A^-/Q_A FTIR DS[24]. Q_A^-/Q_A FTIR DS have been obtained using PBRCs with a variety of unsubstituted and substituted quinone analogues incorporated into the Q_A binding site. The goal of such experiments is to assess how the various molecular groups of the quinones may contribute to its functional properties.

Although experimental Q_A^-/Q_A FTIR DS have been obtained using PBRCs with various unlabeled and isotope labeled quinones incorporated, virtually no computational work aimed at modeling the experimental FTIR DS have been undertaken. Calculations aimed at modeling the vibrational properties of quinones in the Q_A binding site must account for the protein environment. Quantum mechanical (QM) calculations of such a large molecular system (pigment plus protein environment) are unfeasible. To circumnavigate this problem methods have been developed that allow one to separate the molecular system into distinct layers that can be treated at different levels of theory. In one layer the chemical properties of the principle species of interest (the pigment) can be calculated using "high-level" QM methods. The surrounding protein environment is included in the calculation but it is treated using computationally less expensive molecular mechanics (MM) methods.

Recently we have undertaken QM:MM calculations for UQ in the Q_A binding site using the ONIOM method [64]. ONIOM is an acronym for: our Own N-layered Integrated molecular Orbital + Molecular mechanics package. In these calculations we showed that we could simulate experimental isotope edited FTIR difference spectra obtained using PBRCs with neutral UQ in the Q_A binding site. Here we extend upon these previous studies by attempting to simulate experimental isotope edited FTIR difference spectra obtained using PBRCs with symmetric chainless quinones incorporated into the Q_A binding site. We show that the calculated spectra agree well with the experimental spectra, further supporting the notion that the ONIOM method is a useful approach for understanding complex FTIR difference spectra associated with pigments in protein binding sites.

6.3 Materials and Methods

6.3.1 Model Construction. All molecular models were constructed using the crystal structure of *Rb. sphaeroides* PBRCs at 2.2 Å resolution [65] (PDB file 1AIJ). The ONIOM model includes all amino acid atoms within 10 Å of either carbonyl oxygen atom of UQ. The different incorporated quinones are initially set up with the C=O groups in an identical orientation to that found for UQ in the binding site. For ONIOM geometry optimization all atoms associated with the protein backbone, and the non-heme iron atom, are held fixed. All atoms of the amino acid side chains and the incorporated quinone are unconstrained. For calculations of UQ/VK the hydrocarbon tail was modeled as a single prenyl/phytyl unit, respectively. Inclusion of further prenyl/phytyl units did not alter the calculated spectra (not shown).

6.3.2 Calculations. For calculation of UQ molecules in the gas phase, and for the QM part of ONIOM calculations, molecular geometry optimizations and harmonic vibrational frequency calculations were undertaken using hybrid DFT methods, employing the B3LYP functional and

the 6-31+G(d) method within Gaussian 03 [33]. This choice of functional and basis set are appropriate for calculation of the vibrational properties of quinones[40, 66]. The MM part of the ONIOM calculation is undertaken using AMBER [67]. Following ONIOM geometry optimization of the protein-quinone system, the optimized quinone molecule is considered separately for vibrational frequency analysis. Calculated normal mode vibrational frequencies presented here are scaled by 0.9608 (gas phase) and 0.9723 (ONIOM). Such scaling factors are standard [68].

6.3.3 Normal Mode Assessment. Assignment of calculated vibrational frequencies to molecular groups is based on a consideration of the calculated atomic displacements (in Cartesian coordinates) associated with the normal modes. These atomic displacements can be animated using software (GaussView03), and the molecular groups that most prominently contribute to the normal modes can be assessed visually. In addition, potential energy distributions of the normal modes are calculated using the freeware GAR2PED[49]. Normal mode frequencies and intensities are calculated. With both the frequency and intensity information IR absorption spectra (stick spectra) are constructed, as described previously[50]. The stick spectra are convolved with a Gaussian function with half-width of 4 cm^{-1} to produce more realistic looking spectra.

6.4 Results

6.4.1 UQ structure and numbering. Figure 6.1 shows the structure and numbering scheme used here for UQ_n, MQ_0, DQ, DMNQ and VK. Naphthoquinones generally have a different numbering scheme. We have applied the UQ numbering scheme to DMNQ and VK for the sake of easy comparison. Figure 2 shows a picture of (A) DMNQ, (B) VK, (C) MQ_0 and (D) UQ_1 in the Q_A binding site with three of the surrounding amino acids. The structures shown are after

geometry optimization using ONIOM methods. Possible hydrogen bonds (or ligand to the non-heme iron atom) are indicated by dotted lines.

Table 6.1 lists several bond lengths and bond angles derived from the ONIOM calculated optimized geometries of the various quinones in the Q_A binding site. For comparison, table 6.1 also lists corresponding bond lengths and angles derived from DFT calculated optimized geometries of the various quinones in the gas phase.

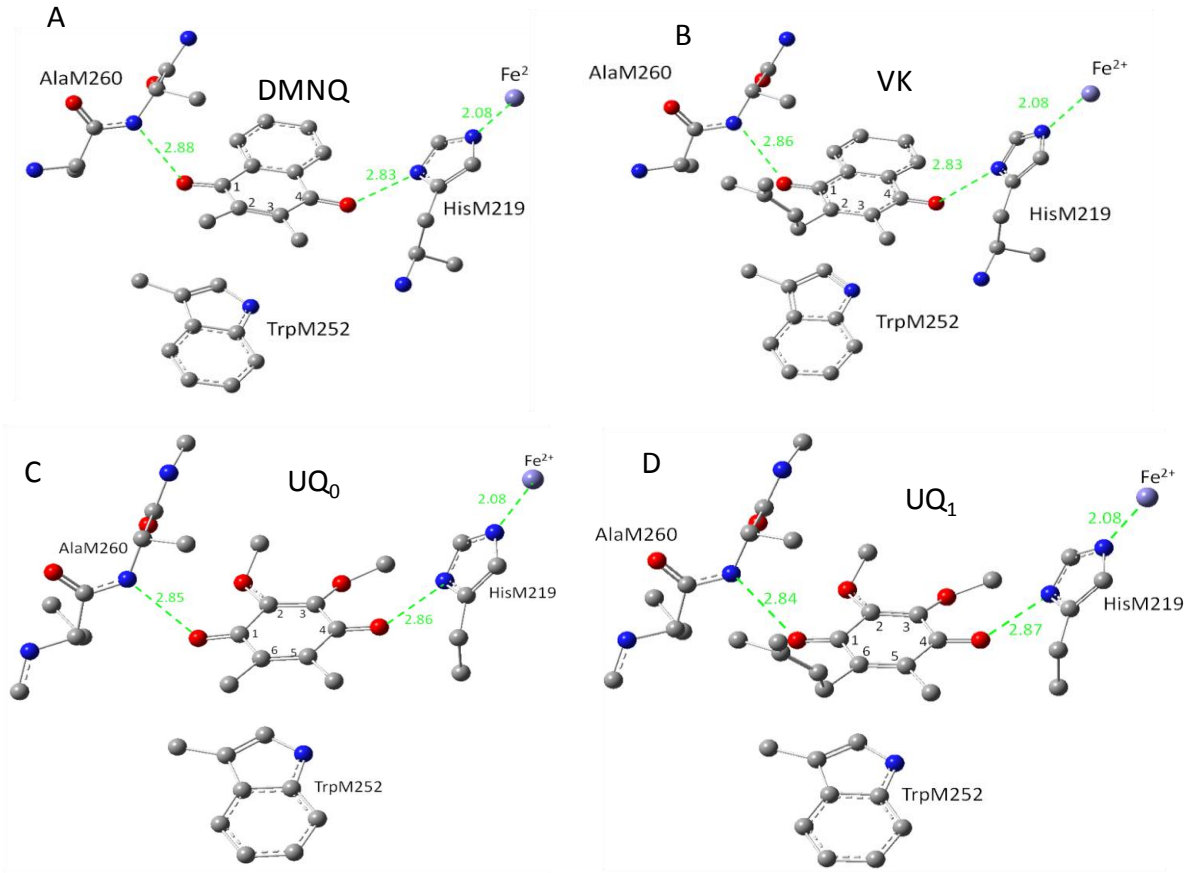

Figure 6.2: Structure of (A) DMNQ, (B) VK, (C) MQ_0 and (D) UQ_1 in the Q_A binding site in PBRCs from *Rb. sphaeroides*. Structure is after geometry optimization using ONIOM methods. Possible H-bonds (or ligands) are shown as dotted lines and distances quoted are in Å. Hydrogen atoms have been omitted for clarity.

Table 6.1: Comparison of bond lengths and angles derived from the ONIOM calculated (O) and gas phase calculated (GP) optimized geometry of neutral UQ_1, VK, DMNQ and MQ_0. Bond lengths and angles taken directly from the 1AIJ crystal structure are also listed. Distances are in Å and angles are in degrees. [a]from[50].

	Crystal Structure	UQ_1		MQ_0		DQ		VK_1		DMNQ	
		O	GP	O	GP	O	GP	O	GP	O	GP
C_1=O	1.234	1.227	1.223	1.227	1.223	1.232	1.230	1.233	1.229	1.232	1.229
C_4=O	1.232	1.238	1.231	1.238	1.231	1.236	1.231	1.236	1.229	1.236	1.229
C_2=C_3	1.404	1.366	1.364	1.367	1.364	1.357	1.355	1.405	1.405	1.406	1.405
C_5=C_6	1.419	1.354	1.354	1.354	1.354	1.355	1.355	1.363	1.361	1.362	1.360
C_4=O H-bond	2.788	2.868		2.865		2.829		2.856		2.878	
C_1=O H-bond	2.837	2.837		2.846		2.895		2.832		2.831	
C_4=O - Fe	6.832	6.744		6.715		6.627		6.692		6.637	
Tail Angle	113.0	114.9	111.7					114.7	111.6		
C_2-dihedryl	-57.1	-25.3	-8.9[a]	-26.5	-10.1						
C_3-dihedryl	109.5	150.5	123.6[a]	150.6	123.1						

For UQ_{10} in the Q_A site the 1AIJ crystal structure [65] indicates that the C_1=O bond is marginally longer than the C_4=O bond. (1.234 *versus* 1.232 Å). In contrast, from ONIOM calculations of all the quinones listed in table 6.1 the C_1=O bond is shorter than the C_4=O bond.

In gas phase calculations the C_1=O and C_4=O bond lengths are shorter than that found in ONIOM calculations (except the C_1=O of DQ). This lengthening of the C=O bonds of the quinones in the Q_A binding site is related to hydrogen bonding and other electrostatic interactions of the pigment with the protein environment.

For UQ_1 and MQ_0 the C_1=O bond is shorter than the C_4=O bond in both ONIOM and gas phase calculations. This difference in C_1=O and C_4=O bond lengths in UQ_1 and MQ_0 (at least in the gas phase calculations) must relate to the differing orientations of the C_2 and C_3 methoxy

groups. The C_2 and C_3 methoxy group dihedral angles are defined as the C_3-C_2-O-CH_3 and C_2-C_3-O-CH_3 dihedral angles. The ONIOM calculated C_2 and C_3 methoxy group dihedral angles for UQ_1 are -25.3 and 150.5^o (table 6.1). Similar angles are calculated for MQ_0. The calculated dihedral angles for UQ_1 in the gas phase, and the observed angles for UQ_{10} in the Q_A binding site (from the crystal structure) are within 32 degrees of that calculated for UQ_1 using ONIOM methods.

For UQ_{10} in the Q_A site the crystal structure indicates that the C_2=C_3 bond is shorter than the C_5=C_6 bond. (1.404 *versus* 1.419 Å). In contrast, for all quinones except DQ, in both ONIOM and gas phase calculations the C_2=C_3 bond is longer than the C_5=C_6 bond. For VK and DMNQ the calculated C_2=C_3 and C_5=C_6 bond lengths are considerably different.

For UQ_1 and VK the tail makes a distinct "kink" after the first carbon atom (figure 6.2B, D). The C-C-C bond angle is 112-115^o for both quinones in both the ONIOM and gas phase calculations. The calculated angles are virtually the same as that found in the crystal structure (table 6.1). Given these similarities (between the ONIOM and gas phase calculations, for both the naphthoquinone and benzoquinone species, as well as between calculation and experiment) the suggestion is that the protein environment does not constrain the orientation of the quinone ring relative to the tail.

Figure 6.3A shows ONIOM calculated ^{18}O isotope edited difference spectra for neutral VK and DMNQ in the Q_A binding site. Figure 6.3D shows corresponding DFT calculated spectra for VK and DMNQ in the gas phase. Experimental spectra are also shown (figure 3B and C) for comparison. Positive/negative bands in the isotope edited spectra are due to the unlabeled/^{18}O labeled quinone species, respectively. The ONIOM calculated spectra clearly better describe the

experimental spectra. Calculations including the protein environment are necessary in order to adequately simulate the experimental spectra.

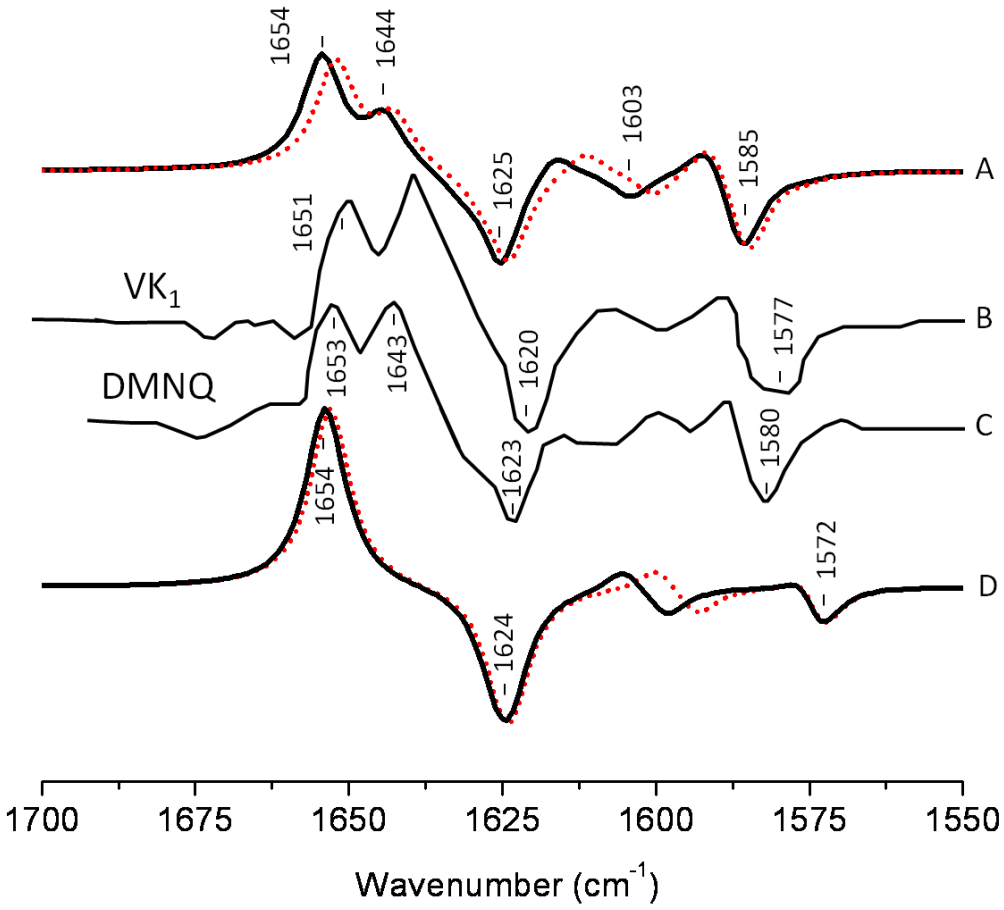

Figure 6.3: (A) ONIOM calculated ^{18}O isotope edited DDS for neutral VK (*dotted*) and DMNQ (*solid*) in the Q_A binding site. Experimental spectra for VK (B) and DMNQ (C) are also shown, and were taken from reference [69], with permission. (D) DFT calculated ^{18}O isotope edited DDS for neutral VK (*dotted*) and DMNQ (*solid*) are also shown. ONIOM/gas phase calculated spectra were scaled by 0.9718/0.9608, respectively.

Table 6.2: Normal mode frequencies (in cm^{-1}), intensities (in km/mol) and PEDs (in %) calculated using ONIOM methods for unlabeled and ^{18}O labeled neutral DMNQ (*bold text*), VK_1, DQ, MQ_0 and UQ_1. Frequency shifts upon ^{18}O labeling are also listed. Negative signs in the PEDs refer to the relative phase of vibration of the internal coordinates. Only internal coordinates that contribute at least 6% are shown. Mode frequencies were scaled by 0.9718.

Unlabeled				
	ν	I		Potential Energy Distribution
DMNQ	1654	235		C_1=O (71)
VK	1652	224		C_1=O (69)
DQ	1632	181		C_1=O (83)
MQ_0	1666	209		C_1=O (81)
UQ_1	1663	185		C_1=O (80)
DMNQ	1644	108		C_4=O (60)
VK	1642	107		C_4=O (60)
DQ	1646	254		C_4=O (83)
MQ_0	1627	270		C_4=O (70), -C_2=C_3 (8)
UQ_1	1626	305		C_4=O (68), -C_2=C_3 (9)
DMNQ	1617	59		C_5=C_6 (61), -C_4=O (8)
VK	1611	54		C_5=C_6 (60), -C_4=O (8)
DQ	1620	55		C_5=C_6 (38), -C_2=C_3 (33)
MQ_0	1657	20		C_5=C_6 (52), C_2=C_3 (15)
UQ_1	-	-		-
DMNQ	1591	93		C_7=C_8 (15), -C_9=C_{10} (14), C_2=C_{10} (14), -C_3=C_7 (12)
VK	1591	96		C_7=C_8 (15), -C_9=C_{10} (14), C_5=C_{10} (13), -C_3=C_7 (12), -C_4=O (5)
DQ	-	-		-
MQ_0	1601	293		C_2=C_3 (39), -C_5=C_6 (15)
UQ_1	1601	275		C_2=C_3 (35), -C_5=C_6 (18), C_4=O (14), -C_2=O (6)
^{18}O labeled				
			Δν	
DMNQ	1631	32	23	C_1=O (28), C_5=C_6 (22), C_2=C_3 (10)
VK	1628	29	24	C_1=O (32), C_5=C_6 (16), C_2=C_3 (6)
DQ	1599	144	33	C_1=O (81)
MQ_0	1631	211	35	C_1=O (83)
UQ_1	1629	187	34	C_1=O (82)
DMNQ	1625	199	19	C_4=O (26), -C_1=O (21), C_5=C_6 (8), -C_3=C_7 (7)
VK	1624	188	18	C_4=O (29), -C_1=O (15), C_5=C_6 (8), -C_3=C_7 (7)
DQ	1613	264	33	C_4=O (80)
MQ_0	1587	265	40	C_4=O (63), C_2=C_3 (9), -C_5=C_6 (5)
UQ_1	1586	249	40	C_4=O (65), C_2=C_3 (7), -C_5=C_6 (6)
DMNQ	1604	54	13	C_5=C_6 (37), - C_4=O (25), -C_1=O (14)
VK	1600	52	11	C_5=C_6 (42), -C_4=O (20), -C_1=O (14)

DQ	1620	56	0	$C_5=C_6$ (37), $-C_2=C_3$ (34)
MQ_0	1657	8	0	$C_5=C_6$ (49%), $C_2=C_3$ (13%)
UQ_1	-	-	-	-
DMNQ	1586	181	5	$C_7=C_8$ (14), $-C_4=O$ (13), $C_2=C_{10}$ (12), $-C_9=C_{10}$ (10), $C_1=O$ (10), $-C_3=C_7$ (7)
VK	1585	186	6	
DQ	-	-	-	$-C_7=C_8$ (14), $C_4=O$ (14), $-C_2=C_{10}$ (11), $-C_9=C_{10}$ (9), $C_1=O$ (11), $-C_6=C_7$ (6)
MQ_0	1609	273	-7	
UQ_1	1609	308	-8	-
				$C_2=C_3$ (40), $-C_1=O$ (15), $-C_5=C_6$ (12)
				$C_2=C_3$ (37), $-C_1=O$ (13), $-C_5=C_6$ (15), $-C_2$-O (10)

Figure 6.3 shows that except for a small frequency shift in some of the modes, the calculated spectra for DMNQ and VK are virtually the same. Replacement of the methyl group at C_6 with an isoprene unit therefore has no influence on the calculated spectra.

The normal modes (frequencies and intensities) that give rise to the various bands in the ONIOM calculated ^{18}O isotope edited spectra of DMNQ and VK are listed in table 6.2. The potential energy distributions (PEDs), which quantify to what extent various internal coordinates contribute to the normal modes, are also listed in table 6.2. Results for DMNQ and VK are very similar. Below we will discuss calculated data obtained for DMNQ with the recognition that very similar results and conclusions also apply to VK.

In the ONIOM calculated ^{18}O isotope edited spectra for DMNQ the two bands at 1654 and 1643 cm^{-1} are due predominantly to $C_4=O$ and $C_1=O$ stretching vibrations, respectively (table 2). In contrast, in gas phase calculation the two C=O modes of DMNQ are (antisymmetrically) coupled[40], giving rise to a single intense band at 1654 cm^{-1} (figure 6.3D)

In ONIOM calculations it is found that upon ^{18}O labeling the $C_4=O$ and $C_1=O$ modes f DMNQ downshift 23 and 19 cm^{-1}, to 1631 and 1625 cm^{-1}, respectively (table 2). Upon ^{18}O labeling the 1625 cm^{-1} mode is considerably more intense than the 1631 cm^{-1} mode. The 1625 cm^{-1} mode in ^{18}O labeled DMNQ is due mainly to the antisymmetric coupled vibration of both C=O groups. That is, two separate C=O modes of unlabeled DMNQ couple upon ^{18}O labeling.

This behavior is not predicted based upon consideration of the experimental spectra, where it is "assumed" that the two C=O modes of DMNQ remain separate upon ^{18}O labeling [69].

A C=C mode of the quinone ring of DMNQ is found at 1617 cm^{-1}. This quinone C=C mode downshifts 13 cm^{-1}, to 1604 cm^{-1}, upon ^{18}O labeling, with little change in intensity. The 1604 cm^{-1} mode composition in ^{18}O labeled DMNQ displays considerable mixing of the C=O and C=C modes (the C=O modes account for 39% of the PED). This behavior might be expected given that the C=O and C=C modes are closer in frequency upon ^{18}O labeling.

A C=C mode of the aromatic ring of DMNQ occurs at 1591 cm^{-1}. This aromatic C=C mode downshifts 5 cm^{-1} to 1586 cm^{-1} upon ^{18}O labeling. The 1586 cm^{-1} mode in ^{18}O labeled DMNQ displays some mixing with C=O modes (23%), and the intensity of the aromatic C=C mode nearly doubles upon ^{18}O labeling. The calculated C=C normal modes and their interpretation in terms of internal coordinates, as well as the calculated ^{18}O induced frequency shifts are similar to that suggested on the basis of the experimental spectra [69].

Figure 6.4A shows ONIOM calculated ^{18}O isotope edited IR difference spectra for neutral DQ in the Q_A binding site. Figure 4C shows corresponding DFT calculated spectrum for DQ in the gas phase. The experimental spectrum is shown in figure 4B. Again, the ONIOM calculated spectrum is in line with the experimental spectrum, while the DFT calculated gas phase spectrum is not. The ONIOM calculated normal modes (frequencies and intensities) that give rise to the bands in the ^{18}O isotope edited spectrum for DQ, as well as the PEDs, are listed in table 6.2

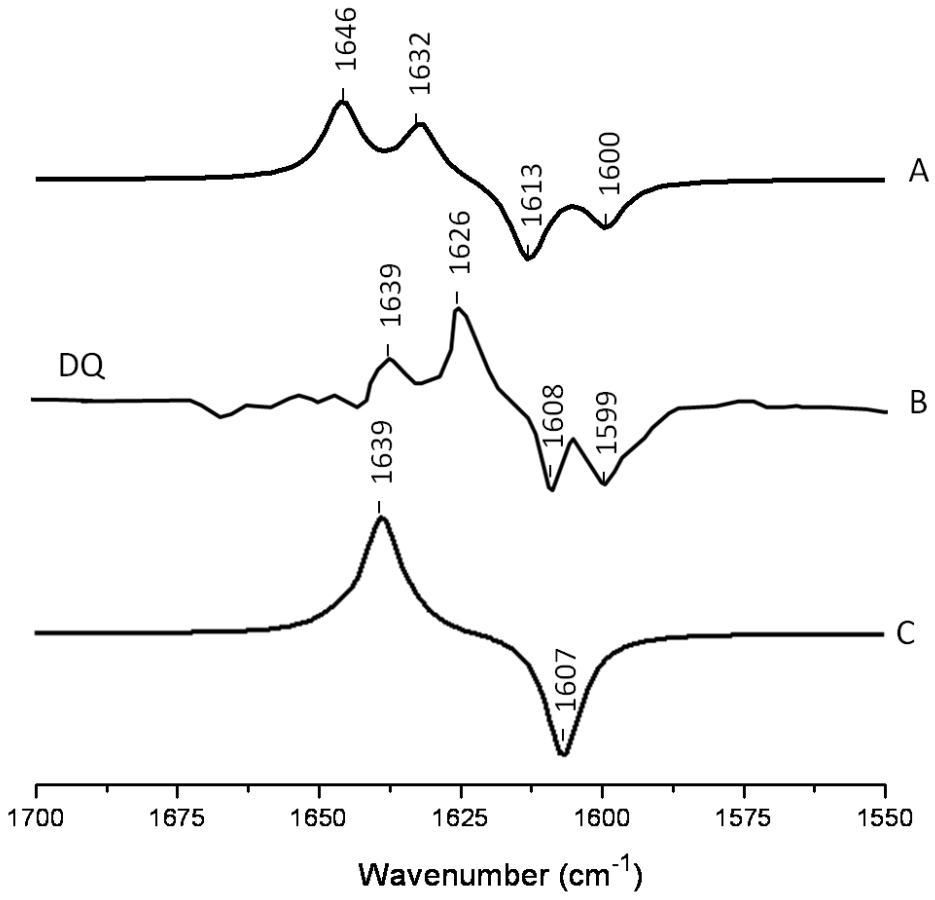

Figure 6.4: (A) ONIOM calculated ^{18}O isotope edited DDS for neutral DQ in the Q_A binding site. Experimental spectra are shown in (B), and were taken from reference [69] with permission. (C) DFT calculated ^{18}O isotope edited DDS for neutral DQ. ONIOM and gas phase calculated spectra were scaled by 0.9718 and 0.9608, respectively.

In the ONIOM calculated ^{18}O isotope edited spectrum for DQ the two bands at 1646 and 1632 cm^{-1} are due to C_1=O and C_4=O stretching vibrations, respectively (table 2). Upon ^{18}O labeling the C_4=O and C_1=O modes both downshift 33 cm^{-1} with little change in mode intensities (table 2). This 33 cm^{-1} downshift is large compared to that calculated for DMNQ in the Q_A site, (19-23 cm^{-1}). For DQ, the ONIOM calculated mode composition is virtually unchanged upon ^{18}O labeling. This is also markedly different to that calculated for DMNQ in the Q_A binding site.

In the DFT calculated ^{18}O isotope edited spectrum for DQ in the gas phase, the two C=O modes are strongly coupled, and give rise to the band at 1639 cm^{-1} in figure 4C. The calculated gas phase spectrum is in line with the experimental FTIR spectrum for DQ in solution, where only a single (and not two) intense C=O band is observed [69].

From ONIOM calculations for DQ, a single C=C mode is calculated 1620 cm^{-1}. This C=C mode is virtually unaltered in frequency, intensity and mode composition upon ^{18}O labeling (table 6.2).

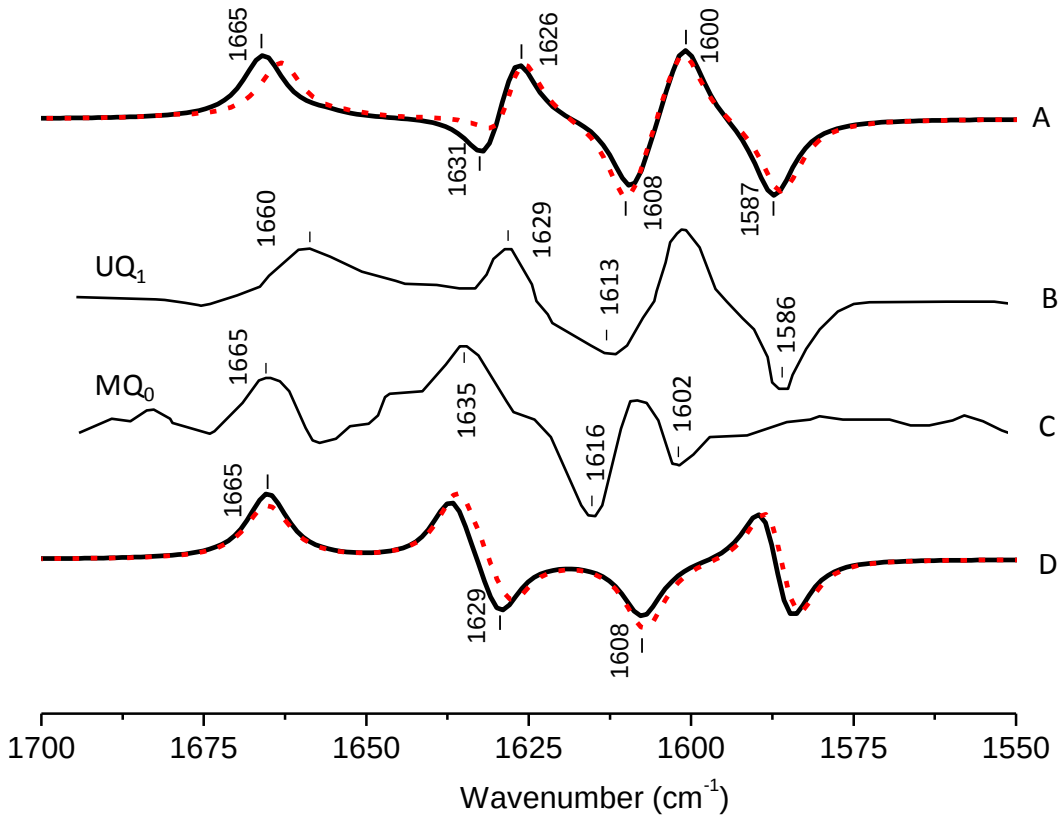

Figure 6.5: (A) ONIOM calculated ^{18}O isotope edited DDS for neutral MQ_0 (*solid*) and UQ_1 (*dotted*) in the Q_A binding site. Experimental spectrum for (B) MQ_0 and (C) UQ_1 are also shown, and were taken from reference [69] with permission. (D) DFT calculated ^{18}O isotope edited DDS for neutral MQ_0 (*solid*) and UQ_1 (*dotted*). ONIOM and gas phase calculated spectra were scaled by 0.9718 and 0.9608, respectively.

Figure 6.5A shows ONIOM calculated ^{18}O isotope edited IR spectra for neutral unlabeled MQ_0 (*solid*) and UQ_1 (dotted) in the Q_A binding site. Figure 5D shows DFT calculated spectra for MQ_0 and UQ_1 in the gas phase. The experimental spectra for MQ_0 and UQ_1 are shown in figure 5B and C, respectively. The normal modes (frequencies and intensities) that give rise to the various bands in the calculated spectra, as well as the PEDs, are listed in table 2. The data for UQ_1 has been presented previously [53] and we show here that very similar data is calculated for both MQ_0 and UQ_1. Replacement of an isoprene unit at C_6 with a methyl group does not appear to significantly alter the calculated spectra.

In the ONIOM calculated ^{18}O isotope edited spectra for neutral MQ_0 the two bands at 1665 and 1626 cm^{-1} are due to C_1=O and C_4=O stretching vibrations, respectively (table 2). Upon ^{18}O labeling the C_1=O and C_4=O modes downshift 34 and 38 cm^{-1}, respectively (table 2). Unlike that found for DMNQ, the mode intensities and composition are little altered by ^{18}O labeling. The C=C mode of MQ_0 and UQ_1 at 1601 cm^{-1} up-shifts 8 cm^{-1} upon ^{18}O labeling (Table 2). An explanation for this ^{18}O induced frequency upshift has been presented [53].

6.5 Discussion

Previously we have shown that ONIOM methods can be used to calculate isotope edited difference spectra for UQ_1 in the Q_A binding site, and that these calculated spectra model very well the corresponding experimental spectra [53]. Here we considerably extend these studies, and show that ONIOM calculated isotope edited spectra for different quinones in the Q_A binding site also model very well the corresponding experimental spectra. We show that the calculated vibrational properties of quinones in the gas phase are totally inappropriate for modeling the vibrational properties of quinones in the Q_A binding site. This is also very likely to be the case for modeling the properties of any protein bound pigment.

Without normal mode vibrational frequency calculations interpretation of experimental spectra is limited. We clearly show here that the computational methods outlined here can lead to a greatly increased understanding of the experimental spectra.

In our ONIOM calculations for neutral UQ_1 in the Q_A binding site we considered all amino acids included in the model only at the molecular mechanics level of computation. Previously, ONIOM calculations have been undertaken in order to model EPR data associated with the UQ_1 anion in the Q_A binding site[40]. In these calculations key amino acids, such as HisM219 and AlaM260, were considered at the higher quantum mechanical level of calculation. It was not shown that this type of calculation was necessary, however. For simulating the vibrational properties of neutral quinones in the Q_A binding site we show that treatment of key amino acids at a quantum mechanical level is not required.

An experimental ^{18}O isotope edited FTIR difference spectrum for UQ in the Q_A binding site is shown in figure 5B. Three positive bands at 1660, 1629 and 1601 cm^{-1} are observed. By considering FTIR difference spectra obtained using PBRCs with unlabeled and specifically $^{13}C_1$ and $^{13}C_4$ labeled UQ occupying the Q_A binding site, it was concluded that the 1660 and 1601 cm^{-1} bands are due to the C_1=O and C_4=O vibrations of unlabeled neutral UQ, respectively. It was also concluded that the 1628 cm^{-1} band is due to a UQ C=C vibration[15]. Since the C_4=O mode was so massively downshifted (1601 cm^{-1} compared to 1664-1650 cm^{-1} for UQ in solvent) it was suggested that this group must be engaged in very strong hydrogen bonding, presumably with HisM219 (figure 2d). This conclusion is difficult to rationalize based on the crystal structural data and other experimental data (see [13] for a review). Such a conclusion is also not supported by the data presented here. Specifically, the C_1=O and C_4=O modes of DMNQ and VK are found at 1653 and 1643 cm^{-1} (table 2), respectively, compared to ~1662 cm^{-1} for the coupled

C=O vibration in solution[40]. Thus the C_1=O/C_4=O mode of DMNQ or VK in the Q_A site is downshifted 9/19 cm^{-1}, respectively, compared to that found in solution. Such shifts suggest that both C=O modes of DMNQ or VK are H-bonded in the Q_A site, albeit quite weakly.

Experimentally, the vibrational modes of DMNQ are at a slightly higher frequency (~3 cm^{-1}) than corresponding modes for VK. Presumably replacing the C_6 methyl group with an isoprene unit causes this difference. Interestingly, this small frequency difference in the modes of DMNQ and VK is also found in our calculated spectra. This result is not specific to the ONIOM method, however, as a small shift is also found in the gas phase calculations (figure 3D).

The C_1=O and C_4=O modes of DMNQ and VK are calculated to be separated by 10 cm^{-1}. The two C=O modes of DQ are calculated to be separated by 13 cm^{-1}. This separation is due to differences in bonding interactions of the two C=O groups. For UQ_1 (and MQ_0) the separation in the C=O modes is 32 cm^{-1} (1660-1628). Some of the differences in frequency of the C=O modes of UQ are due to the different orientation of the methoxy groups. If we assume that differential hydrogen bonding gives rise to a 13 cm^{-1} separation in the frequencies of the C=O modes then this would indicate that the difference in the orientation of the methoxy groups of UQ (or MQ_0) in the Q_A site gives rise to a frequency difference of 19 cm^{-1} for the two C=O groups. This result is in quite good agreement with results from experimental spectra of UQ in solution, which show that the two C=O modes are separated by ~ 16 cm^{-1} [14, 15].

Normal mode vibrational frequencies are governed by molecular bonding force constants. These force constants relate to the electronic structure of the molecule. Since the calculated and experimental spectra for DMNQ and VK are virtually the same it is concluded that the replacing the isoprene unit at C_6 of VK with a methyl group does not appreciably perturb the electronic

structure of the naphthoquinone ring. In addition, the tail does not perturb the protein in a way that significantly modifies any pigment protein interactions

In VK and UQ_1, the "kink" in the tail after the first carbon atom is 3.1-3.2 degrees higher in ONIOM calculations compared to gas phase calculations. It therefore appears that the tail is somewhat constrained relative to the quinone ring when incorporated into the Q_A binding site. It is not clear if this is a significant constraint. The C_1=O and C_4=O bonds of MQ_0 and UQ_1 (and of DMNQ and VK) are virtually unaltered in ONIOM calculations. The hydrogen bond lengths for the C=O groups are also little unaltered. The distance of the C_4=O oxygen to the non heme iron atom is altered by about 0.025-0.055 Å, suggesting a very small change in orientation of the UQ_1 head-group (since the iron atom is fixed) compared to MQ_0 (or VK compared DMNQ) in the Q_A binding site. The isoprene unit therefore leads to a very slight change in the orientation of the quinone ring in the Q_A binding site.

The experimental ^{18}O isotope edited spectrum for MQ_0 is quite different to that for UQ (compare figure 5B and C). This difference cannot be modeled computationally (figure 5A). The experimental isotope edited spectrum for MQ_0 is considerably noisier than the spectrum for UQ [69]. As far as we are aware the Q_A^-/Q_A FTIR difference spectrum for RCs with MQ_0 in the binding site have never been reproduced, so the accuracy of the spectrum may be somewhat questionable. On the other hand MQ_0 may be able to incorporate into the Q_A binding site with the methoxy groups oriented in several different ways. As described previously, each of these methoxy group conformers will have slightly different spectra[50]. This heterogeneity in orientation of MQ_0 in the Q_A binding site may contribute to differences in the experimental spectra for MQ_0 and UQ in figure 5B and C. In spite of this, there are similarities in the MQ_0 and UQ experimental spectra in figure 5B and C. For the MQ_0 spectrum positive bands are

found at 1665, 1631 and 1608 cm^{-1}. For UQ_1 the bands are at 1660, 1628 and 1601 cm^{-1}. For the MQ_0 spectrum negative bands are found at 1616 and 1602 cm^{-1}. For UQ the bands are at 1613 and 1586 cm^{-1}.

6.6 Conclusions

We have shown that ONIOM type QM/MM calculations can be used to model experimental isotope edited FTIR difference spectra obtained using purple bacterial reaction centers that have had several different quinones incorporated into the Q_A binding site. The fact that the many different spectra can all be modeled is a clear indicator of the appropriateness of the approach.

The calculated spectra appear not to depend on whether the quinone incorporated has a prenyl/phytyl unit or a methyl group attached at C_6. The electronic structure of the quinone ring is therefore not sensitive to the presence or absence of a hydrocarbon side chain at C_6. This suggests that the hydrocarbon side chain does not significantly constrain the quinone ring in the Q_A binding site.

7 REFERENCES

1. Gest, H., *History of the word photosynthesis and evolution of its definition.* Photosynthesis Research, 2002. **73**(1): p. 7-10.
2. Blankenship, R.E. and H. Hartman, *The origin and evolution of oxygenic photosynthesis.* Trends in Biochemical Sciences, 1998. **23**(3): p. 94-97.
3. Hunter, C.N., Daldal, F. and Thurner, M. C., *Purple Phototrophic Bacteria Advances in Photsynthesis and Respiration.* 2009. **28**.
4. Ke, B., *Photosynthesis : photobiochemistry and photobiophysics*. Advances in photosynthesis ;. 2001, Kluwer Academic Publishers: Dordrecht ;.
5. Hillier, W. and G.T. Babcock, *Photosynthetic Reaction Centers.* Plant Physiology, 2001. **125**(1): p. 33-37.
6. Stowell, M.H.B. and T.M. McPhillips, *Light-induced structural changes in photosynthetic reaction center: Implications for mechanism of el.* Science, 1997. **276**(5313): p. 812.
7. Blankenship, R.E., Madigan, M. T., andd Bauer, C. E., Eds., *Anoxygenic Photosynthetic Bacteria.* 1995.
8. Feher, G. and M. Okamura, *The primary and secondary acceptors in bacterial photosynthesis: II. The structure of the Fe2+ -Q− complex.* Applied Magnetic Resonance, 1999. **16**(1): p. 63-100.
9. Kirmaier, C., et al., *Comparison of M-Side Electron Transfer in Rb. sphaeroides and Rb. capsulatus Reaction Centers.* The Journal of Physical Chemistry B, 2002. **106**(7): p. 1799-1808.
10. Okamura, M.Y., et al., *Proton and electron transfer in bacterial reaction centers.* Biochimica et Biophysica Acta (BBA) - Bioenergetics, 2000. **1458**(1): p. 148-163.
11. Gunner, M.R. and E. Alexov, *A pragmatic approach to structure based calculation of coupled proton and electron transfer in proteins.* Biochimica et Biophysica Acta (BBA) - Bioenergetics, 2000. **1458**(1): p. 63-87.
12. Bosch, M.K., et al., *The primary acceptor quinone QA in reaction centers of Rhodobacter sphaeroides R26 is hydrogen bonded to the N[sigma](1)-H of His M219. An electron spin echo study of QA.* Chemical Physics Letters, 1995. **239**(4-6): p. 306-312.
13. Wraight, C.A. and M.R. Gunner, *The acceptor quinones of purple photosynthetic bacteria-structure and spectroscopy. The Purple Photosynthetic Bacteria, eds C. N. Hunter, F Daldal, M. C. Thurnnauer, and J. T. Beatty (Springer, Doredretcht).* 2009. **28**: p. 379-405.
14. Brudler, R., et al., *Asymmetric binding of the 1- and 4-C=O groups of QA in Rhodobacter sphaeroides R26 reaction centres monitored by Fourier transform infra-red spectroscopy using site-specific isotopically labelled ubiquinone-10.* The EMBO Journal, 1994. **13**(23): p. 5523-5530.
15. Breton, J., et al., *Binding Sites of Quinones in Photosynthetic Bacterial Reaction Centers Investigated by Light-Induced FTIR Difference Spectroscopy: Assignment of the Interactions of Each Carbonyl of QA in Rhodobacter sphaeroides Using Site-Specific 13C-Labeled Ubiquinone.* Biochemistry, 1994. **33**(48): p. 14378-14386.
16. Breton, J., et al., *The Binding Sites of Quinones in Photosynthetic Bacterial Reaction Centers Investigated by Light-Induced FTIR Difference Spectroscopy: Assignment of the*

QA Vibrations in Rhodobacter sphaeroides Using 18O- or 13C-Labeled Ubiquinones and Vitamin K1. Biochemistry, 1994. **33**(16): p. 4953-4965.
17. Breton, J., et al., *Binding sites of quinones in photosynthetic bacterial reaction centers investigated by light-induced FTIR difference spectroscopy: Binding of chainless symmetrical quinones to the QA site of Rhodobacter sphaeroides.* Biochemistry, 1994. **33**(41): p. 12405-12415.
18. Foresman, J. and A. Frisch, *Exploring Chemistry with Electronic Structure Methods.* 1996.
19. Vreven, T., et al., *Combining Quantum Mechanics Methods with Molecular Mechanics Methods in ONIOM.* Journal of Chemical Theory and Computation, 2006. **2**(3): p. 815-826.
20. Trumpower, B., *Function of Quinones in Energy Conserving Systems.* Academic Press, 1982.
21. Ke, B., *The Bacterial Photosynthetic Reaction Center: Chemical Composition and Crystal Structure*, in *Photosynthesis: Photobiochemistry and Photobiophysics*. 2001, Kluwer Academic Publishers: Dordrecht; Boston. p. 47-62.
22. Ke, B., *The "Stable" Primary Electron Acceptor (Q_A) of Photosynthetic Bacteria*, in *Photosynthesis: Photobiochemistry and Photobiophysics*. 2001, Kluwer Academic Publishers, : Dordrecht ; Boston. p. 101-110.
23. Ke, B., *The Secondary Electron Acceptor (Q_B) of Photosynthetic Bacteria*, in *Photobiochemistry and Photobiophysics* 2001, Kluwer Academic Publishers: Dordrecht ; Boston. p. 111-128.
24. Breton, J. and E. Nabedryk, *Protein-quinone interactions in the bacterial photosynthetic reaction center: light-induced FTIR difference spectroscopy of the quinone vibrations.* Biochimica et Biophysica Acta (BBA) - Bioenergetics, 1996. **1275**(1-2): p. 84-90.
25. Burie, J.-R., et al., *FTIR Spectroscopy of UV-Generated Quinone Radicals: Evidence for an Intramolecular Hydrogen Atom Transfer in Ubiquinone, Naphthoquinone, and Plastoquinone.* The Journal of Physical Chemistry, 1995. **99**(12): p. 4059-4070.
26. Nonella, M. and C. Brandli, *Density Functional Investigation of Methoxy-Substituted p-Benzoquinones: Conformational Analysis and Harmonic Force Fields of 2-Methoxy- and 2,3-Dimethoxy-1,4-benzoquinone.* Journal of Physical Chemistry, 1996. **100**(34): p. 14549-14559.
27. Wheeler, R.A., *Quinones and quinoidal radicals in photosynthesis*, in *Theoretical Biochemistry-Processes and Properties of Biological Systems*, L.A. Eriksson, Editor. 2001, Elsevier. p. 655-690.
28. Burie, J.-R., et al., *Importance of the Conformation of Methoxy Groups on the Vibrational and Electrochemical Properties of Ubiquinones.* Journal of Physical Chemistry B, 1997. **101**(33): p. 6607-6617.
29. Robinson, H.H. and S.D. Kahn, *Interplay of substituent conformation and electron affinity in quinone models of quinone reductases.* Journal of the American Chemical Society, 1990. **112**(12): p. 4728-4731.
30. Boesch, S.E. and R.A. Wheeler, *Structures and properties of ubiquinone-1 and its radical anion from hybrid Hartree-Fock/density functional studies.* J. Phys. Chem. A, 1997. **101**(32): p. 5799-5804.

31. Balakrishnan, G., P. Mohandas, and S. Umpathy, *Ab initio studies on structure and vibrational spectra of ubiquinone and its radical anion.* Spectrochimica Acta Part A: Molecular and Biomolecular Spectroscopy, 1997. **53**(10): p. 1553-1561.
32. Breton, J. and E. Nabedryk, *Protein-quinone interactions in the bacterial photosynthetic reaction center: Light-induced FTIR difference spectroscopy of the quinone vibrations.* Biochim. Biophys. Acta, 1996. **1275**(1-2): p. 84-90.
33. Frisch, M.J., et al., *Gaussian 03, Revision C.02.* Gaussian 03, Revision D.01, 2004.
34. Cances, E., B. Mennucci, and J. Tomasi, *An new integral equation formalism for the polarizable continuum model: Theoretical background.* Journal of Chemical Physics, 1997. **107**(8): p. 3032.
35. Cancès, E., et al., *Integral Equation Methods for Molecular Scale Calculations in the Liquid Phase.* Mathematical Models & Methods in Applied Sciences, 1999. **9**(1): p. 35.
36. Tomasi, J., B. Mennucci, and E. Cancès, *The IEF version of the PCM solvation method: an overview of a new method addressed to study molecular solutes at the QM ab initio level.* Journal of Molecular Structure: THEOCHEM, 1999. **464**(1-3): p. 211-226.
37. Tomasi, J., et al., *Molecular properties in solution described with a continuum solvation model.* Physical Chemistry Chemical Physics, 2002. **4**(23): p. 5697-5712.
38. Tomasi, J., B. Mennucci, and R. Cammi, *Quantum Mechanical Continuum Solvation Models.* Chemical Reviews, 2005. **105**(8): p. 2999-3094.
39. Bandaranayake, K., et al., *Modeling The A_1 Binding Site In Photosystem I. Density Functional Theory For The Calculation Of "Anion – Neutral" FTIR Difference Spectra of Phylloquinone.* Vib. Spectrosc., 2006. **42**(1): p. 78-87.
40. Priyangika Bandaranayake, K.M., et al., *Modeling the A1 binding site in photosystem: I. Density functional theory for the calculation of "anion − neutral" FTIR difference spectra of phylloquinone.* Vibrational Spectroscopy, 2006. **42**(1): p. 78-87.
41. Rauhut, G. and P. Pulay, *Transferable Scaling Factors for Density-Functional Derived Vibrational Force-Fields.* Journal of Physical Chemistry, 1995. **99**(10): p. 3093-3100.
42. Boullais, C., et al., *Site-specific isotope labeling demonstrates a large mesomeric resonance effect of the methoxy groups on the carbonyl frequency in ubiquinones.* Photosynthesis Research, 1998. **55**(2): p. 247-252.
43. Srinivasan, N. and J.H. Golbeck, *Protein-cofactor interactions in bioenergetic complexes: The role of the A1A and A1B phylloquinones in Photosystem I.* Biochimica et Biophysica Acta (BBA) - Bioenergetics, 2009. **1787**(9): p. 1057-1088.
44. Bauscher, M. and W. Maentele, *Electrochemical and infrared-spectroscopic characterization of redox reactions of p-quinones.* The Journal of Physical Chemistry, 1992. **96**(26): p. 11101-11108.
45. Bauscher, M., et al., *Investigation of models for photosynthetic electron acceptors: Infrared spectroelectrochemistry of ubiquinone and its anions.* FEBS Letters, 1990. **261**(1): p. 191-195.
46. Zhao, X., et al., *Observation of the Resonance Raman Spectra of the Semiquinones QA•- and QB•- in Photosynthetic Reaction Centers from Rhodobacter sphaeroides R26.* Journal of the American Chemical Society, 1997. **119**(22): p. 5263-5264.
47. Nonella, M., *A Density Functional Investigation of Model Molecules for Ubisemiquinone Radical Anions.* The Journal of Physical Chemistry B, 1998. **102**(21): p. 4217-4225.
48. Frisch, M.J., et al., *Gaussian 03, Revision C.02.* 2004.
49. Martin, J.M.L. and A.C. Van, *GAR2PED.* 1995.

50. Lamichhane, H., R. Wang, and G. Hastings, *Comparison of calculated and experimental FTIR spectra of specifically labeled ubiquinones.* Vibrational Spectroscopy, 2011. **55**(2): p. 279-286.
51. Nonella, M., et al., *Structures and Vibrational Frequencies of the Quinones in Rb. sphaeroides Derived by a Combined Density Functional/Molecular Mechanics Approach.* The Journal of Physical Chemistry B, 2002. **107**(1): p. 316-322.
52. Nonella, M. and C. Brandli, *Density Functional Investigation of Methoxy-Substituted p-Benzoquinones: Conformational Analysis and Harmonic Force Fields of 2-Methoxy- and 2,3-Dimethoxy-1,4-benzoquinone.* J. Phys. Chem., 1996. **100**(34): p. 14549-14559.
53. Lamichhane, H.P. and G. Hastings, *Calculated vibrational properties of pigments in protein binding sites.* Proceedings of the National Academy of Sciences, 2011. **108**(26): p. 10526-10531.
54. Case, D.A., et al., *The Amber biomolecular simulation programs.* Journal of Computational Chemistry, 2005. **26**(16): p. 1668-1688.
55. Cornell, W.D., et al., *A Second Generation Force Field for the Simulation of Proteins, Nucleic Acids, and Organic Molecules.* Journal of the American Chemical Society, 1995. **117**(19): p. 5179-5197.
56. Isaacson, R.A., Abresch, E. C., Lendzian, F., Boullais, C., Paddock, M. L., Mioskowski, C., Lubitz, W., and Feher, G., *Asymmetry of the Binding Sites of QA-· and QB-· in Reaction Centers of Rb. sphaeroides Probed by Q-Band EPR with 13C-Labeled Quinones.* Structure and Dynamics, 1996: p. 353-368.
57. Lubitz, W. and G. Feher, *The primary and secondary acceptors in bacterial photosynthesis III. Characterization of the quinone radicals QA− and QB− by EPR and ENDOR.* Applied Magnetic Resonance, 1999. **17**(1): p. 1-48.
58. Trumpower, B., *Function of Quinones in Energy Conserving Systems*. 1982: Academic Press.
59. Ke, B., *The Stable Primary Acceptor Q_A and the Secondary Electron Acceptor Q_B,* in *Photosynthesis: Photobiochemistry and Photobiophysics*. 2001, Kluwer Academic Publishers: Dordrecht; Boston. p. 289-304.
60. Shopes, R.J. and C.A. Wraight, *The acceptor quinone complex of Rhodopseudomonas viridis reaction centers.* Biochim Biophys Acta, 1985. **806**(3): p. 348-56.
61. Hale, M.B., R.E. Blankenship, and R.C. Fuller, *Menaquinone is the sole quinone in the facultatively aerobic green photosynthetic bacterium Chloroflexus aurantiacus.* Biochimica et Biophysica Acta (BBA) - Bioenergetics, 1983. **723**(3): p. 376-382.
62. Warncke, K., et al., *Influence of Hydrocarbon Tail Structure on Quinone Binding and Electron-Transfer Performance at the Q(a) and Q(B) Sites of the Photosynthetic Reaction-Center Protein.* Biochemistry, 1994. **33**(25): p. 7830-7841.
63. Noguchi, T. and C. Berthomieu, *Molecular Analysis by Vibrational Spectroscopy*, in *Photosystem II The Light Driven Water:Plastoquinone Oxidoreductase*, T. Wydrzynski and K. Satoh, Editors. 2005, Springer: Dordrecht. p. 367-387.
64. Vreven, T., et al., *Combining quantum mechanics methods with molecular mechanics methods in ONIOM.* Journal of Chemical Theory and Computation, 2006. **2**(3): p. 815-826.
65. Stowell, M.H., et al., *Light-induced structural changes in photosynthetic reaction center: implications for mechanism of electron-proton transfer.* Science, 1997. **276**(5313): p. 812-816.

66. Wheeler, R.A., *Theoretical Biochemistry-Processes and Properties of Biological Systems.* 2001. **Chapter 15,** : p. 655-690.
67. Case, D.A., et al., *The Amber biomolecular simulation programs.* Journal of Computational Chemistry, 2005. **26**(16): p. 1668-1688.
68. Foresman, J. and A. Frisch, *Exploring Chemistry with Electronic Structure Methods (2nd Edition).* 1996, Pittsburg, PA: Gaussian Inc.
69. Breton, J., et al., *Binding sites of quinones in photosynthetic bacterial reaction centers investigated by light-induced FTIR difference spectroscopy: binding of chainless symmetrical quinones to the Q_A site of Rhodobacter sphaeroides.* Biochemistry, 1994. **33**(41): p. 12405-12415.

8 APPENDIX

8.1 Appendix A.

Exploration of minimum energy conformations of ubiquinone molecule at various constraint methoxy group dihedral angles

Ubiquinone has two methoxy groups at 2- and 3-carbon positions. Orientations of these methoxy groups have great impact on the properties of the ubiquinone molecule. The methoxy methyl group can be rotated 360° about the C_r-O bond, where C_r represents one of the carbon atoms of ubiquinone ring. Gaussian key word "opt=modredundant" facilitates the calculation of the geometry optimized energy of ubiquinone at some constraint dihedral angle. In order to explore minimum energy conformation of ubiquinone, the ubiquinone molecule can be optimized at various constraint methoxy group dihedral angles from 0° to 360°. With 10° increment of one methoxy group dihedral angle keeping another dihedral and constraint at some angle, there will be at least 37 geometry optimization calculations. For a systematic calculation, the gen section of Gaussian input file can be edited leaving a blank line after geometry parameters as follows:

D * 2 17 * R

D * 3 16 * R

D 2 3 16 8 0.000000 S 37 10.000000

D 1 2 17 9 -64.400000 S 0 0.000000

Notation and explanation:

D: dihedral angle

R: remove other bonds

S: step number

*: any adjacent atom

The Gaussian program first isolates dihedral angles associates with bonds C_2-O_{17} and C_3-O_{18}. Dihedral angle C_1-C_2-O_{17}-C_9 will be fixed at -64.4°. The dihedral angle C_2-C_3-O_{16}-C_8 will be set at 0° for the first geometry optimization of the molecule. Then, the dihedral angle C_2-C_3-O_{16}-C_8 will be set at 10^0 and the molecule is optimized for geometry. The ubiquinone molecule will be optimized 37 times in 10° increment of C_2-C_3-O_{16}-C_8 dihedral angle.

8.2 Appendix B

Calculation of resp charge and amber parameters of ubiquinone

Electronic embedding of protein binding site on the pigment ubiquinone molecule in the QA binding site of Rb. sphaeroides RC can be applied in the during molecular optimization of ubiquinone using ONIOM (QM/MM) calculation with amber at the MM level. Resp charge and amber parameters for ubiquinone molecule can be calculated using antechamber program. Key steps for calculating resp charge and amber parameters using antechamber program are summarized below.

1) Geometry Optimization

a. Download 1AIJ pdb file from protein data bank.

b. Open the 1AIJ file in Swisspdb Viewer, select U10311 pigment , save the pigment structure in the pdb format.

c. Open U10311.pdb in GaussView, add hydrogens and check the structure to make sure the final structure is close to the known structure.

d. Substitute H for the part of the isoprene unit after the first unit and name the molecule UQ1.

e. Geometry optimize the structure at B3LYP/6-31G(d) level (Output file UQ1.log). Put the log file in the data folder in the antechamber package.

2) Resp Charge calculation

a. Run a Gaussian single point energy calculation at the HF/6-31G(d) level with additional key words iop(6/33=2) pop=mk scf=tight. The output file is UQ1HF.log

[iop(6/33=2) makes Gaussian write out the potential points and potentials.]

b. Extract the ESP information from the UQ1.log file using antechamber in to a file named UQ1.esp

./amber10/exe/espgen –i UQ1.log –o UQ1.esp

c. Perform the two- stage resp fit in antechamber. The UQ1_resp.ac has the resp charges for UQ1.

./amber10/exe/antechamber – i UQ1.log - fi gout – o UQ1.ac - fo ac

./amber10/exe/respgen -i UQ1.ac -o UQ1.respin1 -f resp1

./amber10/exe/respgen -i UQ1.ac -o UQ1.respin2 -f resp2

./amber10/exe/resp -O -i UQ1.respin1 -o UQ1.respout1 -e UQ1.esp –t qout_stage1

./amber10/exe/resp -O -i UQ1.respin2 -o UQ1.respout2 -e UQ1.esp -q qout_stage1-t qout_stage2

./amber10/exe/antechamber -i UQ1.ac -fi ac -o UQ1_resp.ac -fo ac -c rc -cf qout_stage2

The UQ1_resp.ac has the resp charges for UQ1.

3) AMBER atom type and Force Field Parameters

a. Re-Run Geormetry optimization of file UQ1.log at molecular mechanics (UFF) level. The output file is UQ1UFF.log

b. Run antechamber to get the AMBER atom types and missing force filed parameters.

./amber10/exe/antechamber –i UQ1UFF.log –fi gout –o UQ1_AMBER.ac –fo ac –at amber

./amber10/exe/parmchk –i UQ1_AMBER.ac –f ac –o UQ1.frcmod

Note: All files are kept in folder “data”. Similar process can also be applied to anion UQ_1.

8.3 Appendix C

Gar2ped for generating internal coordinates and calculating potential energy distribution of UQ_1:

Internal coordinates of a molecule such as bond length, angle, dihedral angle and wag (out-of-plane) are independent of the translational and rotational motions of the molecule and hence, they are preferred to define vibrational modes of the molecule. Internal coordinates of a molecule can be generated using gar2ped program. Gar2ped has two functions.

1) Pullarc is used to read archieve data from the vibrational frequency output file.
2) Gar2ped can be used to generate internal coordinates of UQ1 using various codes provided in the gar2ped program. Gar2ped also calculates potential energy distribution and phase relationships of a vibrational mode.

Figure 8.1 shows structure UQ_1 and notations of the internal coordinates. Table 8.1 presents description of each internal coordinate.

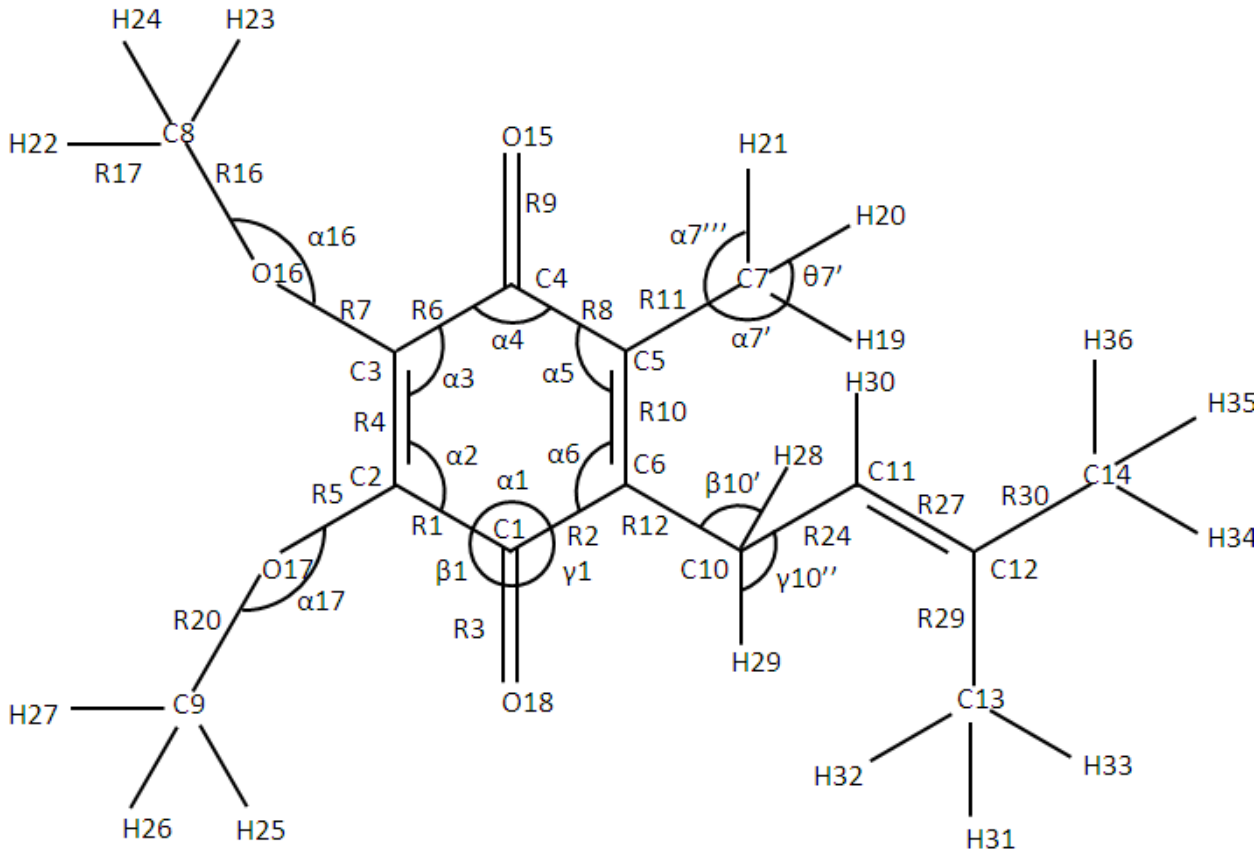

Figure 8.1. Structure of UQ_1 and representation of internal coordinates

Table 8.1: Definition of internal coordinates of UQ_1

Internal Coordinate Number	Internal Coordinate	Description
1, 2, 6, 8, 11, 12, 24, 29, 30	R1, R2, R6, R8, R11, R12, R24, R29, R30	C-C stretching
4, 10, 27	R4, R10, R27	C=C stretching
3, 9	R3, R9	C=O stretching
5, 7, 16, 20	R5, R7, R16, R20	C-O stretching
13, 14, 15, 17, 18, 19, 21, 22, 23, 25, 26, 28, 31, 32, 33, 34, 35, 36	R13, R14, R15, R17, R18, R19, R21, R22, R23, R25, R26, R28, R31, R32, R33, R34, R35, R36	C-H stretching
37	$6^{-0.5}$(α1-α2+α3-α4+α5-α6)	Ring def. (in plane): RD1
38	$12^{-0.5}$(2α1-α2-α3+2α4-α5-α6)	Ring def. (in plane): RD2
39	2^{-1}(α2-α3+α5-α6)	Ring def. (in plane): RD3
44, 46	σ1, σ4	C=O wag (out-of-plane)
48, 50	σ3, σ2	C-O wag (out-of-plane)
52, 54, 90	σ6, σ5, σ12	C-C wag (out-of-plane)
40	$6^{-0.5}$(τ1-τ2+τ3-τ4+τ5-τ6)	Ring torsion

41	$2^{-1}(\tau1-\tau3+\tau4-\tau6)$	Ring torsion
42	$12^{-0.5}(-\tau1+2\tau2-\tau3-\tau4+2\tau5-\tau6)$	Ring torsion
43, 45	$2^{-0.5}(\beta1-\gamma1)$, $2^{-0.5}(\beta4-\gamma4)$	C=O def. (in plane)
47, 49	$2^{-0.5}(\beta3-\gamma3)$, $2^{-0.5}(\beta2-\gamma2)$	C-O def. (in plane)
51, 53	$2^{-0.5}(\beta6-\gamma6)$, $2^{-0.5}(\beta5-\gamma5)$	C-C def. (in plane)
55	$6^{-0.5}(\theta7'+\theta7''+\theta7'''-\alpha7'-\alpha7''-\alpha7''')$	C7-methyl bending
56	$6^{-0.5}(2\theta7'-\theta7''-\theta7''')$	C7-methyl bending
57	$2^{-0.5}(\theta7'-\theta7'')$	C7-ethyl bending
58	$6^{-0.5}(2\alpha7'-\alpha7''-\alpha7''')$	C7-methyl bending
59	$2^{-0.5}(\alpha7'-\alpha7'')$	C7-methyl bending
60, 65	$6^{-0.5}(\theta8'+\theta8''+\theta8'''-\alpha8'-\alpha8''-\alpha8''')$, $6^{-0.5}(\theta9'+\theta9''+\theta9'''-\alpha9'-\alpha9''-\alpha9''')$	Methoxy-methyl bending
61, 66	$6^{-0.5}(2\theta8'-\theta8''-\theta8''')$, $6^{-0.5}(2\theta9'-\theta9''-\theta9''')$	Methoxy-methyl bending
62, 67	$2^{-0.5}(\theta8'-\theta8'')$, $2^{-0.5}(\theta9'-\theta9'')$	Methoxy-methyl bending
63, 68	$6^{-0.5}(2\alpha8'-\alpha8''-\alpha8''')$, $6^{-0.5}(2\alpha9'-\alpha9''-\alpha9''')$	Methoxy-methyl bending
64, 69	$2^{-0.5}(\alpha8'-\alpha8'')$, $2^{-0.5}(\alpha9'-\alpha9'')$	Methoxy-methyl bending
70, 75	$6^{-0.5}(\theta13'+\theta13''+\theta13'''-\alpha13'-\alpha13''-\alpha13''')$, $6^{-0.5}(\theta14'+\theta14''+\theta14'''-\alpha14'-\alpha14''-\alpha14''')$	Tail-methyl bending
71, 76	$6^{-0.5}(2\theta13'-\theta13''-\theta13''')$, $6^{-0.5}(2\theta14'-\theta14''-\theta14''')$	Tail -methyl bending
72, 77	$2^{-0.5}(\theta13'-\theta13'')$, $2^{-0.5}(\theta14'-\theta14'')$	Tail -methyl bending
73, 78	$6^{-0.5}(2\alpha13'-\alpha13''-\alpha13''')$, $6^{-0.5}(2\alpha14'-\alpha14''-\alpha14''')$	Tail -methyl bending
74, 79	$2^{-0.5}(\alpha13'-\alpha13'')$, $2^{-0.5}(\alpha14'-\alpha14'')$	Tail -methyl bending
80, 81	$26^{-0.5}(5\theta10+\alpha10)$, $26^{-0.5}(\theta10+5\alpha10)$	H-C-H, C-C-C bend
82, 83, 84	$2^{-1}(\beta10'-\beta10''+\gamma10'-\gamma10'')$, $2^{-1}(\beta10'+\beta10''-\gamma10'-\gamma10'')$, $2^{-1}(\beta10'-\beta10''-\gamma10'+\gamma10'')$	C10-H def.
85, 86	$6^{-0.5}(2\alpha11-\beta11-\gamma11)$, $2^{-0.5}(\beta11-\gamma11)$	C11-H def. (in plane)
87	$\sigma11$	C-H wag (out-of-plane)
88, 89	$6^{-0.5}(2\alpha12-\beta12-\gamma12)$, $2^{-0.5}(\beta12-\gamma12)$	C-C12-C bend
90	$\sigma12$	C-C wag (out-of-plane)
91, 93	$\tau3\text{-}16$, $\tau2\text{-}17$	C-C-O-C torsion
92, 94	$\tau8\text{-}16$, $\tau9\text{-}17$	H-C-O-C torsion
95, 99, 100	$\tau5\text{-}7$, $\tau12\text{-}13$, $\tau12\text{-}14$	C-C-C-H torsion
96, 97, 98	$\tau6\text{-}10$, $\tau10\text{-}11$, $\tau11\text{-}12$	X-C-C-X(H or C) torsion
101, 102	$\alpha16$, $\alpha17$	C-O-C bend

Notations:

x = atom number

Cx, Ox and Hx are carbon, oxygen and hydrogen atoms

Ri = i^{th} bond

αx = angle between consecutive sides at the vertex x

βx = angle between the first and the third side which are connected at the vertex x

γ x= angle between the second and the third side which are connected at the vertex x

θx = H-C-H angle at the vertex atom Cx

‘, ‘’ and ‘’’ = numbering of similar angles (used for CH3 and CH2 groups) at a vertex

σx = angle of wag at the vertex x

τx-x = torsion angle about the bond x-x.

We are interested only in the frequency region between 1800 and 1300 cm^{-1} because the most intense IR bands of C=C, C=O and C-C stretching vibrations occur in this region. In this sense, CH bending vibrations can be regrouped in order to reduce cost of data analysis. Brief notation for CH bending is:

δCx for CH bending associated with Cx^{th} carbon atom.

Example: Internal coordinate numbers 55, 56, 57, 58 and 59 belong to δC_7.

This new notation is used in this article.

8.4 Appendix D.

Calculated IR absorption spectra and potential energy distribution of unlabeled, $^{13}C_1$, $^{13}C_4$, ^{13}C and ^{18}O labeled ubisemiquinone in the Q_A binding site of Rb. sphaeroides reaction centers.

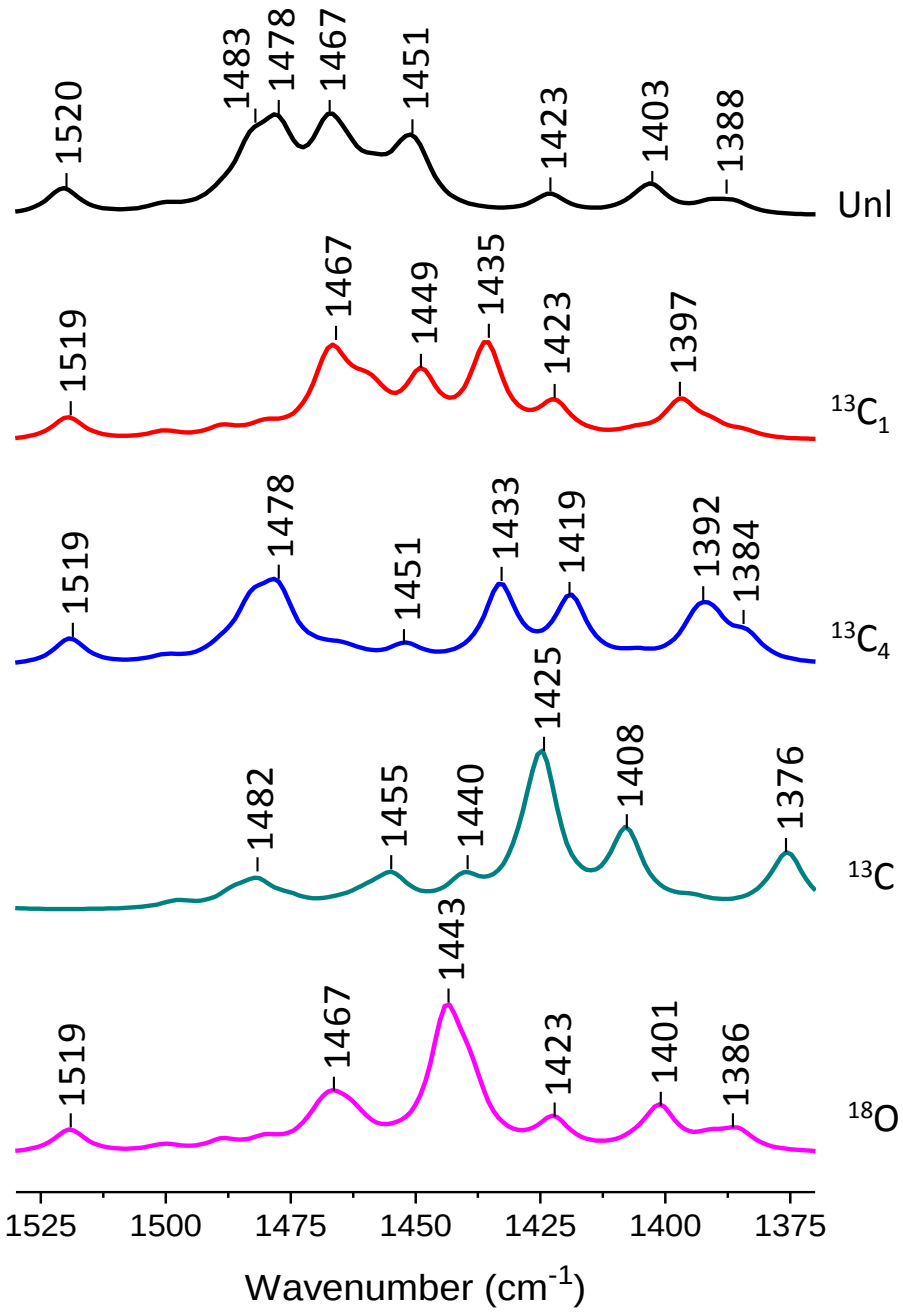

Figure 8.2 Calculated absorption spectra of unlabeled, $^{13}C_1$, $^{13}C_4$, ^{13}C and ^{18}O labeled UQ_1^- in the Q_A binding site of Rb. sphaeroides reaction centers.

Table 8.2 Calculated IR frequency, frequency shift, IR intensity and potential energy distribution of unlabeled, $^{13}C_1$, $^{13}C_4$, ^{13}C and ^{18}O labeled UQ_1^- in the Q_A binding site of Rb. sphaeroides RC

Frequency (cm^{-1})	Δν (cm^{-1})	IR Intensity (km/mol)	Potential Energy Distribution
Unlabeled Anion UQ_1			
1450		66	R9(11%)-R6(6%)+δC9(42%)+δC8(11%)
1452		52	R3(14%)-R10(5%)+δC7(37%)+δC10(18%)
1458		33	R9(11%)+δC8(38%)+δC9(30%)
1464		31	R9(7%)+δC7(47%)+δC9(9%)+δC10(7%)
1466		25	R9(15%)+δC9(38%)+δC7(14%)+δC8(8%)
1468		84	R9(24%)+δC8(34%)+δC9(15%)
1477		93	R3(24%)+δC13(19%)+δC7(19%)+δC14(7%)+δC10(6%)
1483		75	R3(33%)+δC13(31%)+δC10(10%)
1521		41	R4(33%)-R10(19%)-R5(9%)-R7(6%)
1599		29	R10(27%)+R4(24%)+RD2(11%)
$^{13}C_1$ labeled Anion UQ_1			
1436	47, 41, 16	141	R3(58%)+δC7(6%)+RD1(6%)
1449	1	86	R9(12%)+ R6(6%)+δC9(45%)+δC8(9%)
1458	0	34	R9(11%)+δC8(41%)+δC9(27%)
1461	16, -9	30	R3(9%)+δC7(31%)+δC10(16%)+δC13(13%)+δC14(10%)
1464	0	14	R9(11%)+δC7(37%)+δC9(28%)
1467	-1	61	R9(13%)+δC7(39%)+δC9(17%)+δC8(6%)
1468	0	52	R9(22%)+δC8(36%)+δC9(18%)
1520	1	36	R4(33%)-R10(20%)-R5(9%)-R7(6%)+δC7(5%)
1597	2	36	R10(28%)+R4(26%)+RD2(11%)
$^{13}C_4$ labeled Anion UQ_1			
1394	10	56	R9(8%)-R8(15%)+R2(11%)+δC14(13%)+δC8(8%)+RD3(8%)
1419	39, 31	99	R9(17%)-R6(10%)+δC8(28%)+δC9(10%)+δC7(9%)
1433	35, 33, 31	118	R9(36%)+δC8(27%)+δC9(13%)
1453	-1	14	R3(11%)-R10(8%)+δC7(31%)+δC10(18%)
1477	0	87	R3(24%)+δC7(19%)+δC13(19%)+δC14(7%)+δC10(6%)
1483	0	69	R3(33%)+δC13(31%)+δC10(10%)
1519	2	41	R4(32%)-R10(20%)-R5(9%)-R7(5%)+δC7(5%)
1596	3	30	R10(28%)+R4(26%)+RD2(11%)
^{13}C labeled Anion UQ_1			
1375	12	82	R9(11%)+R11(7%)+δC7(70%)
1408	15	114	R9(16%)+ R4(5%)+δC8(39%)+δC7(8%)+δC9(6%)
1425	43, 41	218	R9(27%)-R3(10%)-R4(7%)+δC9(13%)+δC8(6%)+δC7(6%)-RD1(5%)
1428	49	35	R3(39%)-R10(13%)+R9(11%)+δC9(7%)+δC8(6%)+δC7(6%)
1440	18	37	R9(6%)-R3(5%)+δC9(33%)+δC8(24%)
1455	28	41	R3(19%)-R10(5%)+δC7(19%)+δC9(17%)+δC8(12%)

1482	39	36	R4(19%)+R5(5%)+ δC7(23%)+δC13(9%)
1541	58	25	R10(26%)+R4(22%)+RD2(11%)
^{18}O labeled Anion UQ_1			
1401	2	67	R9(6%)-R8(19%)+R2(12%)+RD3(9%)+δC8(15%)
1439	29, 27	78	R9(37%)-R3(11%)-R6(7%)+δC9(14%)
1444	39, 33	194	R3(33%)- R9(8%)+RD1(7%)+δC7(17%)+δC10(6%)
1454	12	4	R9(7%)+δC9(38%)+δC8(11%)+δC9(10%)
1463	14	25	R3(7%)+δC7(37%)+δC10(15%)+δC13(11%)+δC14(10%)
1468	9	35	R3(12%)+δC7(42%)+δC9(16%)
1519	2	36	R4(33%)-R10(21%)-R5(9%)-R7(5%)+δC7(5%)
1598	1	30	R10(27%)+R4(25%)+RD2(11%)

Ri = i^{th} bond stretching;
δCi = X-C_i-X bending for -CH_3, -CH_2- and –CH= groups; X = atom bonded to the atom C_i;
RD1 = $6^{-1/2}$(α1- α2+ α3- α4+ α5- α6); RD2 = $12^{-1/2}$(2α1- α2- α3+2α4- α5- α6); RD3 = (½)(α2- α3+ α5- α6) = ring deformation;
αi = C_{i-1}-C_i-C_{i+1} angle bending of ring atoms
Atom and bond numbers are shown in Figure 5.1 B.